Bespoke Binder Jetting System and Powder Bed Temperature Assessment

by

Matthew Chai

A thesis
presented to the University of Waterloo
in fulfillment of the
thesis requirement for the degree of
Master of Applied Science
in
Mechanical and Mechatronics Engineering

Waterloo, Ontario, Canada, 2024

© Matthew Chai 2024

Author's Declaration

I hereby declare that I am the sole author of this thesis. This is a true copy of the thesis, including any required final revisions, as accepted by my examiners.

I understand that my thesis may be made electronically available to the public.

Abstract

Binder jetting is an additive manufacturing process in which powdered material is bound together via a printhead that jets binder, similar to an inkjet printer. Parts are created from powder and binder, built up layer-by-layer. The parts produced are called green parts. These green parts are often post-processed by sintering in a furnace to fully solidify and densify them to achieve desired mechanical properties and final geometric characteristics.

New and continuing developments in additive manufacturing as well as research requirements motivates the development of an open-architecture binder jetting system that can be updated modularly, is capable of producing complex parts at reasonable scale, and which provides full control of the software and hardware to researchers and users. The development of such a system is described herein.

To demonstrate the research ability of the system and provide information on binder jetting parameters, the thesis also details the use of thermocouples and a thermal camera to gather data on the effects of infrared heating on powder bed temperature, used for in-situ curing to improve green part properties. The heating rate at the surface of the powder bed can exceed 8°C/s, even for relatively modest heater powers (400 W), and heater parameters can be directly related to the peak temperatures achieved in the bed, consistently producing peak temperatures of over 100°C for linear energy densities of 70 J/mm, providing data for evaporation in aqueous binders. The presence of binder caused substantial differences compared to dry powder, producing consistently lower heating rates until solvent evaporation, but having minimal effect on long-term peak temperatures. The thermal camera was able to produce qualitative data on the surface of the build bed, indicating that the temperature differences across the surface can be significant, on the scale of 10°C to 20°C.

Acknowledgements

Thanks to Prof. Mihaela Vlasea for providing the chassis and prior electronic work, done in collaboration with University of Waterloo technical staff and Parker Automation engineers, and Marc Wang for conceptualizing the current revision of electrical design and motion control, documenting the electrical connections, and developing the initial revisions of software for the binder circulation and heater control.

Thanks to Melody Gao, Zoe Kong, and Jay Shi for performing vital electrical, logistics, and software work during our final year as undergraduate students, during which the current machine's capabilities was a pipe dream and without whose contributions would likely still be the case. Thanks also to Sanjay Singh, who provided guidance on understanding complex electrical systems and organizing schematics, as well as Andy Barber, Neil Griffett, and Jim Merli, who provided electrical support during the initial development of the machine, and Neil Griffett and Bin Tan, for their ongoing support in ensuring the machine is properly certified.

Thanks to Caleb Shepherd Davis for setting up the Dropwatcher and binder circulation systems, without which development of binder jetting waveforms and testing of different binders would be impossible. Thanks to Mariah de Torres for continuing this work, and working with Daniel Juhasz to develop printing parameters with a variety of inks and binders with advanced piezoelectric printheads.

Thanks to Roman Boychuk for organization and planning, CAD support, mechanical and electrical design, equipment acquisition, and FDM printing assistance for various parts and pieces. Thanks to Edward Yang for developing the software for controlling a specialized syringe device for local binder deposition, IR sensor for temperature data, and carrying out microscope analysis for geometric measurements. Thanks to Daniel Juhasz for work on developing parameters for the binder circulation and printhead, a vital part of ensuring that the printer was both functional and accurate.

Dedication

To my family,
for their unending support
before, during, and (I'm sure) after.

Table of Contents

Author's Declaration ii

Abstract iii

Acknowledgements iv

Dedication v

List of Figures ix

List of Tables xvii

1 Introduction 1

1.1 Motivation - Objective 1: Development of Custom Machinery 2

1.2 Motivation - Objective 2: Experimentally-Driven Powder Bed Temperature Analytics 4

1.3 Thesis Structure 5

2 Background and Literature Review 6

2.1 Description and Industrial Applications 6

2.2 Open Architecture BJAM Systems 9

2.3 Powder-Binder Heating and Geometric Fidelity of Parts 15

3 Technical Description of Custom Binder Jetting Machine **18**
3.1 Overview . . . 21
3.2 Hardware Modules . . . 23
3.2.1 Gantry Positioning System . . . 23
3.2.2 Powder Beds and Roller . . . 25
3.2.3 Printhead and Binder Circulator . . . 28
3.2.4 Infrared Heater . . . 31
3.3 Software and Motion Control . . . 33
3.4 User Interface and Workflow . . . 35
3.5 Printing Capabilities . . . 37

4 Experimental Methodologies **40**
4.1 Temperature Measurement Setup . . . 40
4.1.1 Thermocouples and the Thermocouple Array . . . 40
4.1.2 Thermal Camera . . . 43
4.1.3 Material System . . . 43
4.2 Data Packages . . . 44
4.3 Data Collection Procedure . . . 45
4.3.1 Procedure Overview . . . 45
4.3.2 Detailed Steps . . . 47

5 Results - Measurements and Analysis **51**
5.1 Measurement - Descriptions of Data Visualization . . . 51
5.2 Measurement - Physical Reasoning and Lead-in . . . 57
5.3 Analysis - Impact of Infrared Heater on Dry Powder Bed . . . 58
5.3.1 Analysis - Effect of Heating Rate . . . 58
5.3.2 Analysis - Peak Temperatures . . . 69
5.3.3 Analysis - Cooling Rates . . . 79

5.4 Analysis - Impact of Aqueous Binder on Temperature Measurements . . . 89
5.4.1 Analysis - Heating Rates of Dry vs. Printed Layers . . . 89
5.4.2 Analysis - Peak Temperatures . . . 98
5.4.3 Analysis - Cooling Rates . . . 103
5.5 Analysis - Surface Temperature and Detectable Geometry . . . 109
5.5.1 Analysis - Visible Spatial Dependencies based on Vision Data Surface Measurements . . . 111
5.5.2 Analysis - Surface-to-Depth Temperature Deltas . . . 126
5.6 Dimensional Dependencies . . . 129

6 Conclusions and Future Work **131**
6.1 Conclusions . . . 131
6.2 Future Work . . . 132
6.2.1 Latency of Heater Impact . . . 132
6.2.2 Defect Detection and Geometric Fidelity . . . 132
6.2.3 Green Part Strength . . . 133
6.2.4 Multi-Material Printing and Localization . . . 133

References **134**

APPENDICES **138**

A LinuxCNC Configuration **139**
A.1 LinuxCNC INI File . . . 139

B G-Code **150**
B.1 G-Code for Standard Printing . . . 150
B.2 G-code for Temperature Measurements . . . 151

C Geometric Detection **153**

D Emissivity Compensation **162**

List of Figures

1.1 Proposed benefits for the development of flexible, open-architecture binder jetting systems. 3

2.1 Binder jetting steps, going from feedstock material to completed part, showing two alternative post-processing stages (sintering and infiltration) for achieving target density. Adapted from [11]. 6

2.2 Diagram suggesting alternate categorical breakdown for binder jetting parameters that affect part outcomes. Adapted from [19]. 7

2.3 Design of machine by Oropeza and Hart showing single print nozzle, supply of feed powder via platform/bed, and heat lamp. (The hopper dispenser is not used in their paper, but is available as an alternative to the powder platform for powder dispensing.) Adapted from [27]. 10

2.4 Design of machine by Lawrence et al., showing the single print nozzle, build platform, powder dispensing hopper, and side-view droplet camera. Adapted from [20]. 12

2.5 Design of machine by Chang et al., showing their "moving sled" design, in which the powder feed and build beds are moved under the roller and printheads. Adapted from [3]. 13

2.6 Design of machine by Persembe et al., showing a modified commercial binder jetting printer (Projet 660, 3D Systems), replacing the original thermal printheads (HP11, HP) with piezoelectric printheads (XAAR 128, Xaar). Arduino cluster and custom software allow greater control over printing. Adapted from [28]. 14

2.7 Design of machine by Oak Ridge National Laboratory, showing two gantries for the powder dispensing hoppers and printhead respectively. System contains multiple hoppers for multi-powder printing and vacuum nozzle for powder recovery. Adapted from [14]. 15

2.8 Relationship between initial binder saturation and drying time and effects on inter-layer adhesion and excess binder presence. Adapted from [25]. . . 16

2.9 Sensor schematic layout developed by Vest et al. for their data collection in SLM. Adapted from [33]. 17

3.1 Photo of the custom binder jetting machine. The printing area is the top half, while supporting electronics are placed in the lower cabinet. 20

3.2 Photo of the printing level, with powder beds, roller, and heater, as well as binder circulator visible. The printhead is not installed in this figure, but would be placed in a mount under the binder circulator. 21

3.3 Display of major steps in the printing of a part in binder jetting, prior to sintering and post-processing. Adapted from [36]. 22

3.4 CAD of gantry and printhead stages, showing powder feed and build beds as well as the reference directions. The roller and heater are underneath the horizontal part of the gantry and are not visible in this image. 24

3.5 Control schema for motors 25

3.6 CAD of roller, feed and build beds, and heater, with gantry removed. These modules are located underneath the gantry shown in Figure 3.4. 26

3.7 Photo of roller, feed and build beds, and heater. 27

3.8 Printhead and mount images 29

3.9 Photo of Dropwatcher setup 31

3.10 Infrared heater images 32

3.11 Heater Power Draw (W) vs. Input Current Signal (mA) 33

3.12 Diagram of major hardware components. Commands flow from software control into the major modules, with feedback from sensors sent back for electronic closed-loop control. 34

3.13 Axis GUI, a graphical front-end for LinuxCNC that provides a default implementation for machine control, with custom user interface elements implemented for the binder jetting machine shown on the right. 35

3.14 Example sliced image 36
3.15 PrusaSlicer settings, showing main modification for Starfire SG1024 printhead, 2.5 inch/63.5 mm print width with 1024 nozzles. 37
3.16 Example of a printed lattice (IWP Solid), 100 µm layer thickness, 1 cm by 1 cm sides. 38
3.17 IWP lattice solid model, generated by MSLattice [2]. 38
3.18 Example of a keychain print, 100 µm layer thickness, showing an example of a print failure due to feature size being too small. 39
3.19 Keychain solid model, designed by Sagar Patel and Jerry Ratthapakdee . . 39

4.1 Thermocouple hardware setup 41
4.2 CAD of thermocouple array plate. The thermocouple wires are fed through holes in the side and the junctions are pulled out through holes in the top. 42
4.3 Photo of thermocouples buried under SS316L powder, with the wires leading into the feedthrough point. The thermocouple junctions are barely visible above the surface of the powder. 42
4.4 Thermal camera mount 43
4.5 Sensor measurements and machine sequencing during dry experiments. This figure indicates the sequence of actions taken by the machine, thermocouple logger, and thermal camera, in order from top to bottom. 45
4.6 Sensor measurements and machine sequencing during printed experiments. Compared to the dry experiments, this has a printing step and an additional thermal camera capture. 46
4.7 Thermocouple indices and directions, showing the locations of the nine thermocouples with numbered callouts and relative directions in which powder spreading, heating, and printing occur. 48
4.8 Locations of Printed Circles 49
4.9 Experimental Parameter Coverage, Dry. Checkmarks indicate a combination of heater power and speed that was tested. 50
4.10 Experimental Parameter Coverage, Printed. Checkmarks indicate a combination of heater power and speed that was tested. 50

5.1 Example thermocouple data, showing temperature data over nine thermocouples taken at a heater power of 349 W and a heater speed of 5 mm/s. A zoomed-in view of the temperature trend across a single layer is shown below the full plot. 53

5.2 Procedure steps, dry experiments. Each layer consists of a heating step, a cooling down step, and a powder spreading step. No temperature measurements take place during the powder spreading step. Example taken with a heater power of 349 W and a heater speed of 5 mm/s. 54

5.3 Procedure steps, printed experiments. Each layer consists of a heating step, a cooling down step, a powder spreading step, and a printing step. No temperature measurements take place during the powder spreading and printing steps. Example taken with a heater power of 349 W and a heater speed of 5 mm/s. 55

5.4 Example thermal camera image, printed. Example taken with a heater power of 349 W and a heater speed of 5 mm/s at layer 15. 56

5.5 Example thermal camera image, dry powder. Example taken with a heater power of 349 W and a heater speed of 5 mm/s at layer 15. 56

5.6 Example of binder bleeding and elephant's foot defect in ceramic cuboid samples due to insufficient drying. Adapted from [23]. 58

5.7 Linear approximation of heating rate 60

5.8 Dry Heating Rate vs. Layer Index, 389 W, 5 mm/s, 79.86 J/mm for thermocouple 5 located at the center of the build bed. 61

5.9 Dry Heating Rate vs. Layer Index, 268 W, 5 mm/s, 53.56 J/mm for thermocouple 5 located at the center of the build bed. 62

5.10 Dry Heating Rate vs. Layer Index, 99 W, 5 mm/s, 19.78 J/mm for thermocouple 5 located at the center of the build bed. 63

5.11 Dry Heating Rate vs. Layer Index 64

5.12 Dry Heating Rate Normalized vs. Layer Index 65

5.13 Dry Heating Rate at Surface (0th Layer) vs. Linear Energy Density, proposed transition region highlighted. 66

5.14 Dry Heating Rate at Surface (0th Layer), Full vs. Linear Energy Density . 67

5.15 Dry Heating Rate across Thermocouples 4, 5, and 6, 389 W, 5.0 mm/s, 77.86 J/mm. One experiment is shown in blue, and one is shown in orange. 68

5.16 Example thermocouple data and corresponding per-layer temperature peaks of thermocouple 5, taken at a heater power of 349 W and a heater speed of 5 mm/s. 70

5.17 Well-fitted and poorly-fitted examples of peak temperature curves 73

5.18 Time Constants for Dry Heating Peaks 74

5.19 Averaged Peak Temperatures of Thermocouple 5 over last five layers vs. Linear Energy Density 75

5.20 Averaged Peak Temperatures over the last five layers (Thermocouple 4 to 6) vs. Linear Energy Density. This figure is for the thermocouple measurements in the center row, showing that the temperatures are highest in the center, as expected. 76

5.21 Averaged Peak Temperatures (Thermocouple 2, 5, 8) vs. Linear Energy Density. As noted previously, the bottom row of thermocouples (Thermocouple 7, 8, 9) are not fully covered by the heater pass. 78

5.22 Layer shifting defect of SS316L part intended to be cuboid. Adapted from [27]. 80

5.23 Peak-to-Trough Delta, 389 W, 5 mm/s, 79.86 J/mm for thermocouple 5. The orange line is the peak temperatures for each layer, and the blue line is the minimum temperatures for each layer, with the temperature indicated on the right axis. The dots indicate the difference between the peak and trough values, with the delta indicated on the left axis. 81

5.24 Peak-to-Trough Delta, 268 W, 5 mm/s, 53.56 J/mm for thermocouple 5. . 82

5.25 Peak-to-Trough Delta, 99 W, 5 mm/s, 19.78 J/mm for thermocouple 5. . . 83

5.26 Cooling Time Constants vs. Layer Index, 389 W, 5 mm/s, 79.86 J/mm for thermocouple 5. This indicates that the cooling is rapid for the earlier layers, when the thermocouples are closer to the surface. 84

5.27 0th Layer Cooling, 389 W, 5 mm/s, 79.86 J/mm for thermocouple 5. The temperature measurements for the cooling down period of the surface (0th layer), plus some additional measurements from the start of the next layer are shown. The fitted curve is also plotted. 85

5.28 14th Layer Cooling, 389 W, 5 mm/s, 79.86 J/mm for thermocouple 5. . . . 86

5.29 28th Layer Cooling, 389 W, 5 mm/s, 79.86 J/mm for thermocouple 5. . . . 87

5.30 Cooling Time Constants, 268 W, 5 mm/s, 53.56 J/mm for thermocouple 5. Compared to Figure 5.26, the time constants are higher, especially for the latter layers. 88

5.31 Dry and Printed Heating Rate vs. Layer Index, 389 W, 5 mm/s, 79.86 J/mm for thermocouple 5. The dry heating rates vs. layer index are shown in blue, while the printed heating rates are shown in orange. 90

5.32 Printed Heating Rate vs. Layer Index, 268 W, 5 mm/s, 53.56 J/mm for thermocouple 5. 91

5.33 Printed Heating Rate vs. Layer Index, 99 W, 5 mm/s, 19.78 J/mm for thermocouple 5. 92

5.34 Printed Heating Rate vs. Layer Index 93

5.35 Printed Heating Rate Normalized vs. Layer Index 94

5.36 Heating Rates at Surface (0th Layer) vs. Linear Energy Density. Dry and printed heating rates presented for comparison. Noted discontinuity occurs between 60 J/mm and 70 J/mm. 95

5.37 Heating Rates 0.75 mm deep (15th Layer) vs. Linear Energy Density . . . 96

5.38 Printed Heating Rate across Thermocouples 4 to 6, 389 W, 5 mm/s, 77.86 J/mm 97

5.39 Time Constants for Dry and Printed Heating Peaks 99

5.40 Averaged Peak Temperatures vs. Linear Energy Density 100

5.41 Averaged Peak Temperatures over the last five layers (Thermocouple 4 to 6) vs. Linear Energy Density. 101

5.42 Averaged Peak Temperatures over the last five layers (Thermocouple 2, 5, 8) vs. Linear Energy Density 102

5.43 Peak-to-Trough Delta, 389 W, 5 mm/s, 79.86 J/mm for thermocouple 5. . 104

5.44 Peak-to-Trough Delta, 268 W, 5 mm/s, 53.56 J/mm for thermocouple 5. . 105

5.45 Peak-to-Trough Delta, 99 W, 5 mm/s, 19.78 J/mm for thermocouple 5. . . 106

5.46 Cooling Time Constants, 389 W, 5 mm/s, 79.86 J/mm for thermocouple 5. Dry and printed results are presented for comparison. 107

5.47 28th Layer Cooling, 389 W, 5 mm/s, 79.86 J/mm for thermocouple 5. . . . 108

5.48 Thermal camera imaging overlaid on corresponding thermocouple data, dry powder, taken at a heater power of 349 W and heater speed of 5 mm/s. For each layer, two thermal images are captured: once before heating and once shortly after heating. The thermocouples indicate the temperature below the surface of the powder at a depth of 0.75 mm. 110

5.49 Thermal camera imaging overlaid on corresponding thermocouple data, printed powder, taken at a heater power of 349 W and a heater speed of 5 mm/s. For each layer, three thermal images are captured: once before printing, once after printing, and once after heating. The thermocouples indicate the temperature below the surface of the powder at a depth of 0.50 mm. 111

5.50 Dry powder after heating, high power, 0th and 29th layers 113

5.51 Dry powder after heating, moderate power, 0th and 29th layers 114

5.52 Printed bed after heating, high power, 0th and 29th layers 115

5.53 Printed bed after heating, moderate power, 0th and 29th layers 116

5.54 Printed bed after heating, low power, 0th and 29th layers 117

5.55 Row measurements of dry powder, high power, 0th and 29th layers 119

5.56 Row measurements of printed bed, high power, 0th and 29th layers 121

5.57 Column measurements of dry powder, high power, 0th and 29th layers . . . 123

5.58 Column measurements of printed bed, high power, 0th and 29th layers . . 125

5.59 Dry Surface-to-Depth Temperature Comparison, 389 W, 5 mm/s, 79.86 J/mm 127

5.60 Printed Surface-to-Depth Temperature Comparison, 389 W, 5 mm/s, 79.86 J/mm 128

5.61 Sample Diameters vs. Linear Energy Density 130

C.1 Sobel 2D Filter, 389 W, 79.86 J/mm 154

C.2 Canny Edge Detector, 389 W, 79.86 J/mm 155

C.3 Example Part with Gaps 156

C.4 Gap Test, Sobel 2D Filter 157

C.5 Gap Test, Canny Edge Detector 158

C.6 Gap Test, Raw Data 159

C.7 Subsurface Test, Raw Data 160
C.8 Subsurface Test, Sobel 2D Filter 161

List of Tables

4.1 Thermocouple Data Format Example 44

Chapter 1

Introduction

Binder Jetting Additive Manufacturing (BJAM) is an additive manufacturing (AM) technique in which parts are constructed layer-by-layer by precisely depositing an adhesive binder on a thin layer of powdered material within a build environment, using a device similar or identical to an inkjet printer. This printed cross-section is lowered and a fresh layer of powdered material is spread on top of it, usually with a blade or spinning roller, and the printing process is repeated until the part is complete. The part is then extracted from the build environment, and loose powder is removed, resulting in an unfinished "green" part. Green parts are fragile and generally not directly usable, and so the part is subjected to additional processing. For metal and ceramic parts, the green part is placed in a furnace to burn off the binder and sinter the powder particles together, which increases strength and density, and is the main post-processing step in producing the final part. Binder jetting is flexible in material selection, does not require support material during printing, has high practical size limits and good scalability (via multiple printheads, part stacking, and increased powder bed volume), occurs at near room temperature, and can use variable material composition through localized deposition of material suspensions [26]. However, it produces initially fragile parts that require significant post-processing, has higher surface roughness and lower part resolution compared to laser powder bed fusion, and are subject to significant shrinkage during sintering due to their initially low density, which can cause warping and thermal stresses [26].

Modern commercial binder jetting machines, like those produced by Desktop Metal, Markforged, and others, are highly capable production systems that can be effective in both industrial manufacturing and academic research. While many commercial binder jetting solutions exist, these machines come with limitations that lessen or restrict the scope of certain research applications, such as multi-material manufacturing. They are

also difficult to use with new peripherals as both hardware and software may not interface effectively with external modules. Open architecture binder jetting systems seek to solve some or all of these problems, with the goal of a self-designed and flexible interface, and acceptable print quality and throughput.

Several custom machines for research and development are present, primarily in the academic sector. A binder jetting system at MIT, developed by Oropeza and Hart, is a desktop machine for investigation into binder jetting process optimization and materials [27]. Another desktop machine is present at Brigham Young University, designed for use with external imaging and collecting video of the printing [20]. The HuskyJet at the University of Connecticut uses custom machinery for high throughput production, and has been demonstrated with the production of pharmaceutical tablets [3]. KU Leuven has developed their own customizations to a commercial 3D printer by replacing a 3DSystems machine's thermal printhead with a XAAR piezoelectric printhead for studying changes to printing procedures (adaptive layer thicknesses and voxel-based control) [28]. Oak Ridge National Laboratory has designed and constructed their own binder jetting system during one of their research investigations into multi-material printing, though funding and technical integration challenges resulted in its abandonment [14]. Low-cost, open source printers like the Oasis 3DP and Plan B are also present, with their designs and construction manuals freely available [9, 10].

The development of an open architecture binder jetting machine provides a customizable testbed for advancing process optimization with fine control over hardware and software, the study of multi-material printing, and the potential use of multiple sensor modalities to gather high-resolution data. A multi-nozzle printhead comparable to commercial machines allows for high-throughput printing and conditions similar to those in industrial production. Continued development will improve these capabilities and allow for more sophisticated research.

1.1 Motivation - Objective 1: Development of Custom Machinery

The primary motivation behind the construction and development of an open architecture binder jetting system is to create a modular machine that can be modified and adapted for current and future research goals, with components that can be added or removed to suit specific experiments or production processes. The granular control over the system allows some modules, like sensors, to be tightly integrated into the printing process, producing

higher-quality data. Some of the proposed research tracks include multi-material system development, process modification and control, and defect tracking for quality assessment.

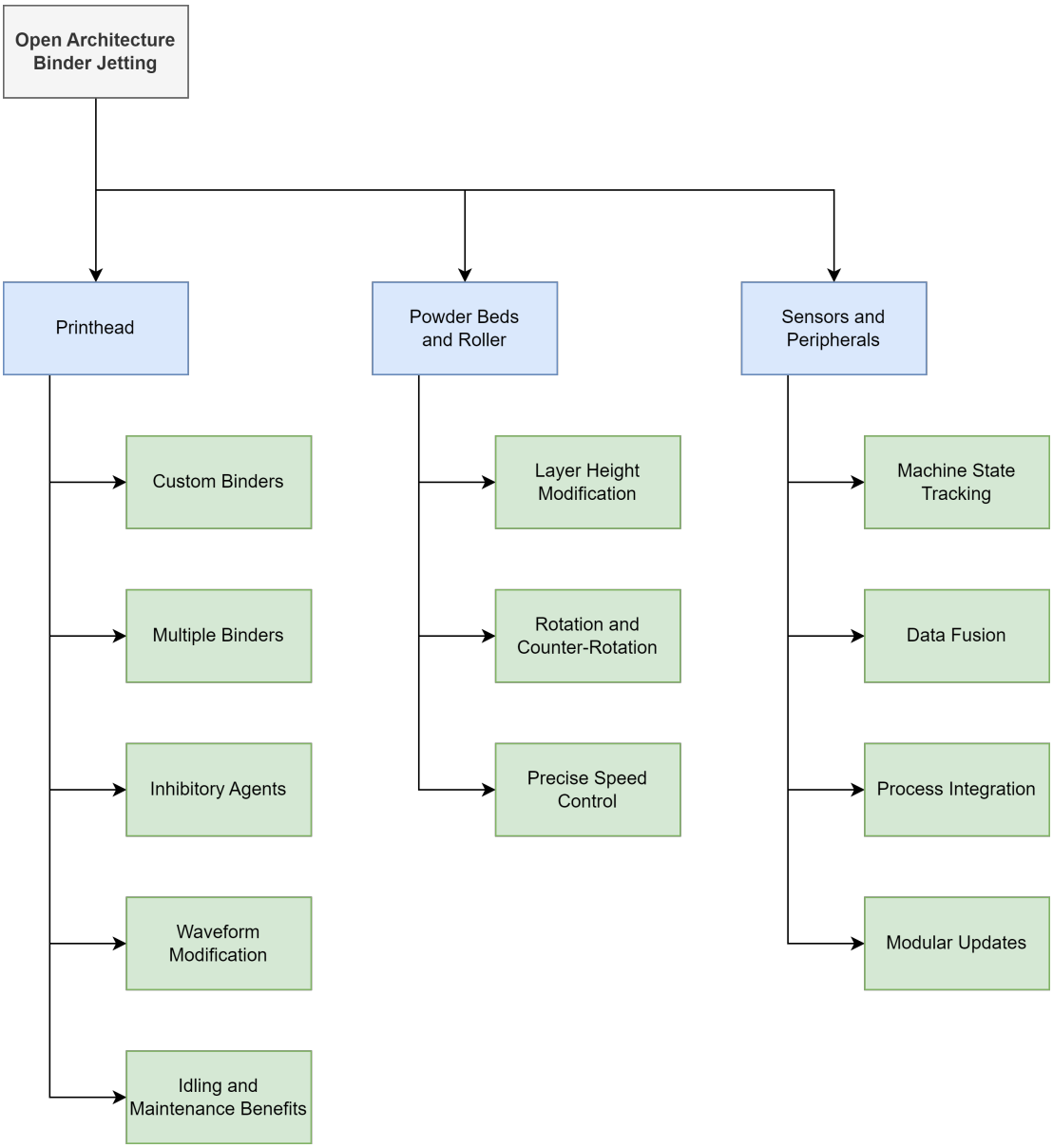


Figure 1.1: Proposed benefits for the development of flexible, open-architecture binder jetting systems.

As enumerated in Figure 1.1, the use of multiple powder beds and a printhead that can be used with many aqueous fluids potentially allows the use of multiple different materials beyond just a single powder and binder that is entirely burned off during the sintering process. The availability of metallic inks, either particle suspensions or metallic salts, makes using them with printhead or programmable nozzles a subject of interest. The use of inhibitors to control binder spreading through the powder substrate is also possible through this architecture. Process modification and control is another area of interest, and covers any changes to the steps used during printing (binder jetting, powder spreading, heating) and the resulting effect on the final part. Access to the underlying software makes modifying and testing new printing procedures relatively straightforward.

Defect tracking using a variety of sensor modalities is a path to improving the reliability of manufacturing, as well as investigating their causes - the close integration makes it easier to record defect data. In principle, a warning-system could be used to alert technicians to the presence of major defects, with the more ambitious goal of developing a closed-loop control system that identifies defects and modifies the process to correct them without requiring operator interference. Lastly, the open-nature of the machine allows it to be added to and updated as new research ideas and concepts enter the field, which will help maintain its relevance into the future.

The goals of custom machinery development are:

1. Generate initial parameters for motion control system and printhead for primary printing functions.
2. Build and test a system that can reliably produce green binder-jetted parts.
3. Develop a workflow for going from 3D models to printed parts.

Over the course of the work, such a binder jetting machine was developed, along with a workflow for converting 3D models to printed parts, successfully completing objective 1.

1.2 Motivation - Objective 2: Experimentally-Driven Powder Bed Temperature Analytics

The experiments described in this work cover the collection of temperature data from the surface and sub-surface regions of 316L stainless steel powder, both with and without binder. The goals of the experiment are:

1. Demonstrate feasibility of sensor integration and tightly coupled data collection to the machine control software.

2. Measure temperatures across different heater parameters, to quantify what temperatures are produced by different combinations of heater power and velocity.

3. Compare temperature relationships in the powder with and without binder.

The open-architecture, bespoke binder jetting system described here is used for these experiments, as its software is entirely under our control, allowing the code responsible for collecting data from sensors to interact directly with the code responsible for machine control. This allows full automation of the experimental procedure and ensures everything happens with precise timing and in a well-defined order.

In the methodology chapter, a combination of sensors are integrated and coupled with the machine to collect temperature data. In the results chapter, the temperature data is presented and compared across different heater powers and velocities, both with and without binder, resulting in the successful completion of objective 2.

1.3 Thesis Structure

The thesis consists of six chapters. Chapter 1 is the introduction, describing the binder jetting process and the motivation for the thesis work. Chapter 2 is the background and literature review, covering pre-existing work on open-architecture binder jetting systems and studies on powder-binder temperature. Chapter 3 is the technical description of the binder jetting machinery developed for research, including its hardware, software, and a brief comment on its capabilities. Chapter 4 describes the experimental methodology used in carrying out the study of the heater effects on SS316L powder and AquaFuse binder. Chapter 5 are the results of the this experimentation, describing various physical effects and their relationship with the heating parameters. Chapter 6 is the conclusion, summarizing the thesis, and proposes future work that may be done, some as extensions of the temperature studies, and others for improving part production.

Chapter 2

Background and Literature Review

2.1 Description and Industrial Applications

Binder jetting is a layer-by-layer powder-based additive manufacturing process, with the major steps going from starting material to finished part shown in Figure 2.1.

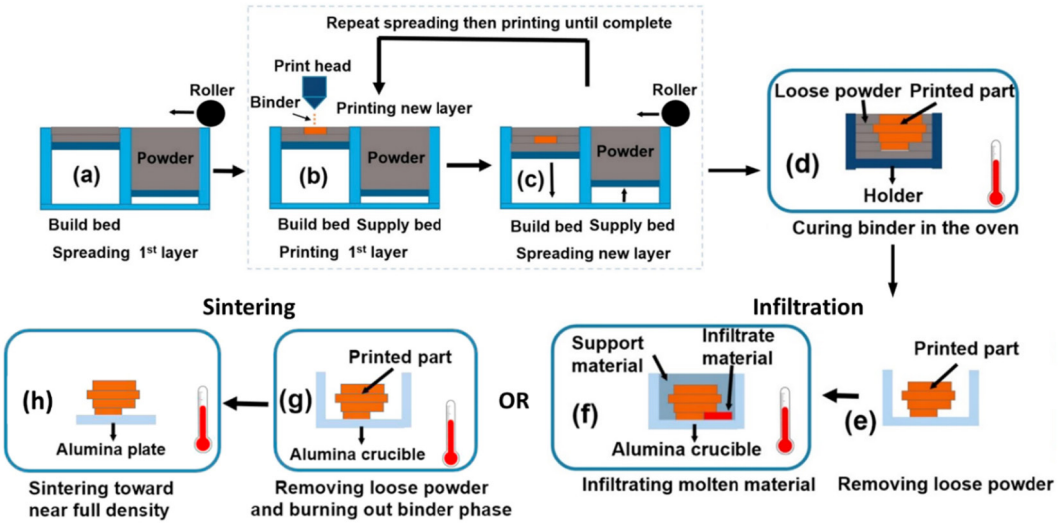


Figure 2.1: Binder jetting steps, going from feedstock material to completed part, showing two alternative post-processing stages (sintering and infiltration) for achieving target density. Adapted from [11].

There are many contributing factors to the final outcome of the binder jetting process studied in literature, that can broadly be separated into four major areas (suggested by Mostafaei et al. [26]), though such breakdowns are the subject of opinion, as in Figure 2.2:

1. Powder characteristics
2. Binder characteristics
3. Print parameters/settings
4. Post-processing and sintering phenomena

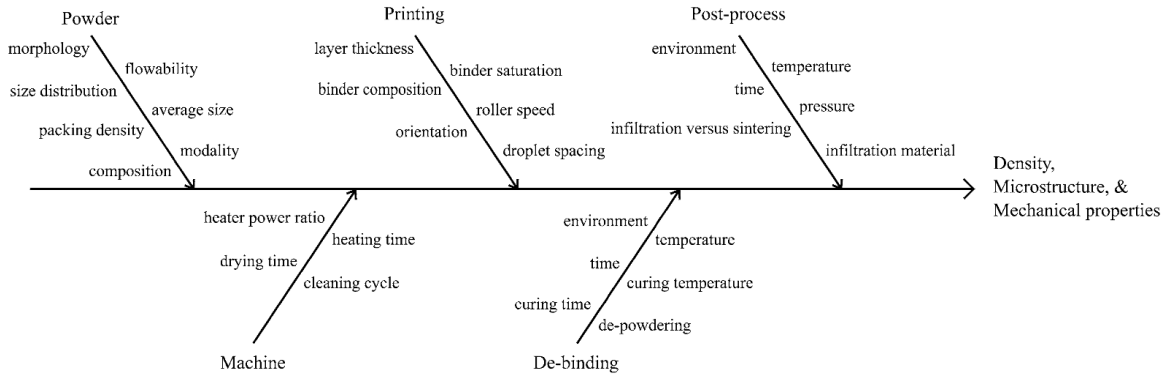


Figure 2.2: Diagram suggesting alternate categorical breakdown for binder jetting parameters that affect part outcomes. Adapted from [19].

The powdered material used in binder jetting has different impacts based on the powder size distribution and particle morphology, which affect the formation of thin layers of powder and the density of both the powder bed and the green part (which in turn affects the sintered part). In particular, spherical particles are generally preferred due to their ability to achieve higher packing densities and better flowability during spreading [26]. Small particles have higher green density and so generally experience less shrinkage compared to parts with lower green density, but have higher interparticle forces and can agglomerate in the powder bed [26].

Binders can be described by their mechanism of binding (acid-base reaction, metal salt re-crystallization or displacement, solvent evaporation), their interactions with the powdered material, and their fluid properties, which impact both their jetting and imbibition behaviours [26].

In printing, parameters of note include the layer thickness, which defines the resolution in the vertical direction as well as interacting with the powder size and flowability - ultimately affecting the both the green and sintered density [26]. The speed at which the roller moves over the powder bed, as well as the rotational speed of the roller, affect the spreading quality and in the case of insufficient powder homogeneity, can result in negative effects like layer delamination [26]. The level of binder saturation in the powder bed affects the strength of the part as well as its geometric accuracy, and the degree to which binder spreads within the powder is affected by the powder density and morphology [26]. Heater power ratio and drying time affects finished part properties, and optimal drying improves dimensional accuracy and surface finish [26]. Lastly, print orientation affects strength and surface quality, due to anisotropic properties caused by the powder spreading and printing steps [26].

Binder jetting additive manufacturing is a versatile additive manufacturing process used in a variety of industrial sectors. For example, it can be used to create sand molds with highly complex geometry that would be impractical or uneconomical to create with other methods - it can be leveraged and used in pre-existing, conventional manufacturing [36]. It has also been used in the aerospace and medical sectors for the creation of low-weight parts - being able to produce complex internal structures and highly customized shapes [26]. It also has applications in ceramics manufacturing, being able to join ceramic particles at room temperature, and thus avoiding some issues with thermal stresses that would impact other additive manufacturing processes [13]. Binder jetting has excellent material flexibility overall [26].

Laser powder bed fusion techniques, by comparison, use a laser that passes over a metal powder bed to rapidly fuse the metal powder into a solid metal part. These parts have very good geometric fidelity and density (higher than is possible with binder jetting) [26]. However, these parts are expensive to produce due to specialized machinery requirements and the use of inert gas atmospheres to avoid oxidation, and can develop internal stresses due to the large temperature gradients that occur during manufacturing [7]. Binder jetting additive manufacturing does not (and cannot) produce parts of the same accuracy due to the nature of fluid deposition - practical size limitations of droplet size and the tendency of fluid to soak into and spread out slightly reduce green part accuracy [26]. Furthermore, since the green part is not at full density, it can shrink and distort significantly during sintering [26]. However, its operating costs are lower (compared to single laser powder bed fusion) and its capability for parallelization is higher [18], making it better suited for larger numbers of small-to-medium sized parts that are minimally affected by shrinkage (when used in tandem with sintering models to estimate the final net shape) [26].

Existing challenges in binder jetting include identifying and fixing the causes of uneven

powder spreading, and predicting the shrinkage and distortion that occurs during sintering [36], as well as the presence of internal defects and voids after sintering [26].

2.2 Open Architecture BJAM Systems

As previously described, the usage of open-architecture equipment created in internal research development programs is not new, and some examples of this type of work can be considered and compared to that presented in this thesis.

In 2021, Oropeza and Hart presented a small-scale binder jetting printer for laboratory work, combining a previous modular testbed for investigating powder spreading with a Microfab piezoelectric nozzle and drive, which dispenses binder from a single nozzle that passes over the powder bed [27], shown in Figure 2.3.

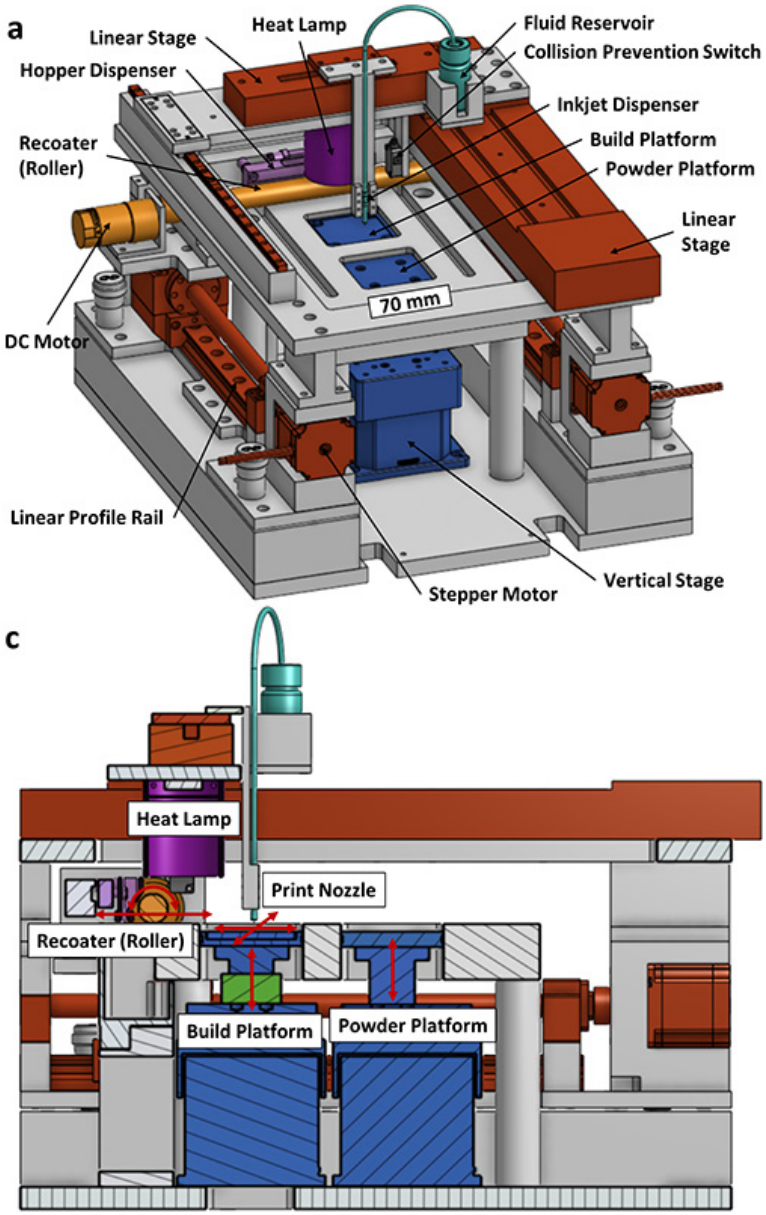


Figure 2.3: Design of machine by Oropeza and Hart showing single print nozzle, supply of feed powder via platform/bed, and heat lamp. (The hopper dispenser is not used in their paper, but is available as an alternative to the powder platform for powder dispensing.) Adapted from [27].

The single-nozzle capability is not industrially-practical due to limited throughput, but allows for showcasing basic principles in BJAM. Along with displaying general printing capabilities, they demonstrated the ability to apply an infrared heating source and measure the temperature status of the powder bed via a thermocouple above the powder as well as a thermal camera, which is significant for measuring binder curing data. In their experiments, a SS316L powder with a 15-45 µm size distribution and spherical morphology was used with a polyethylene glycol binder. The heating results indicated that the 250 W heating lamp used was able to reach a temperature of 100°C over the build bed in 8 seconds, and a temperature of 200°C in 48 seconds, noting that a temperature of 100°C is enough to dry many common solvents and exceeds the glass transition temperature of commonly used polymers [27].

Similar to our study, this work uses a similar gas-atomized powder with the same size distribution of 15-45 µm and high sphericity, and an AquaFuse polyethylene glycol binder. The powder spreading during the experiment was performed with a counter-rotating roller (roller spinning in the same direction as motion) at 250 RPM and 5 mm/s, which is described as typical compared to studies that made use of the commercial ExOne Innovent+ machine [27]. The temperatures reached in the study are suitable for the process goals of drying and curing common binders, and the powder bed temperatures achieved (80°C to 100°C) are comparable to some commercial systems, like the ExOne R2 [26]. The Microfab MJ single nozzle line, while not capable of the same productivity as multi-nozzle printheads, has a nozzle diameter of between 20 to 80 µm, compared to the ExOne Innovent+'s 10 to 30 µm diameter [27]. The Microfab nozzle is capable of a jetting frequency of up to 1 kHz, while the printhead used in our testing (Starfire SG1024MA/2C, Fujifilm) is technically capable of much higher (12 kHz) [17], though such jetting frequencies are impractical for our uses (requiring toolhead speeds in excess of 600 mm/s). In practice, our jetting frequencies are comparable to those used in this study. Overall, while not directly comparable to many industrial systems, the hardware selected is capable of achieving many parameter ranges typical of commercial machinery.

In 2022, researchers at Brigham Young University produced and described a system [20] that is described as somewhat similar to that built by Oropeza and Hart [27], but with a focus on external imaging, making use of an exposed build bed for use with high-speed visible light cameras and X-ray synchrotrons for studying the liquid-powder interaction, shown in Figure 2.4.

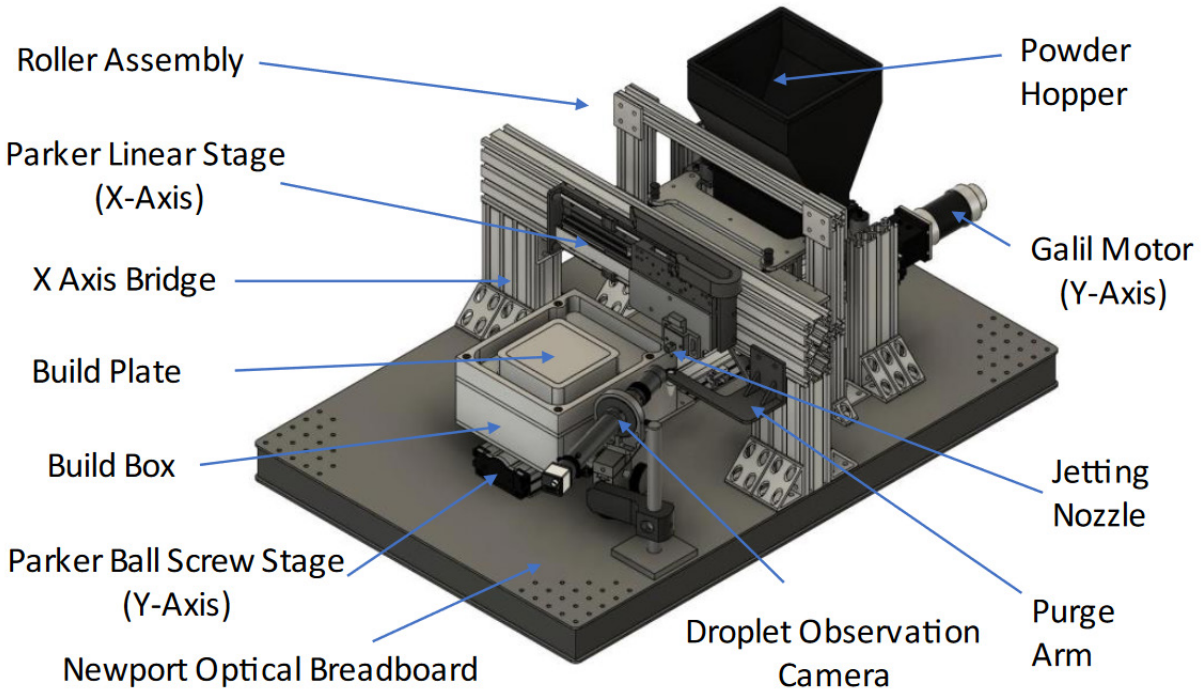


Figure 2.4: Design of machine by Lawrence et al., showing the single print nozzle, build platform, powder dispensing hopper, and side-view droplet camera. Adapted from [20].

It uses a single Microfab nozzle for printing, with a strobe light and camera set to capture jetted droplets, allowing for testing of droplet velocity and size in-flight. This machine only had accuracy validation performed, using a SS316L powder with a average diameter of 10.0 µm and an unspecified binder [20]. By comparison, the machine described in our work is not as well-suited for side imaging in-process due to the powder beds being surrounded by a granite table, but top-down imaging of the powder bed is still possible. Additionally, the experimental work related to droplet measurements is possible with our hardware with an external equipment setup called a Dropwatcher, in which the printhead is fixed into a strobe light and camera rig. This BYU system does not contain a heat lamp due to their primary focus of imaging droplets in-flight and printing accuracy, rather than printing full parts; however, they include the possibility of integrating a heat lamp for further experimentation in the future [20].

Chang et. al. at the University of Connecticut used three piezoelectric printheads for aqueous inks (Starfire SG1024/MA, Fujifilm) in their pharmaceutical tablet printer [3], shown in Figure 2.5.

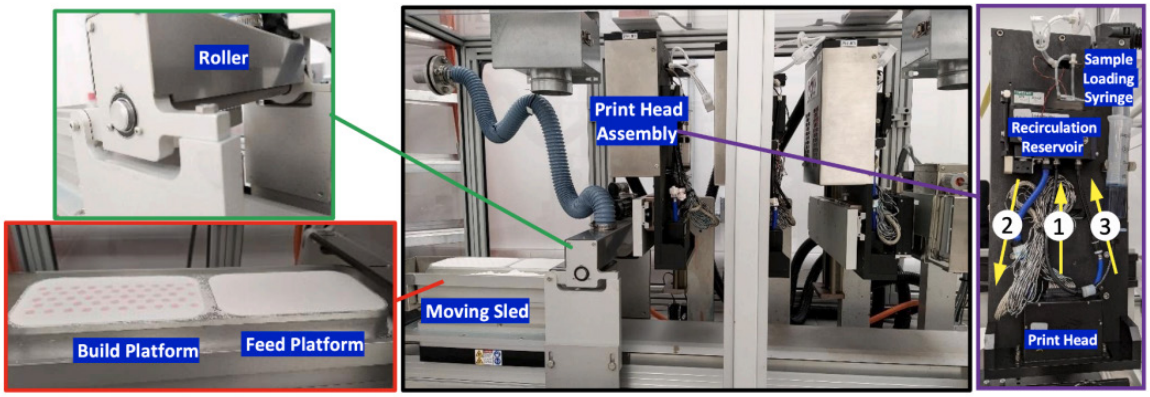


Figure 2.5: Design of machine by Chang et al., showing their "moving sled" design, in which the powder feed and build beds are moved under the roller and printheads. Adapted from [3].

Due to the different target application, the materials used are a lactose monohydrate/copovidone (Kollidon® VA64) powder mix and an aqueous binder containing 5% VA64. As their focus is on productivity and optimization of dissolvable pills, their focus was on throughput and the impact of process parameters on tablet characteristics like friability and disintegration time [3]. Notably, a nearly identical printhead model (Starfire 1024MA/2C, Fujifilm) was used in our work.

Another example using full printheads (as opposed to single nozzles) are the one developed at KU Leuven, which uses a XAAR 128 printhead with 128 nozzles, tested with a polymethyl methacrylate powder and a acetophenone/butanone binder (viscosity-modified with polyethylene glycol) to examine its resolution and print quality [28], shown in Figure 2.6.

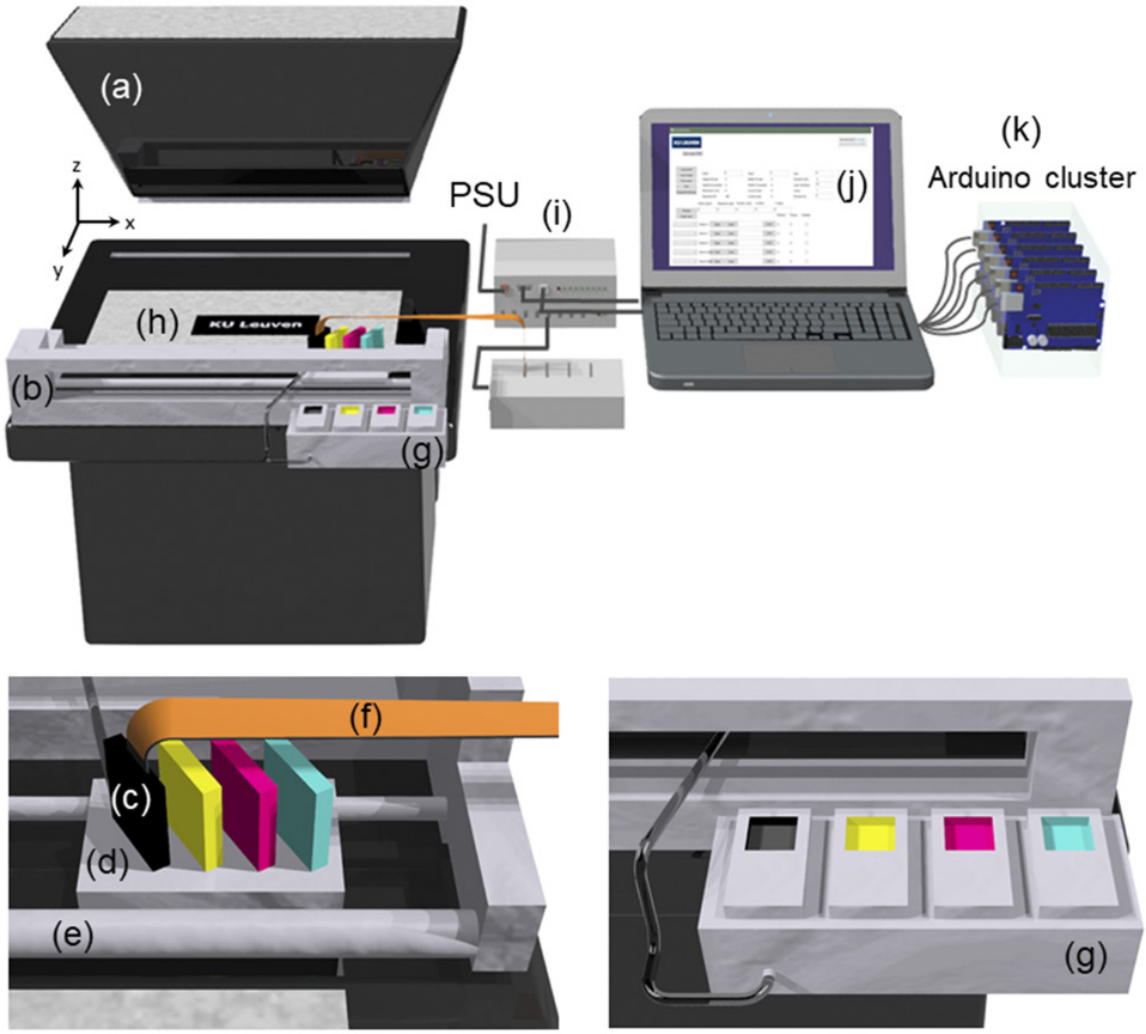


Figure 2.6: Design of machine by Persembe et al., showing a modified commercial binder jetting printer (Projet 660, 3D Systems), replacing the original thermal printheads (HP11, HP) with piezoelectric printheads (XAAR 128, Xaar). Arduino cluster and custom software allow greater control over printing. Adapted from [28].

Oak Ridge National Laboratory has also attempted a multi-material powder bed printing setup, which was assembled but not fully tested, noting struggles with printhead-motion system integration, combined powder dispensation-recovery system, and the fluid supply with associated pumps and sensors [14], shown in Figure 2.7. It was concluded that these

issues were unresolvable with their available resources, and the project was abandoned, with the goal of re-evaluating the multi-material research later [14].

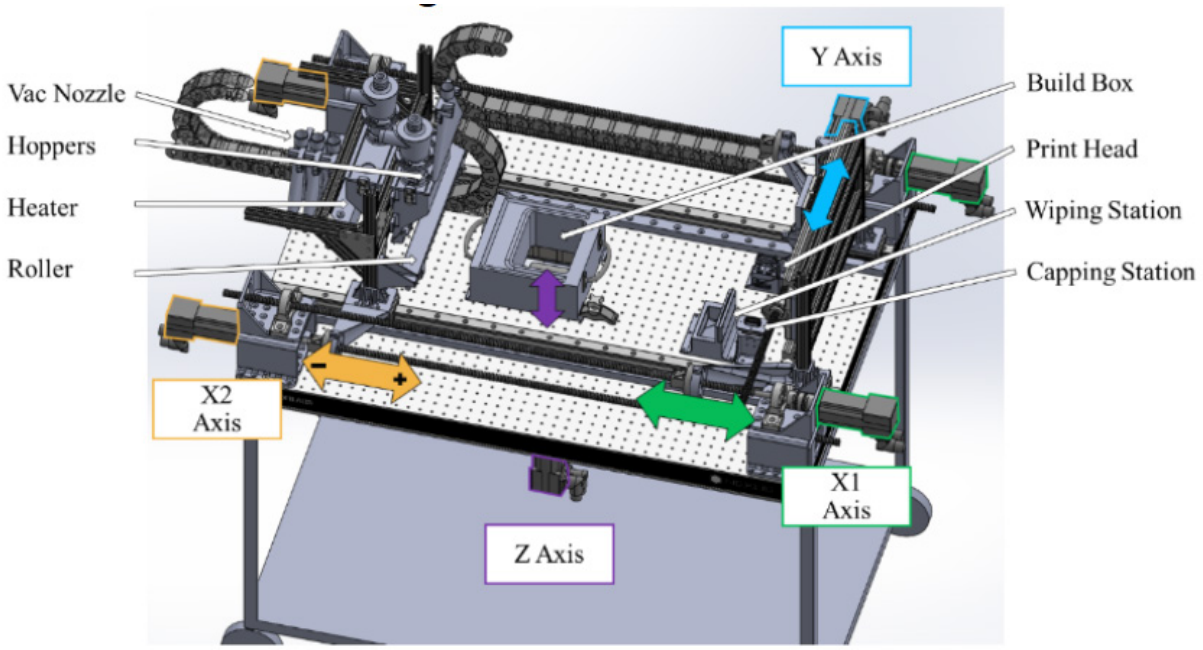


Figure 2.7: Design of machine by Oak Ridge National Laboratory, showing two gantries for the powder dispensing hoppers and printhead respectively. System contains multiple hoppers for multi-powder printing and vacuum nozzle for powder recovery. Adapted from [14].

2.3 Powder-Binder Heating and Geometric Fidelity of Parts

Many studies on the heating of the powder-binder material focus on the sintering step, while the curing of binder within the powder bed via the heater is described only in general terms (that it impacts geometry, shrinkage and surface finish) [26], or indirectly, for its effects on binder saturation [22]. Chen and Zhao generated an optimization model for directly relating heater parameters to part outcomes, and indicated that non-optimal drying time resulted in greater shrinkage overall, and proposed the mechanisms of insufficient binder penetration for short times causing increased porosity and shrinkage during sintering, and

over-drying for long times causing shrinkage during curing [4]. Mostafaei et al. also looked at the impact of drying time, and described a similar phenomenon relating optimal drying time to binder saturation, with the proposed relationship shown in Figure 2.8. [25].

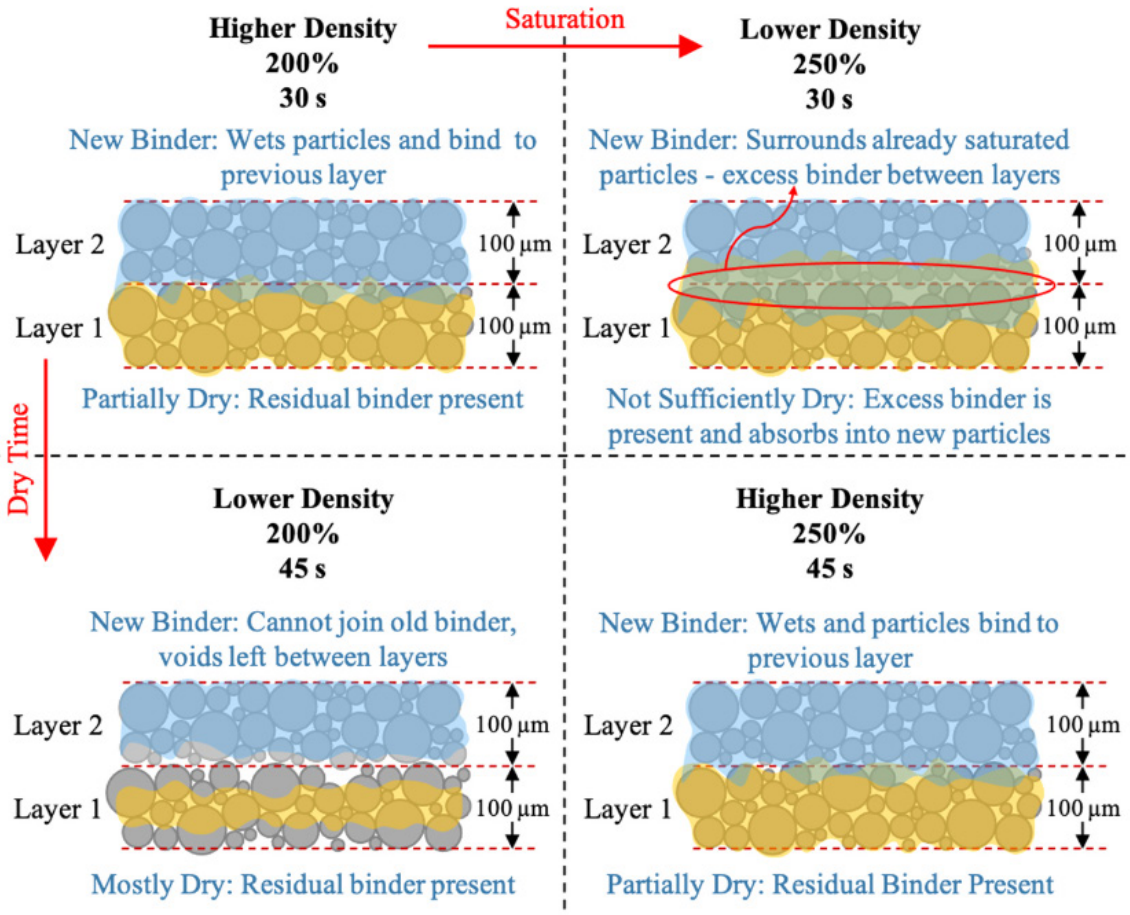


Figure 2.8: Relationship between initial binder saturation and drying time and effects on inter-layer adhesion and excess binder presence. Adapted from [25].

Crane examined the impact of heated versus non-heated powder-binder material and found that heating powder had a positive impact on both the geometric fidelity of parts as well as compliance with the target mass (due to avoiding bleeding that would join additional powder not in the part), and suggested that this may be due to the drying reducing the binder saturation and thus limiting bleeding, as well as the elevated temperature potentially causing a increase in the equilibrium limit of saturation [8].

Temperature measurements in powder beds are measured with a combination of contact and non-contact methods. For example, Oropeza and Hart used a single thermocouple and infrared camera in their binder jetting system to measure the temperatures achieved in the powder bed [27]. Crane used a pyrometer to calibrate heat lamp power to reach a target temperature in his study on drying conditions [8].

Lastly, while not directly relevant to powder bed temperature measurements, Vest et al. developed a high-performance temperature sensor setup, with multiple thermocouple amplifiers and central microcontroller shown in Figure 2.9 for collecting data from multiple thermocouples for their open-architecture SLM machine [33], similar to the setup used in this work, providing a potential path for future higher-resolution capture of thermocouple data.

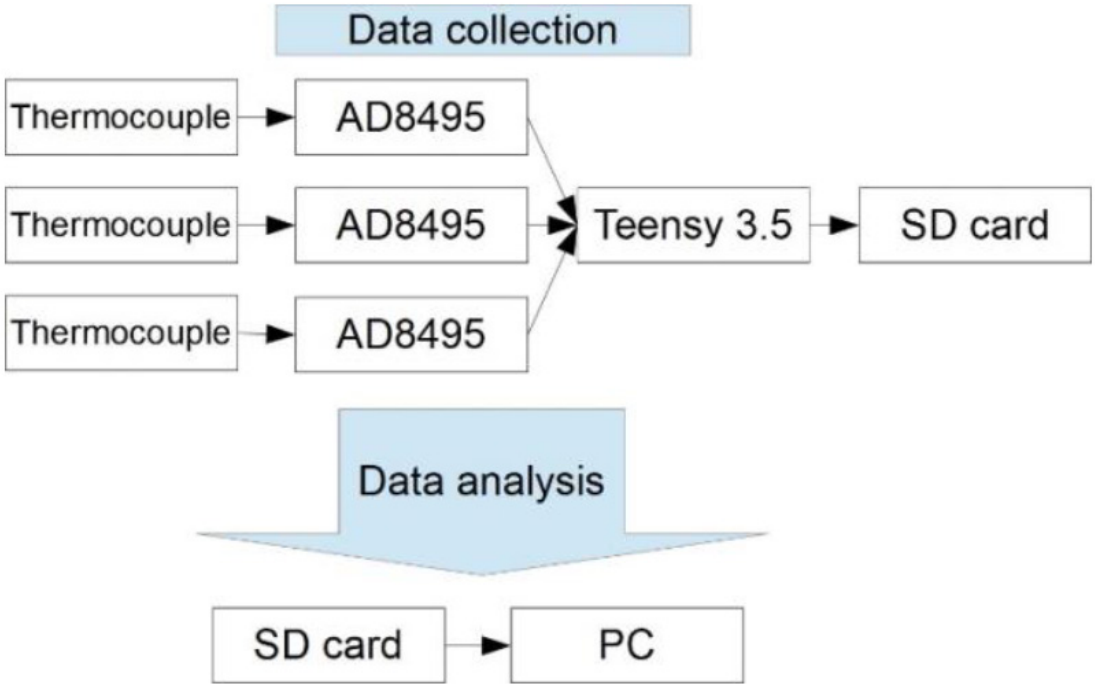


Figure 2.9: Sensor schematic layout developed by Vest et al. for their data collection in SLM. Adapted from [33].

Chapter 3

Technical Description of Custom Binder Jetting Machine

This chapter covers a technical description of the custom, open-architecture binder jetting machine developed at the Multi-Scale Additive Manufacturing Lab (MSAM) at the University of Waterloo, starting with an overview and explanation of the major functional components, then moving onto the software, control schema, and user interface used to control the machine, and concludes with a description of its printing capabilities and some example metal 3D prints.

The upper portion of the machine contains all-round viewing windows displaying the printing area. It is where the powder and binder is loaded, where printing occurs, and where printed parts are unloaded. The major functional components of the machine are all visible here. The printing area lies on top of a granite slab for vibration damping and rigidity, and uses aluminum extrusions as structural members.

The lower portion of the machine is mostly closed off by sheet metal panels, with technician access through the doors at the front. It contains the supporting electronics and electrical wiring needed for the motors, printhead support electronics, motion controllers, etc. and is not accessed during normal usage.

The hardware, including the motors, gantry design, and powder beds, were designed and assembled by other researchers and technical staff. My contribution was the replacement of the original motion control hardware (PMAC 2 Turbo, Delta Tau) with a more extensible alternative (7I96, Mesa Electronics) that was selected by Marc Wang. The corresponding electrical work and rewiring required to support this change was done by myself, Marc Wang, and Melody Gao. The older Labview machine control software was replaced with

LinuxCNC, an open-source CNC machine control software. The calibration of control parameters, including PID tuning, as well as programming of printing steps was performed by me. Printhead software was programmed by Marc Wang and myself. Software to control the heater was programmed by Marc Wang and Edward Yang.

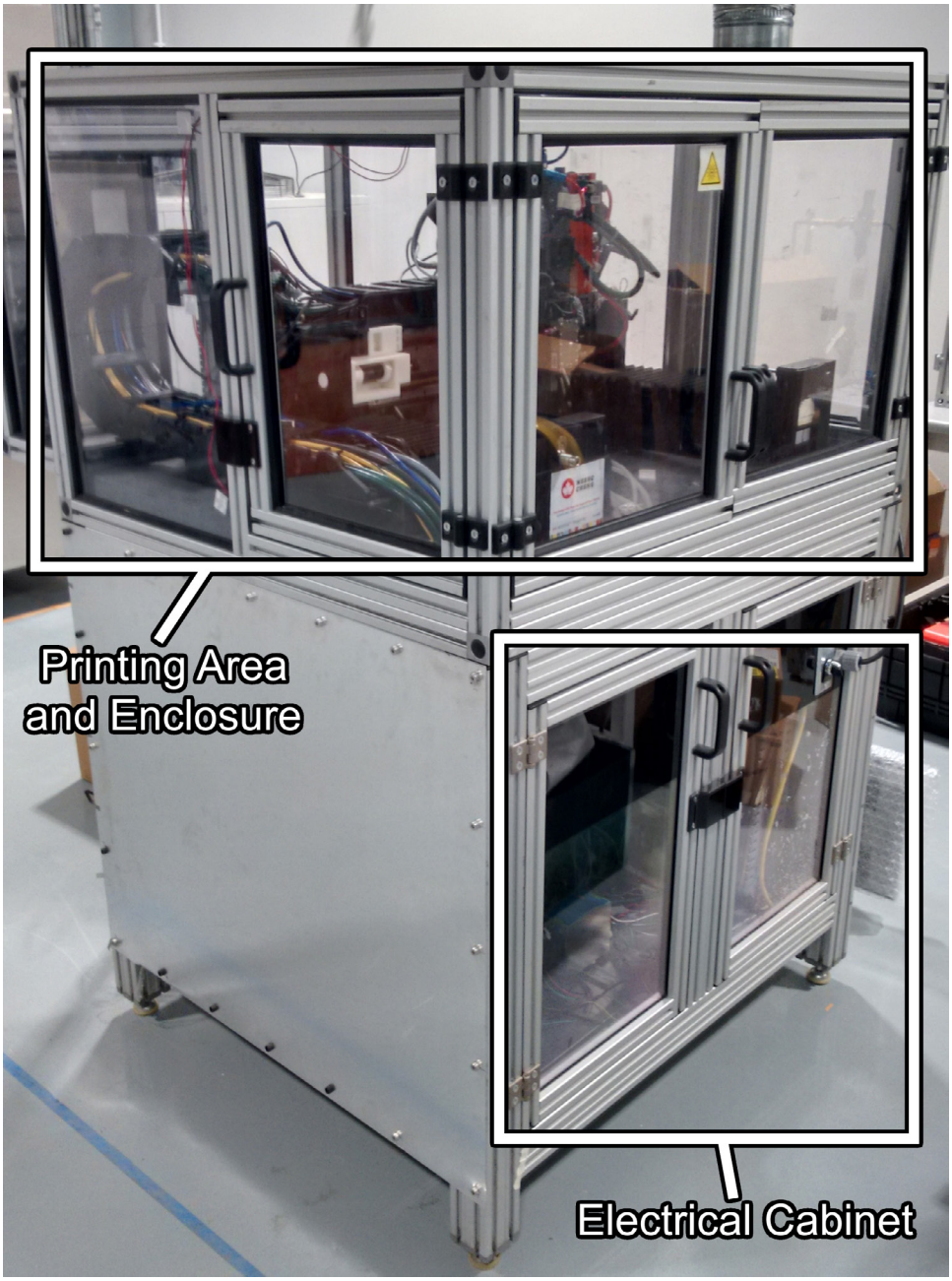


Figure 3.1: Photo of the custom binder jetting machine. The printing area is the top half, while supporting electronics are placed in the lower cabinet.

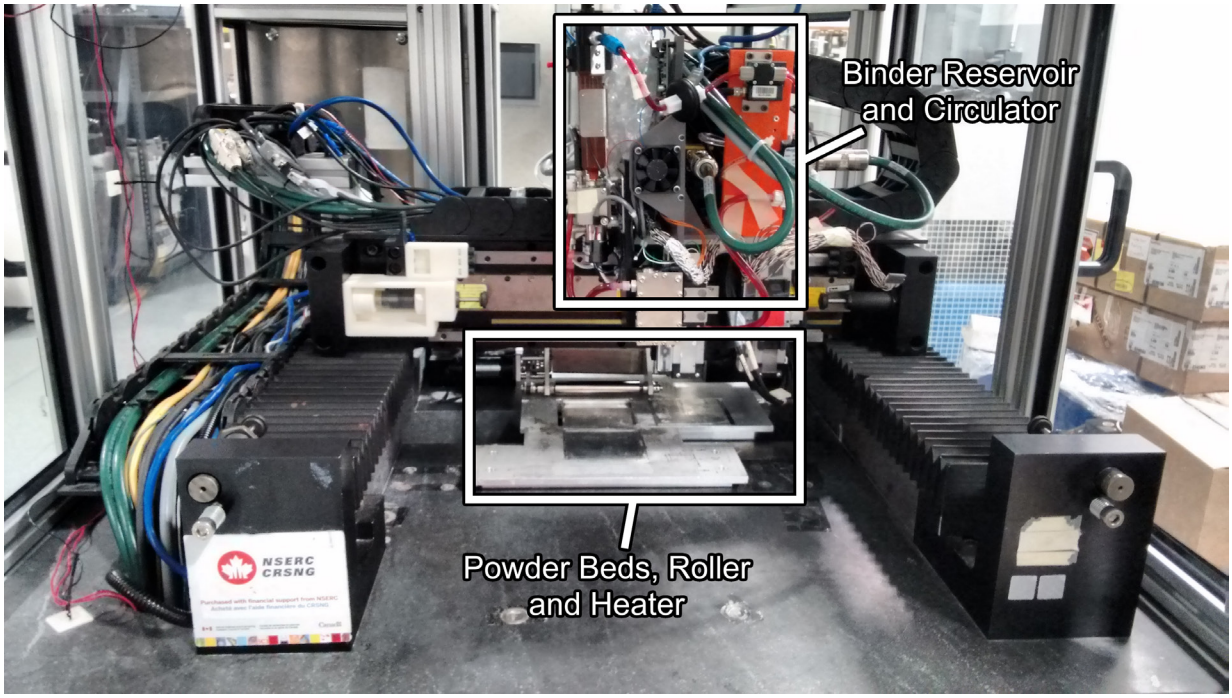


Figure 3.2: Photo of the printing level, with powder beds, roller, and heater, as well as binder circulator visible. The printhead is not installed in this figure, but would be placed in a mount under the binder circulator.

3.1 Overview

The binder jetting system uses a mobile gantry to move the printhead and powder spreader (roller) in the XY plane. The printhead is placed onto a vertical stage that moves it up and down, controlling the distance of the printhead to the build bed powder surface. The printhead is affixed to a fluid handler that provides an external reservoir and maintains the correct fluid pressure for printing. Feed beds are used to provide powder to the build bed. An infrared heater is used to heat the printed regions of the build bed.

The major functions of the system and the components that carry them out can broadly be divided into four groups:

- Positioning: moving the printhead and powder spreader to the correct places using a gantry

- Powder Movement: moving powder from a feed bed to the build bed
- Printing: jetting binder via the printhead and associated fluid handler that stores and circulates binder
- Heating: applying heat to dry and cure the binder after jetting

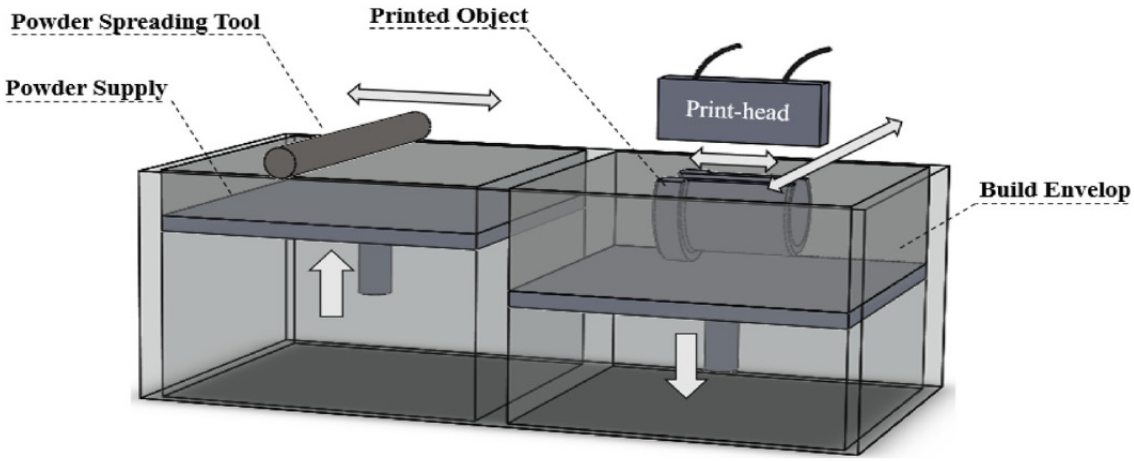


Figure 3.3: Display of major steps in the printing of a part in binder jetting, prior to sintering and post-processing. Adapted from [36].

The typical sequence that occurs during the printing of a single layer is as follows.

1. Move the positioner so that the roller is at the rear of the machine.
2. Raise the feed bed and lower the build bed, and use the roller to push powder from the feed bed to the build bed.
3. Move the positioner so that the printhead is over the build bed, and lower its vertical stage to the correct printing distance.
4. Send printing data to printhead, and move the printhead over the build bed and powder to jet binder.
5. Raise the printhead vertical stage to move the printhead out of the way.

6. Turn on the heater, and move the heater over build bed to dry and cure binder.

7. Turn off the heater.

The sequence above can be parameterised (changing layer height, heater power, etc.) to modify the print characteristics. Different procedures can be used depending on the experiment to be carried out.

3.2 Hardware Modules

3.2.1 Gantry Positioning System

The positioning module, also referred to as the gantry system, is responsible for moving the printhead during printing, the roller during powder spreading, and the heater during heating. It consists of a mobile gantry moved by two large linear motors (Trilogy T2S ironless linear motors, Parker Automation), which are described as "unwrapped" rotary motors using electronic commutation. The printhead stage moves perpendicularly to this, allowing for traversal motion in the XY plane. The printhead is located on an independent vertical Z-stage that allows for control of the standoff height and distance to the powder surface. The vertical stages use linear positioners (Parker Automation, 400XR) that are comparatively low power compared to the larger motors that power the gantry. The encoders on the XY axes have a resolution of 1 µm (RGH24X linear encoder, Renishaw), while the encoders on the vertical stages have a resolution of 0.5 µm (RGH24Z linear encoder, Renishaw).

The motor drives (Aries AR, Parker Automation) are connected to 240 VAC, providing the high power required. The drives use combination Hall effect/encoder commutation, and provide an internal (high-frequency) current and velocity control loop that the outermost positional control loop feeds into.

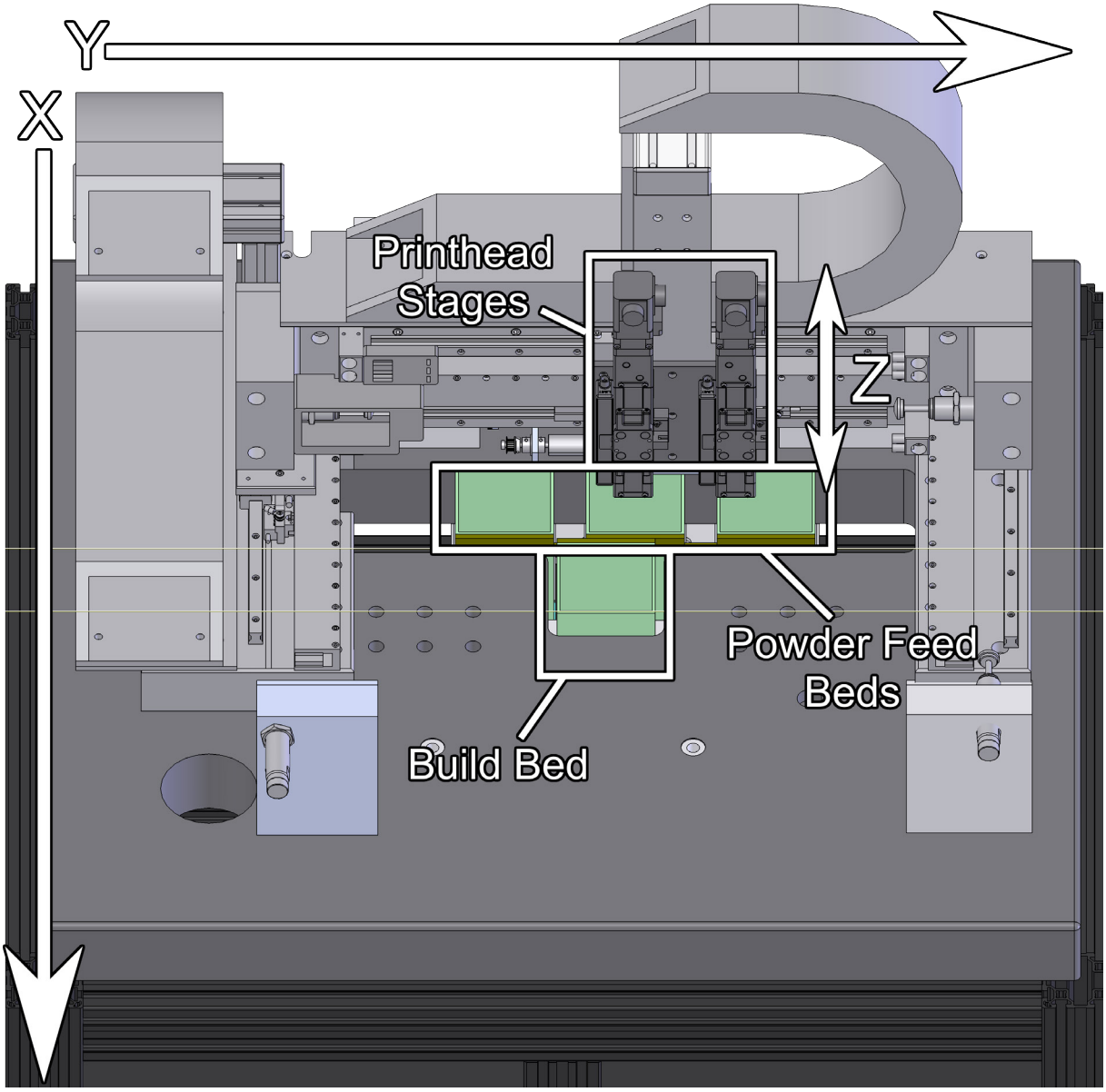


Figure 3.4: CAD of gantry and printhead stages, showing powder feed and build beds as well as the reference directions. The roller and heater are underneath the horizontal part of the gantry and are not visible in this image.

The positioning system uses encoders for position feedback and limit switches for safety. Software control provides both independent jogging and pre-programmed movements. Cas-

cade control is used, with the desktop software providing input to the position PID, which is used to provide input to the velocity and current PIDs on the servo drives. Calibration of the PID, feedforward, and biases are done manually, by examining the error function through the software oscilloscope and modifying the values to minimize it, with the gains entered into a configuration file, shown in Appendix A. Presently, the XY positioner has a precision of about 20 to 40 µm, and an upper practical speed of about 100 mm/s.

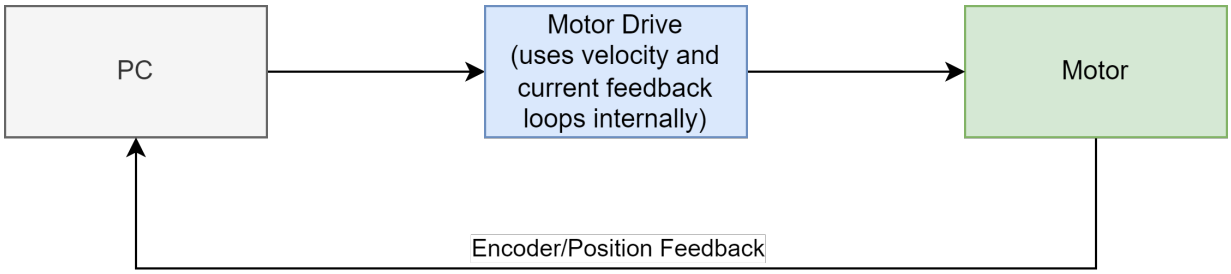


Figure 3.5: Control schema for motors

During printing, the printhead moves in the left-right direction, along the Y-axis, to complete its printing passes. During heating and powder spreading, the gantry moves from its rearward position to the forward position, along the X-axis.

3.2.2 Powder Beds and Roller

The powder beds contain powdered material used during printing. In its current configuration, it contains two feed beds and one build bed. In printing, the feed bed is aligned with the build bed and raised to supply powder, while the build bed is lowered by a corresponding amount. The roller spins and slowly passes over the feed bed and build bed to push the powder into the build bed, before returning to its original location.

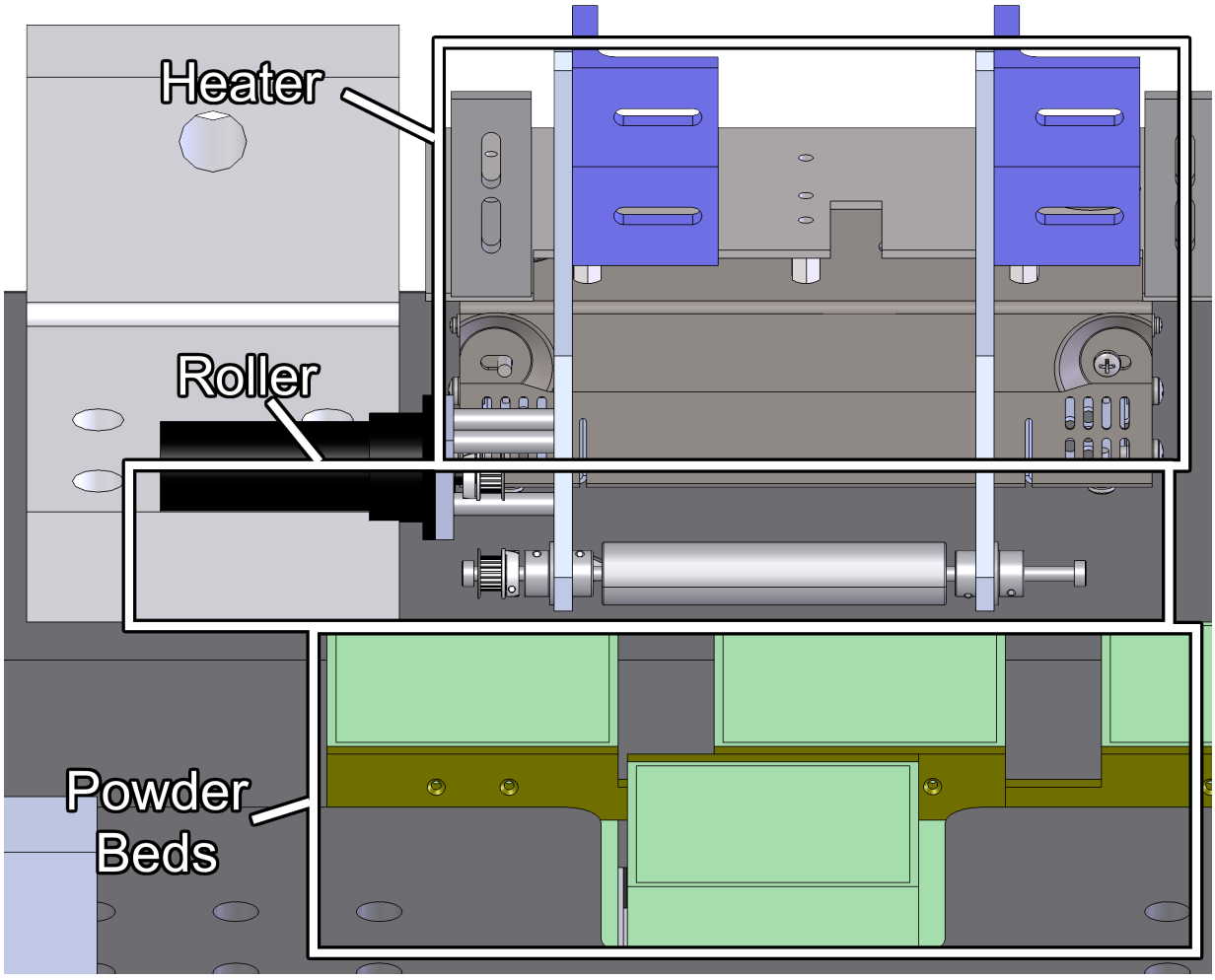


Figure 3.6: CAD of roller, feed and build beds, and heater, with gantry removed. These modules are located underneath the gantry shown in Figure 3.4.

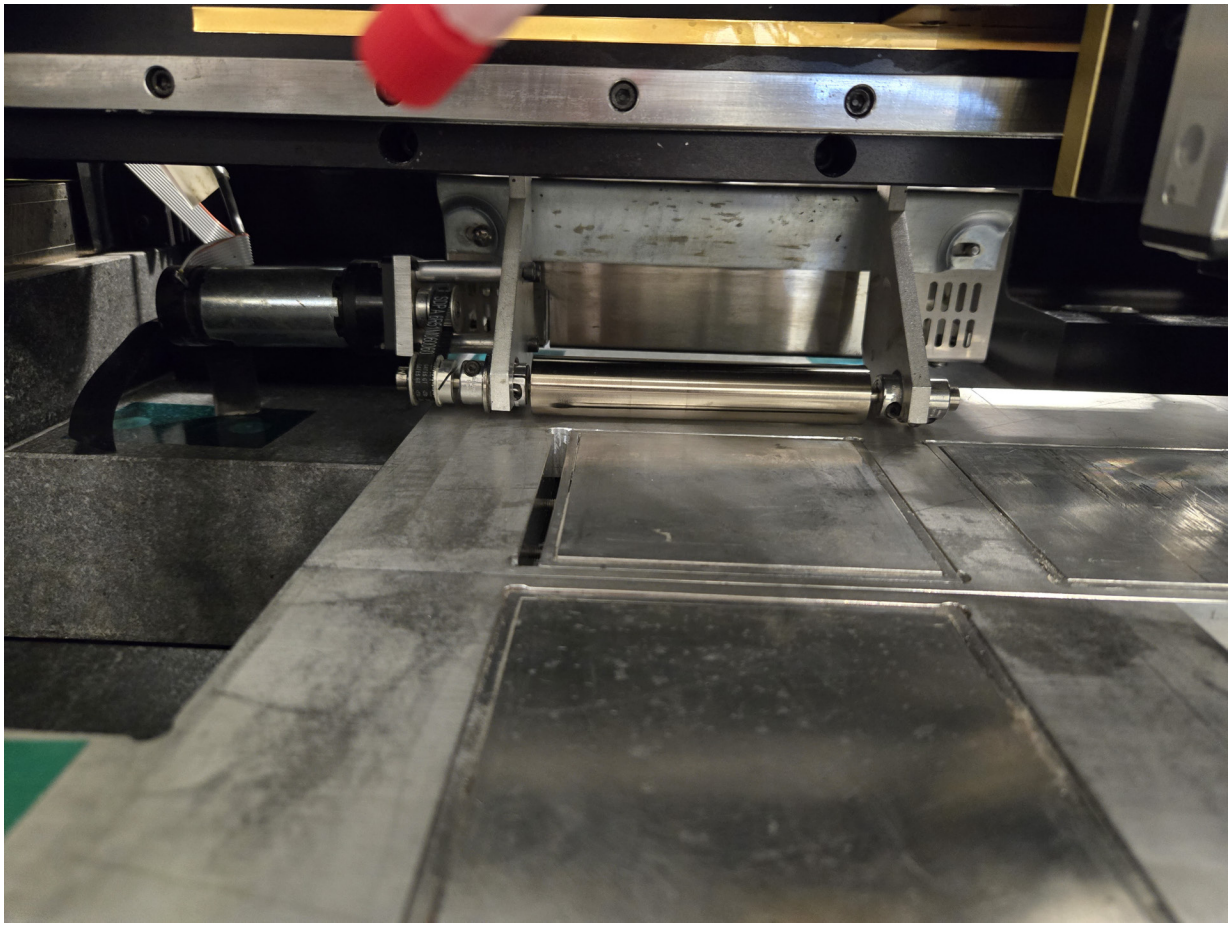


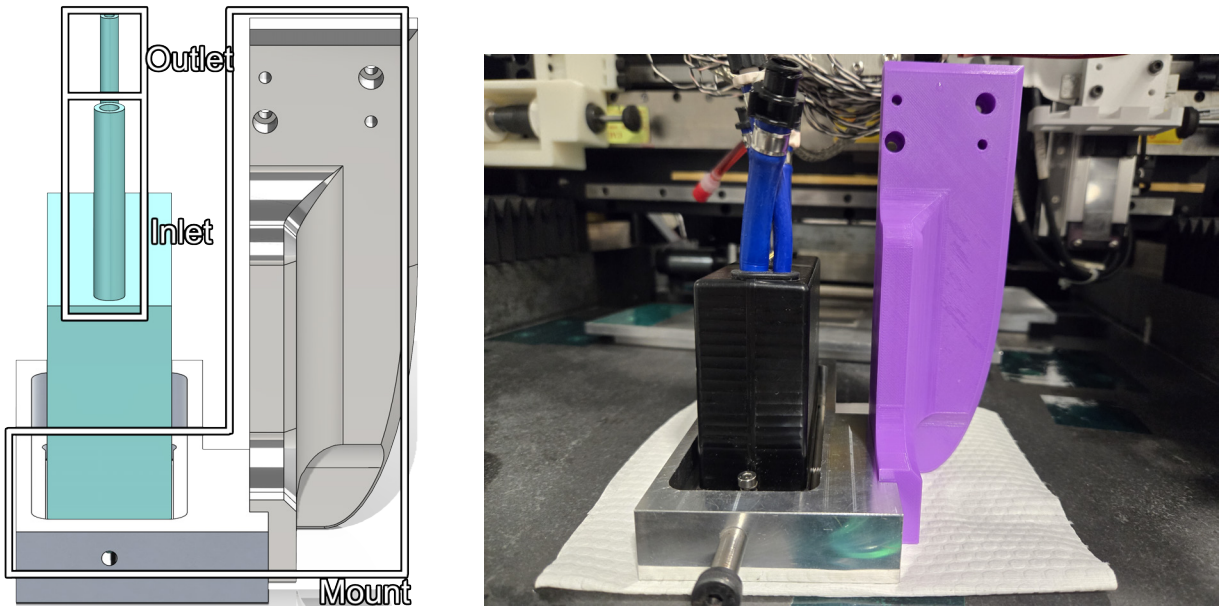
Figure 3.7: Photo of roller, feed and build beds, and heater.

The powder beds have a area of about 9.5 cm by 9.5 cm, with the printhead covering a significant fraction of that in a single pass. The powder beds are driven by stepper motors with lead screws (APPS23 stepper linear actuator, ElectroCraft), with a linear precision of 0.25 mils (thousandths of an inch), or 6.35 µm (with typical layer thicknesses in binder jetting on the order of tens of µm). The feed beds can be aligned with the build bed with a stepper motor driven carriage that can be moved during printing operation. The stepper motors use Parker Automation E-DC drivers that provide the step/direction input in an open-loop configuration (i.e. with no sensor feedback). The powder beds are run at low speeds to avoid disturbing the powder surface and the noise and vibration that occurs during stepper motor resonance, although the short layer thicknesses prevent it from slowing the printing procedure down significantly.

The roller uses a DC motor with a 10-to-1 reduction and encoder for speed control. The motor shaft is attached to the roller via a timing belt, and is capable of up to 500 RPM after reduction in both clockwise and counter-clockwise directions. The roller motor is connected to a servoamplifier (4-Q-DC, Maxon) for power, as well as speed and direction control. The position of the roller above the build bed is adjusted by shifting the positions of the bolts and mounting brackets - since it is manually levelled, the roller is not perfectly level, but since the deviations are minor, it does not have a major effect on the spreading of the powder.

3.2.3 Printhead and Binder Circulator

The printhead jets binder onto the powder inside the build bed, layer-by-layer, gluing the powder into defined shapes to build up a part or a set of parts within a layer. The printhead is attached to a binder reservoir and circulation system (Labjet LFR, Megnajet) that maintains internal pressure for optimum droplet release and continually cycles fluid through the printhead to prevent drying (and also to prevent settling, in the case of non-solution inks). Additional hardware produced by Meteor Inkjet (specifically a PCC, Print Control Card and HDC, Head Driver Card) is used to connect the printhead to the computer for control of both the binder circulator and the printhead. A combination of Meteor Inkjet's SDK and custom software is used to connect to the printhead and prepare images for printing.



(a) CAD of printhead and mount, showing fluid inlet and outlet tubes, as well as the mounting points to the printhead stages shown in Figure 3.4.

(b) Photo of printhead and mount.

Figure 3.8: Printhead and mount images

The printhead is a piezoelectric Fujifilm Starfire SG1024/MA, which comes in one-channel and two-channel models, capable of 400 DPI and 200 DPI, respectively. The model used during experimentation here has a nominal drop size of 30 pL, with other models covering a range from 12 pL to 200 pL. The printhead contains 1024 encoder-fired nozzles allowing the binder to be jetted at the correct locations. It covers a height of 2.56 inches, or 6.5 cm, which covers the majority of the build bed. A combination of vendor and custom software is used to convert images into printhead data. During printing, the printhead passes over the smoothed powder layer, depositing binder in the designated pattern, potentially multiple times to reach the required binder saturation levels. The required number of passes is dependent on the layer thickness, as well as the binder and powder being used - for the experiments described here, it was determined empirically.

The printhead waveform determines the degree of flexing of the nozzles, which physically deform to push the fluid out of the nozzle opening. The waveform is calibrated depending

on the printhead and fluid properties. In general, the fluid or binder to be jetted must be within a certain viscosity and surface tension range, with the vendor recommendations being non-volatile solvents at between 10 to 12 cPs and 32 to 42 dynes/cm at the targeted jetting temperature. The primary droplet characteristics of interest are velocity (higher is better), and shape quality (round and non-fragmented is better), though depending on the binder improving one may sacrifice the other. Lastly, certain binders are more or less tolerant of changes to the printhead and pressure parameters, and may be restricted to a maximum jetting frequency, with the vendor indicating that high viscosity inks are less sensitive and capable of higher-frequency jetting.

More generally, rheology-based binder optimization has been examined previously, and guidelines on fluid selection have been suggested based on Reynolds, Weber, and Ohnesorge numbers, relating them to droplet formation and the presence of satellite droplets [5, 35]. Additionally, in the case of inks containing solid particles, the particle size distribution, degree of particle loading, and the use of ultrasonic treatment to break up agglomerates have practical considerations, since particle clumping can clog printhead nozzles [21].

In our case, the maximum jetting frequency is most likely irrelevant because the printhead jets according to the encoder signal, and the speed of printing is much lower than any typical threshold for performance degradation.

The binder circulator is a Megnajet Labjet LFR, which attaches to the inlet and outlet nozzles of the printhead. The binder circulator provides a small external reservoir and its pumps maintain the fluid pressure at the correct level: too high and fluid will drip down from the printhead's nozzles, too low and fluid will not enter the printhead's nozzles at all, preventing printing. The inlet and outlet pressures of the binder circulator can be changed, which simultaneously affect the meniscus pressure at the printhead nozzles as well as the fluid flowrate - this must be calibrated on a per-fluid basis.

A high-speed camera and strobe light is attached to a Labjet LFR circulator outside of the custom binder jetting machine. This setup ("Dropwatcher") allows high-speed observation of individual droplets jetted by printheads and measuring the effects of changing circulation and printhead parameters (such as the pressures, or voltage waveform sent to the printhead), which may be transferred to the custom system. The close-up view of the printhead plate allows for examining phenomena like droplet velocity, droplet detachment from the nozzles, tail formation, droplet fragmentation, and droplet-on-droplet impact (multiple droplets jetted in quick succession at different velocities may collide with one another to form a larger droplet). Through this, printing parameters may be empirically optimized for each fluid.

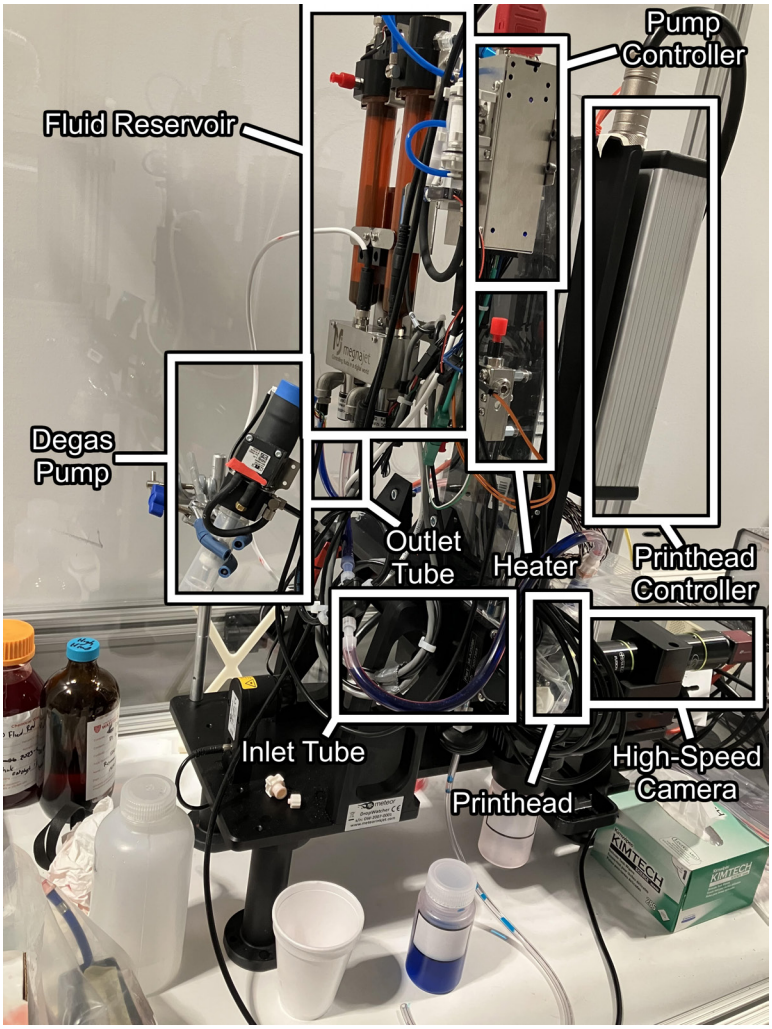
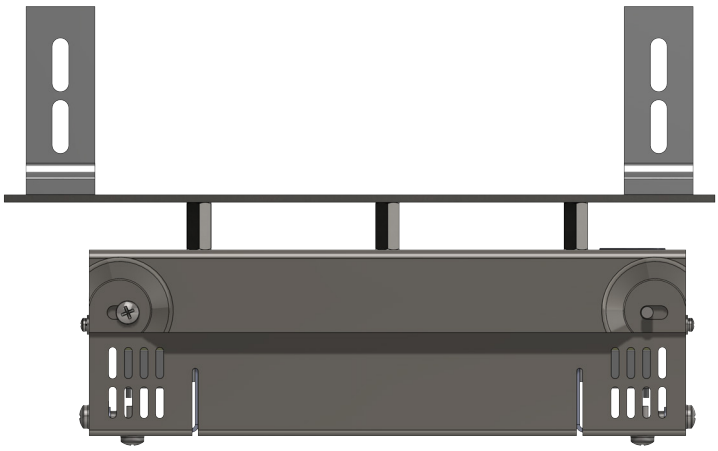


Figure 3.9: Photo of Dropwatcher setup

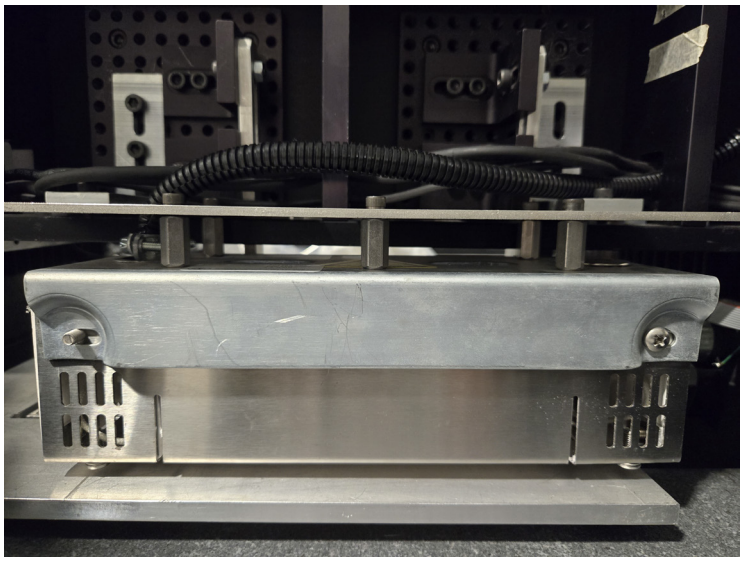
3.2.4 Infrared Heater

The infrared heater (103390-001, Research Inc.) contains a high-power infrared tube bulb and ceramic reflector that directs the radiant energy downwards toward the powder bed. It is used to control the evaporation and drying of the binder and the temperature of the powder bed. It has a maximum power output of 500 Watts, and covers the entirety of the build bed, with some overlap over both edges.

The heater output is controlled with a 4-20 mA control input. The relationship between the control input and actual power draw is non-linear and was measured with an inline power meter tested at multiple points to determine the input power (which is used in the results chapter to relate heater power to the observed temperature).



(a) CAD of infrared heater



(b) Photo of infrared heater

Figure 3.10: Infrared heater images

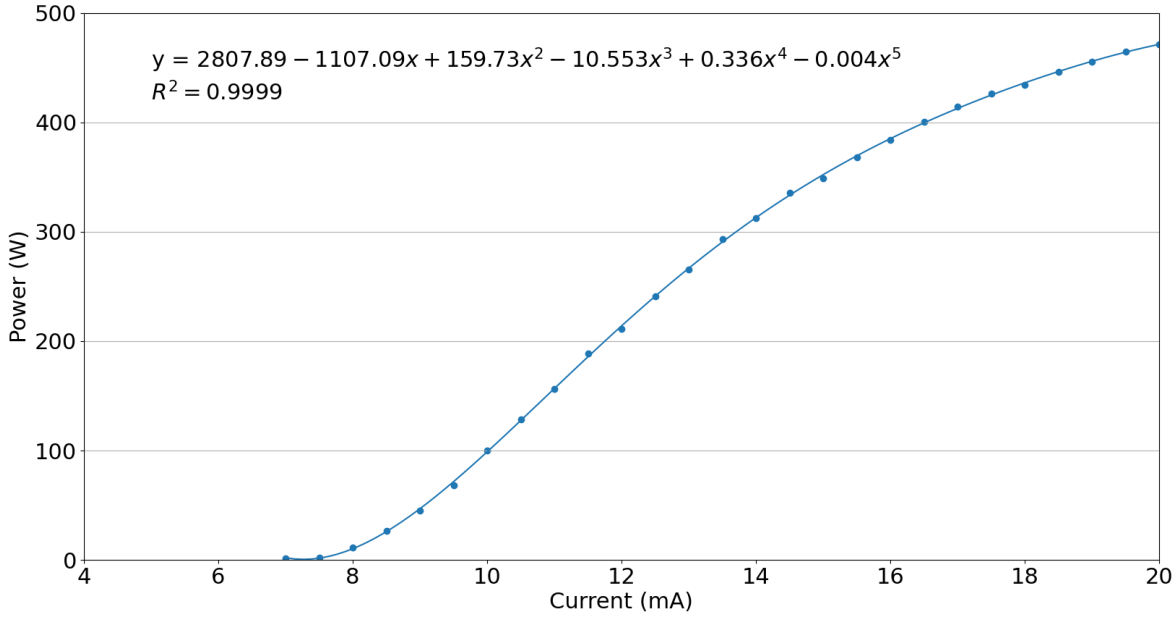


Figure 3.11: Heater Power Draw (W) vs. Input Current Signal (mA)

3.3 Software and Motion Control

The implementation of the software control architecture represented a significant portion of the thesis efforts, requiring full implementation to accomplish the required steps for printing objects. The software control of the system uses an open-source CNC software, LinuxCNC, to provide low-level hardware drivers, a software framework for motion control, G-code interpreter, and a graphical user interface. This framework is used to develop the control schema and integration of peripherals (printhead, roller, heater) that are not used in typical CNC machines. This software is run on a low-latency, realtime Linux kernel.

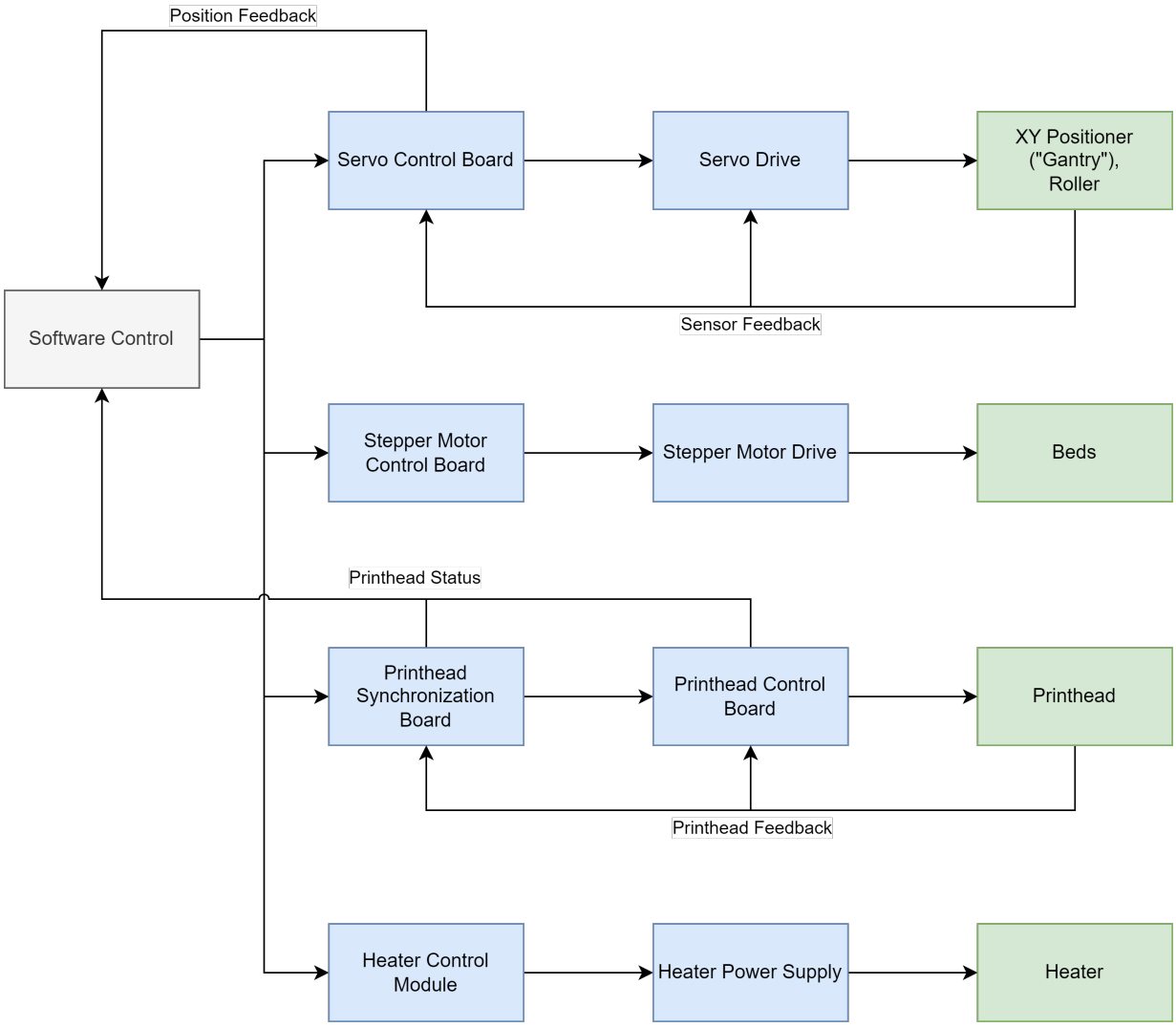


Figure 3.12: Diagram of major hardware components. Commands flow from software control into the major modules, with feedback from sensors sent back for electronic closed-loop control.

This framework allows for programming custom G-code commands and the execution of G-code files with images to define the printing pattern of each layer.

The motion control boards (the hardware that provides the input signals to the motor drives and receives feedback from the sensors) are Mesa Electronics boards; one 7I96 and one 7I77. LinuxCNC includes software drivers for connecting a PC to these boards. A

hardware abstraction layer (HAL) is used to program the relationship between the software and hardware, which provides signal processing and PID.

3.4 User Interface and Workflow

The default user interface used by LinuxCNC is called Axis (or Axis GUI). This GUI provides visualisation of the current state of the machine, fine-grained control of the moving components, and loading of G-code files.

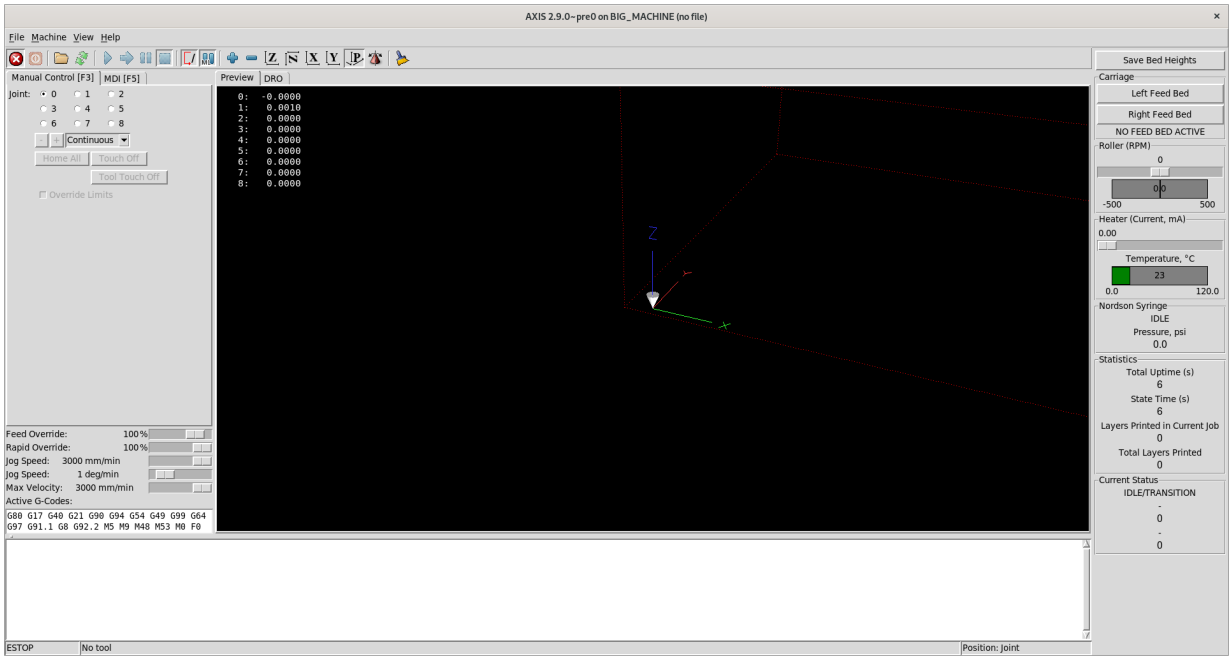


Figure 3.13: Axis GUI, a graphical front-end for LinuxCNC that provides a default implementation for machine control, with custom user interface elements implemented for the binder jetting machine shown on the right.

The typical workflow for a user is to power on the machine and conduct the setup steps needed to connect to the printhead, then transfer the printing data as a sequence of images to the computer and load a G-code file that carries out the printing procedure. For printing parts without recording sensor measurements, a common G-code file can be used due to there being only relatively minor differences between prints, shown in Appendix B.

For experimental printing, including the collection of sensor data, a modified G-code file is used to modify the steps taken, also in Appendix B.

The current workflow for converting a 3D model (STL file) into a set of images that can be used by the custom printer is to use a 3D printer slicer, PrusaSlicer [29], with a modified SLA profile (changing the display height and width to 63.5 mm and pixels to 1024) to output images of the correct resolution and DPI. The slicer can be set with the desired layer height, which will produce images at the corresponding offsets. Those images can be exported from the slicer as a zip archive, where they can then be further processed to invert the black and white pixels and narrow the bit depth from 8 bit monochrome images to 1 bit black and white bitmaps. These images are used in tandem with a G-code file for printing.

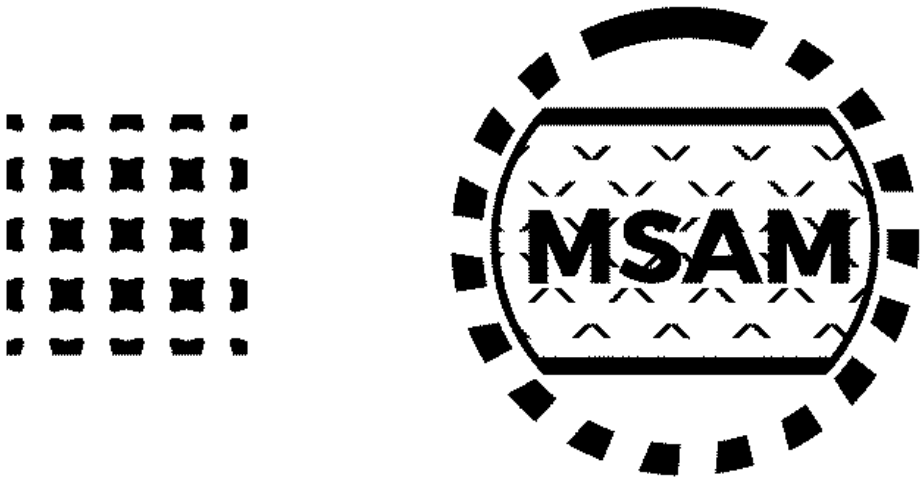


Figure 3.14: Example sliced image

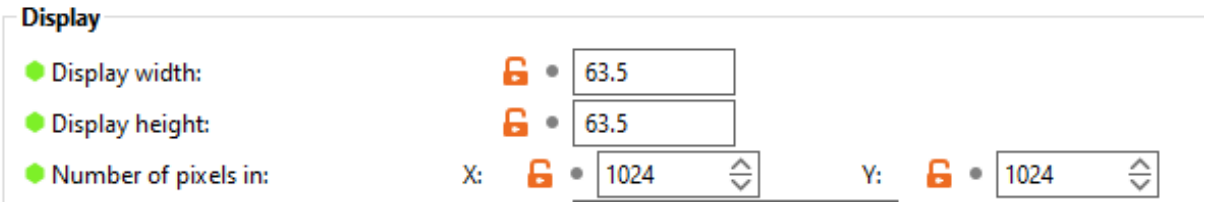


Figure 3.15: PrusaSlicer settings, showing main modification for Starfire SG1024 printhead, 2.5 inch/63.5 mm print width with 1024 nozzles.

3.5 Printing Capabilities

The binder jetting system has currently only been tested with gas-atomized SS316L powder designed for use in laser powder bed fusion processes, with a powder size distribution of 15 to 45 µm. This powder's high sphericity and size distribution gives it good spreading characteristics that may or may not be replicable with large powder sizes or water-atomized powders, which are less spherical. The only binder tested is ExOne's AquaFuse aqueous binder (BA005), which is selected due to its availability, because of its use in other machinery in the lab.

Printing has been carried out at layer thicknesses of 50 µm and 100 µm, with reasonable results from both. Different parts were tested to determine the minimum feature sizes currently achievable, which appears to be on the order of about 1 mm. The current printing speed is about 3 minutes per 100 µm, or 300 minutes to print a 1 cm tall part, with plans in place to improve the printing speed in the future.



Figure 3.16: Example of a printed lattice (IWP Solid), 100 µm layer thickness, 1 cm by 1 cm sides.

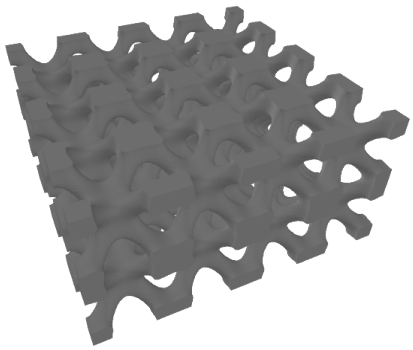


Figure 3.17: IWP lattice solid model, generated by MSLattice [2].

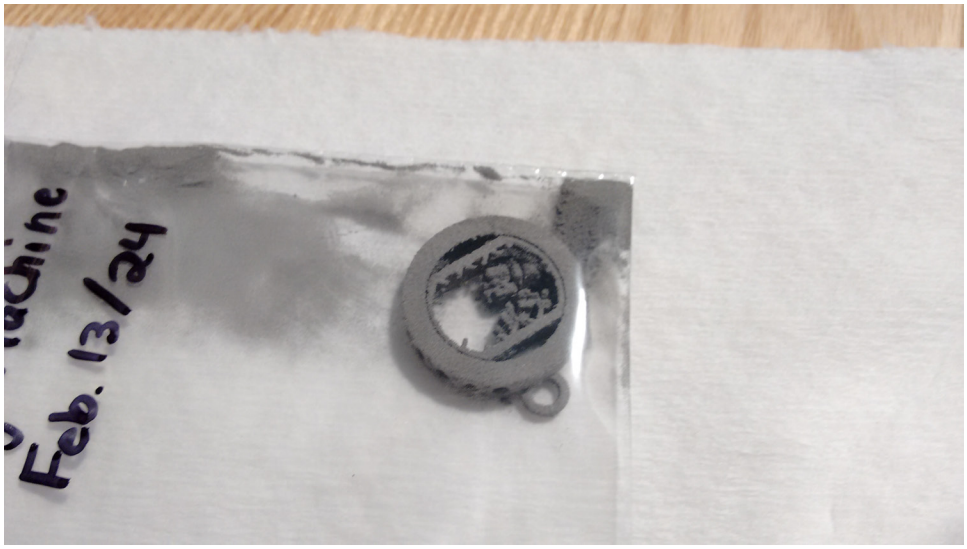


Figure 3.18: Example of a keychain print, 100 µm layer thickness, showing an example of a print failure due to feature size being too small.



Figure 3.19: Keychain solid model, designed by Sagar Patel and Jerry Ratthapakdee

Chapter 4

Experimental Methodologies

The use of a heating lamp has been found to be extremely beneficial in achieving high-fidelity print geometries by tuning the powder substrate temperature (via tuning the intensity of the heating lamp) in tandem with tuning the amount of binder jetted onto the powder in each layer (via tuning the binder saturation) [4]. After jetting the binder, the heating lamp can be used to remove moisture content from the powder substrate to prevent excessive lateral and vertical liquid imbibition, which could reduce geometric fidelity of the part [4]. Furthermore, the heat is also an efficient means to initiate the binding process, where the polymer starts to cure and glue powder particles together in each layer [26]. There is a gap in the pertinent binder jetting additive manufacturing literature focusing on developing methodologies to document and understand the effect of the heating lamp on the powder and binder substrate.

In this present work, the experiment being carried out is the measurement and recording of temperatures within the powder bed both with and without binder. The sensors and data schema described here are used to record the temperatures and other information, like the state of the machine (speed, position) and time. A combination of a thermocouple array and a thermal camera are used to infer temperature data.

4.1 Temperature Measurement Setup

4.1.1 Thermocouples and the Thermocouple Array

The sub-surface temperature is measured using an array of nine type-K bead (exposed junction) thermocouples (CA-733, Wewooday), which are affordable and have good response

time due to their low thermal mass. The thermocouples are connected to corresponding MAX6675 amplifiers to scale their voltage to measurable levels and a microcontroller (MEGA 2560, Arduino) to send the data to a PC to be recorded. The thermocouple setup has a temperature resolution of 0.25°C, a polling frequency of 4 Hz, and an accuracy of approximately ± 2°C. The Arduino code accesses the temperature data and responds to serial interface queries from the PC with the thermocouple temperatures, connected as shown in Figure 4.1.

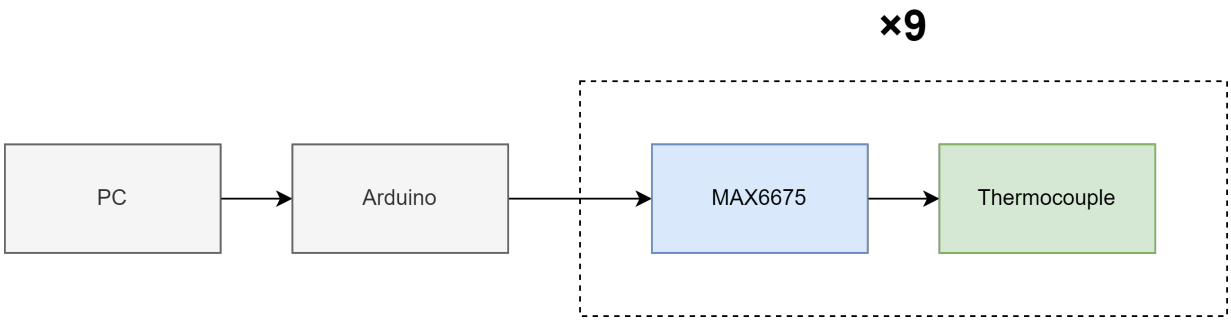


Figure 4.1: Thermocouple hardware setup

A 3D printed inset plate is used to maintain each of the thermocouples' positions and depths. The plate is glued to the build bed platform, which is moved up and down to control the thermocouple depth and distance from the surface of the powder. The thermocouple wires are fed into the holes on the side and pulled through the holes at the top, and clipped into place with plastic clips that fix their locations and prevent them from shifting from their positions in the array plate in Figures 4.2 and 4.3. The thermocouples form a 60 mm square, with 30 mm between each one.

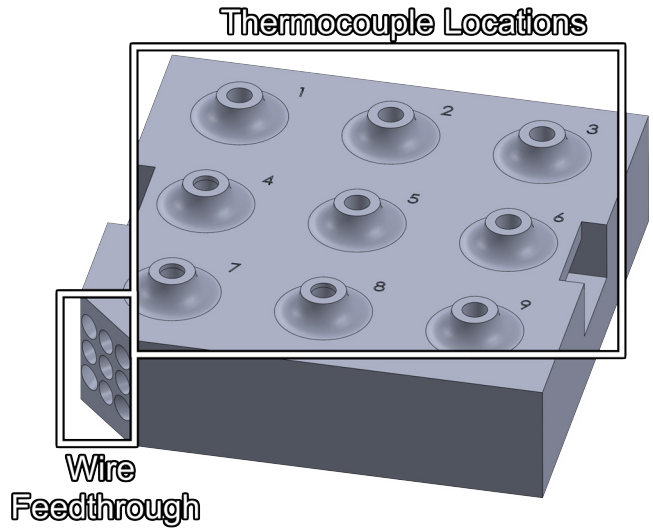


Figure 4.2: CAD of thermocouple array plate. The thermocouple wires are fed through holes in the side and the junctions are pulled out through holes in the top.

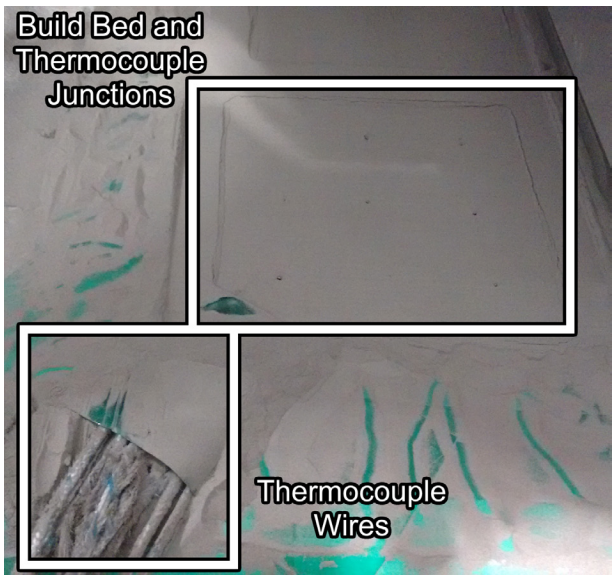
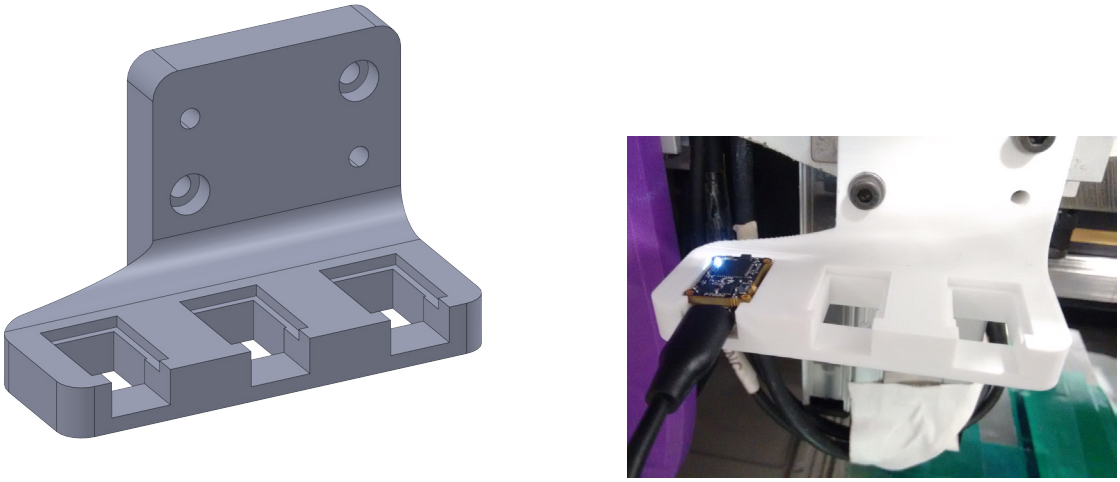


Figure 4.3: Photo of thermocouples buried under SS316L powder, with the wires leading into the feedthrough point. The thermocouple junctions are barely visible above the surface of the powder.

4.1.2 Thermal Camera

The surface temperature is measured using a LWIR camera module (Lepton 3.5, FLIR), which has a resolution of 160 by 120 pixels, an accuracy of ± 5°C, and a maximum frame rate of 8.7 FPS. It is connected to a PC via a breakout board (PureThermal Mini, GroupGets), which the camera module slots into, providing connectivity through USB. The breakout board is placed in a 3D printed mount that is attached to one of the vertical stages, as in Figure 4.4, positioned such that the camera has a view of the entire build bed. The libraries used for interfacing with the thermal camera module are flirpy [32], for parsing and accessing the radiometric data, and OpenCV, for providing connectivity to the breakout board via its UVC software interface.



(a) CAD of thermal camera mount

(b) Photo of thermal camera mount

Figure 4.4: Thermal camera mount

4.1.3 Material System

The powder material system used for this experiment is gas-atomized 316L stainless steel with a 15 to 45 µm powder size distribution. The binder used is a proprietary aqueous binder (ExOne AquaFuse, BA005), which is primarily a mix of water and ethylene glycol, along with some other proprietary components such as anti-foaming agents, surfactants, and antifungal agents.

4.2 Data Packages

The data collected during experimentation comes from the thermocouple array and the thermal camera. The thermocouple array collects temperature data for each layer, beginning data collection when the heater is turned on, allowing the heater to pass over the build bed, and continuing data collection for some time after the heater is turned off to capture the transient effects of cooling down of the build bed.

The thermal camera is mounted on one of the vertical stages, which are in turn mounted on the Y-stage, along with the printhead, roller, and heating lamp. Due to the placement of the camera relative to the build bed, the camera cannot continuously capture the temperature of the build bed surface, as the camera cannot be over the build bed at the same time as the heater or printhead are active. Instead, the camera is moved into place above the build bed immediately after significant steps (heating, printing) to capture key points during the layer. Latency time between heat lamp exposure and camera data acquisition are documented.

The thermocouple data contains both the time of recording as well as the temperatures of all of the thermocouples, with the data format shown in Table 4.1.

Table 4.1: Thermocouple Data Format Example

Time since Start	Thermocouple 1	Thermocouple 2	Thermocouple 3	...
...				
1530.43	47.75	48.00	48.50	
1530.67	48.00	47.50	48.00	
1530.91	48.50	48.50	49.00	
...				

The thermal camera collects snapshots of after specific steps mentioned previously, storing the radiometric data in a NumPy file containing the 160 by 120 pixel array of temperatures reported in Celsius. The only modification performed on the sensor data is converting the original data units from centiKelvins to Celsius.

4.3 Data Collection Procedure

4.3.1 Procedure Overview

Temperature monitoring and associated data collection is carried out both with binder (also referred to as "wet" or "printed" experiments) and without binder (also referred to as "dry" experiments) being jetted onto the substrate, as it was hypothesized that the binder evaporation may have an effect on the temperature readings. The general order of steps in both dry and printed experiments is shown in Figure 4.5 and Figure 4.6 respectively, with steps at the top occurring first.

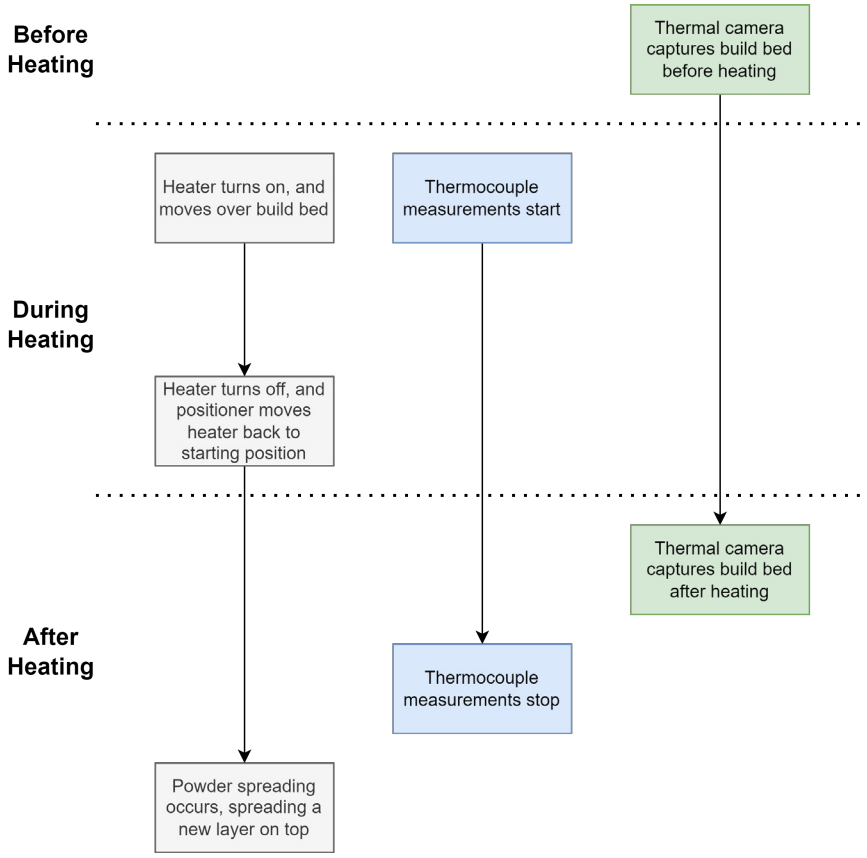


Figure 4.5: Sensor measurements and machine sequencing during dry experiments. This figure indicates the sequence of actions taken by the machine, thermocouple logger, and thermal camera, in order from top to bottom.

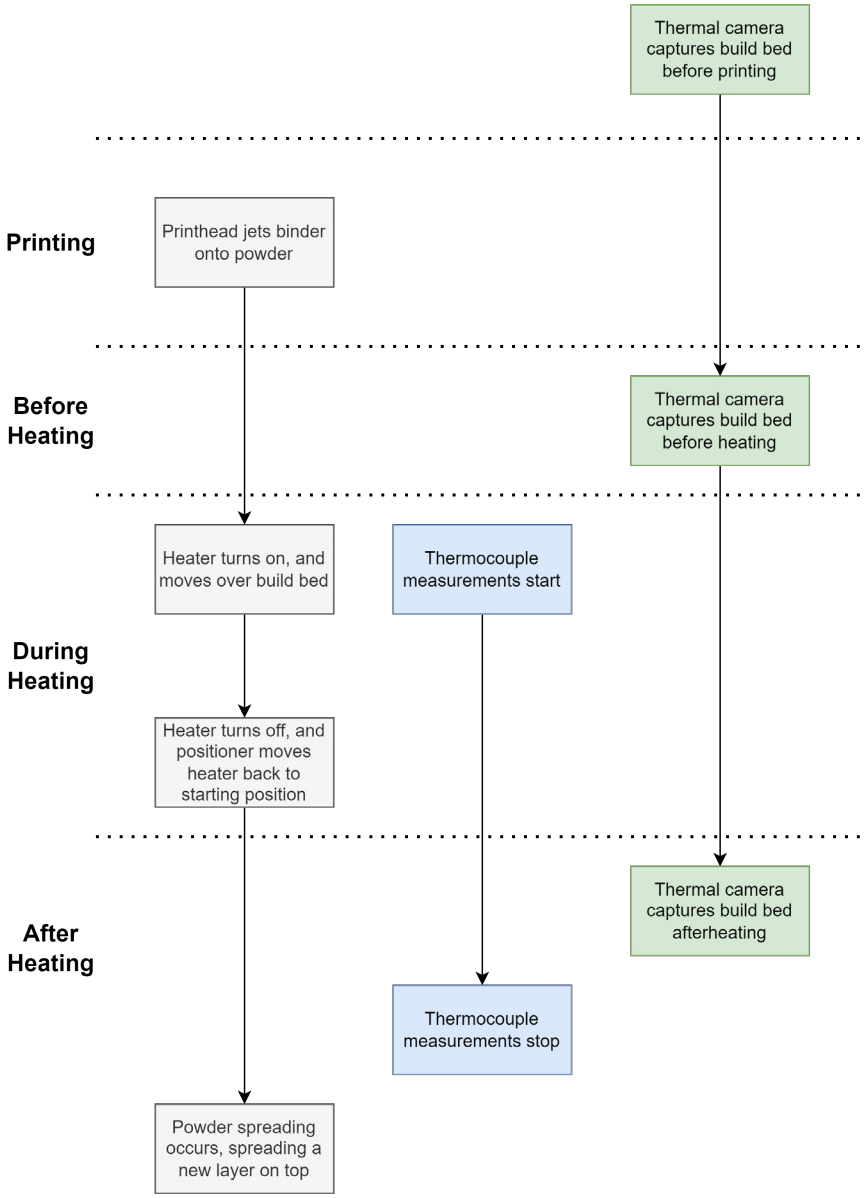


Figure 4.6: Sensor measurements and machine sequencing during printed experiments. Compared to the dry experiments, this has a printing step and an additional thermal camera capture.

4.3.2 Detailed Steps

The mounted thermocouples are placed in the build bed insert and lowered to be level with the bottom of the roller, with an initial check to ensure that all thermocouples are approximately level with each other. The powder will then be loaded into the build bed around the thermocouples and levelled flat with the roller at the height of the thermocouples. The initial temperatures will be close to room temperature, or 20°C to 25°C.

The typical operation for the dry powder experiments involves the sequential layering of a new powder layer, followed by applying heat using the heat lamp. The heater power and trajectory/velocity will be varied, with the heater standoff distance and deflector remaining fixed. The temperatures of the thermocouple array will be logged over time as heat is applied, at different layer depths, as powder is added on top of the thermocouples, layer-by-layer. Powder will be overlaid on top of the build bed to the target layer thickness depth for the experiment using the roller and feed bed.

A typical order of operations for conducting a printed experiment is as follows. It is important to note that dry experiments without binder are conducted similarly, but without steps 1 and 2.

1. Move thermal camera above the powder bed and capture image (prior to printing).
2. Move printhead over build bed and jet binder.
3. Move thermal camera above powder bed and capture image (after printing, before heating).
4. Turn on heater, set to target power, and move at fixed velocity over build bed. Simultaneously begin taking measurements from thermocouples.
5. Turn off heater.
6. Move thermal camera over build bed and capture image (after heating).
7. After some time has passed (experiment-dependent), stop taking measurements from thermocouples.
8. Spread layer of powder over build bed.
9. Repeat from step 1 for target number of layers (30).

Both the roller and heater move in the feed bed-to-build bed direction as seen in Figure 4.7, and so the thermocouples in positions 1 through 3 are exposed to heat first.

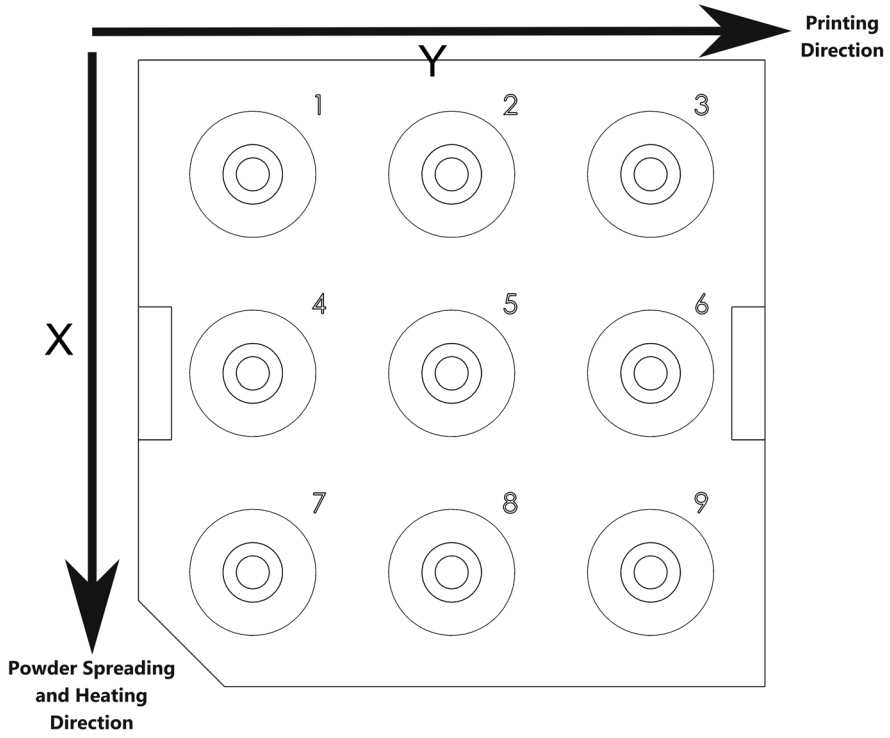


Figure 4.7: Thermocouple indices and directions, showing the locations of the nine thermocouples with numbered callouts and relative directions in which powder spreading, heating, and printing occur.

The heater starts at the rear, and the heater moves from back to front over the build bed. During the heating step for each layer, the heater will be turned on, moved to the edge of the build bed, and then cross the build bed at a fixed velocity. After the heater has covered the length of the build bed, the heater will be turned off and moved to the starting position. Measurements for that layer will continue for some time to capture the cooling down temperatures. Subsequently, a new 50 µm layer of powder will be applied, and then the steps will be repeated again. This will continue for a total of 30 layers; the number of layers was selected based on the assumption that the temperature at the thermocouple depth will reach a steady state, as powder is known to have poor thermal conductivity. Due to the position of the heater relative to the build bed, the forward region of the build

bed is not fully cleared by the heater and thermocouples 7 through 9 receive less heat when the heater is moved at constant velocity.

This experiment was performed both with and without binder (wet and dry powder). The wetted powder pattern will be nine circles, 1 cm in diameter, with each circle printed above the each of the nine thermocouples respectively, as seen in Figure 4.8.

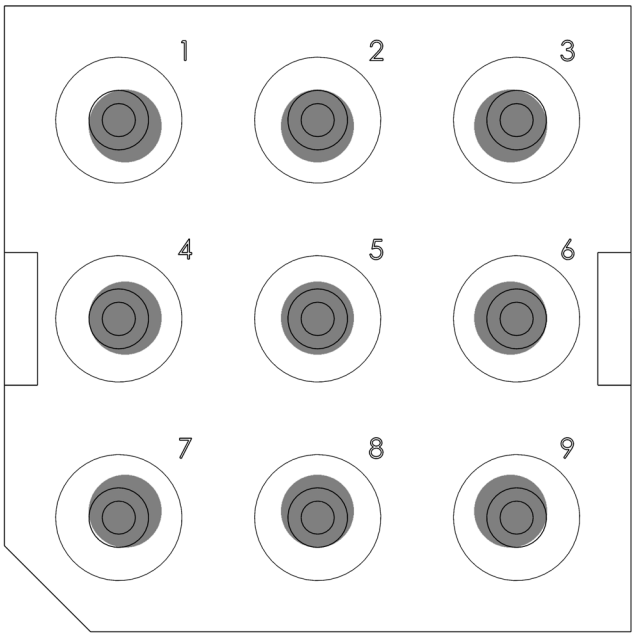


Figure 4.8: Locations of Printed Circles

The thermocouple plate is immobilized to the base of the build bed with hot glue. The thermocouple beads are pulled through the top holes of the inset plate to be level with the powder surface and each other.

The combinations of heater power and heater velocity are shown in Figure 4.9 and Figure 4.10 below for both the dry and printed experiments respectively. The heater power input is given as both a control current that it uses as an input signal (4-20 mA), and the corresponding estimate of its power based on power measurements from the heater curve in Figure 3.11 (e.g. an input signal of 11.0 mA is estimated to draw 157 W of power). The parameter selection is exploratory based on domain expert estimates of "typical" binder

jetting temperatures using a heater for drying, which were anticipated to be between 30°C and 100 °C, as going above the boiling point of water (for commonly used aqueous binders) may cause warping or issues with curling and interlayer adhesion.

The dry experiments were conducted first, and the range of temperatures obtained were used to narrow down a range of heater parameters for the more time-consuming and error-prone printing experiments.

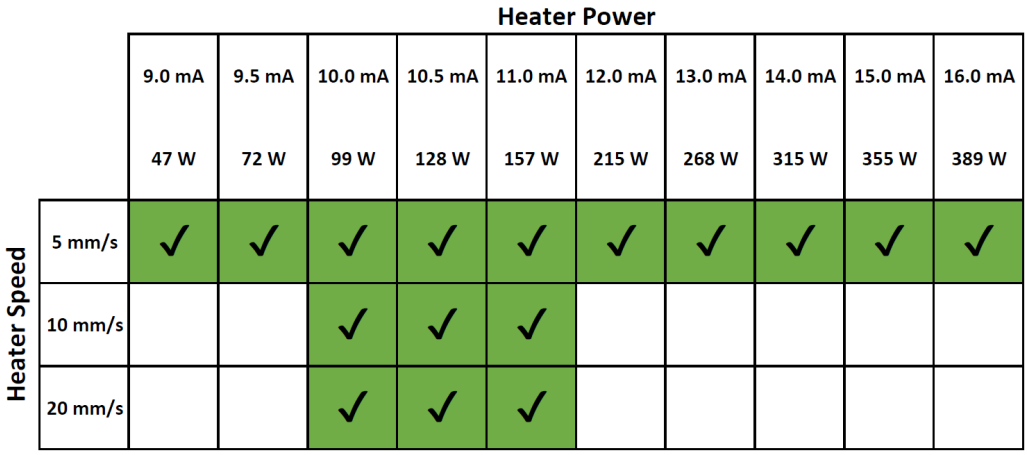


Figure 4.9: Experimental Parameter Coverage, Dry. Checkmarks indicate a combination of heater power and speed that was tested.

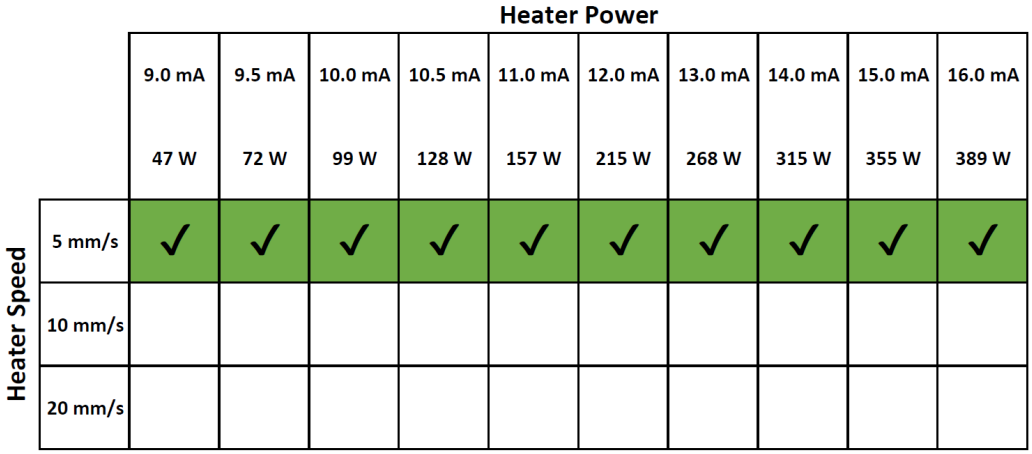


Figure 4.10: Experimental Parameter Coverage, Printed. Checkmarks indicate a combination of heater power and speed that was tested.

Chapter 5

Results - Measurements and Analysis

5.1 Measurement - Descriptions of Data Visualization

The visualization and analysis of temperature trends within the powder help to inform both machine-specific calibration as well as physical phenomena that are relevant to binder jetting more generally, as the temperature of both the surface and bulk powder influence the infiltration of the binder through the powder substrate [6, 8], the curing and drying of the binder [26], and the influence of evaporative cooling from water-based binders [6, 8]. Dressler et al. examined the long-term effects of heating on powder bed temperature over the course of half an hour of heating or more [12]; here, we examine temperature trends during shorter drying times that are more practical for per-layer binder curing.

The data used for the analysis is primarily thermocouple data, with some thermal camera data presented in the later sections. An example of thermocouple data for one set of heater parameters is shown in Figure 5.1 below. As described previously, the experiment occurs over thirty layers of powder - each peak in the full graph represents the peak recorded temperature for one layer, across all 9 thermocouple locations. A zoomed in-view of the temperature change over one layer is also shown in the example in Figure 5.1 below.

It can be seen that for each layer, the temperature rises while the heater is on, reaching a peak and then cooling down after the heater is turned off. There is a gap in between layers, which occurs during powder spreading when no temperature measurements occur, and appears on the graph as a completely straight line connecting the end of one layer's measurements to the beginning of the next layer's measurements. Additionally, the incomplete heater coverage of the build bed is also visible on the plot, as the set of three

thermocouples indexed as 7, 8, and 9 are not completely covered by the heater's path and thus have much cooler peak temperatures.

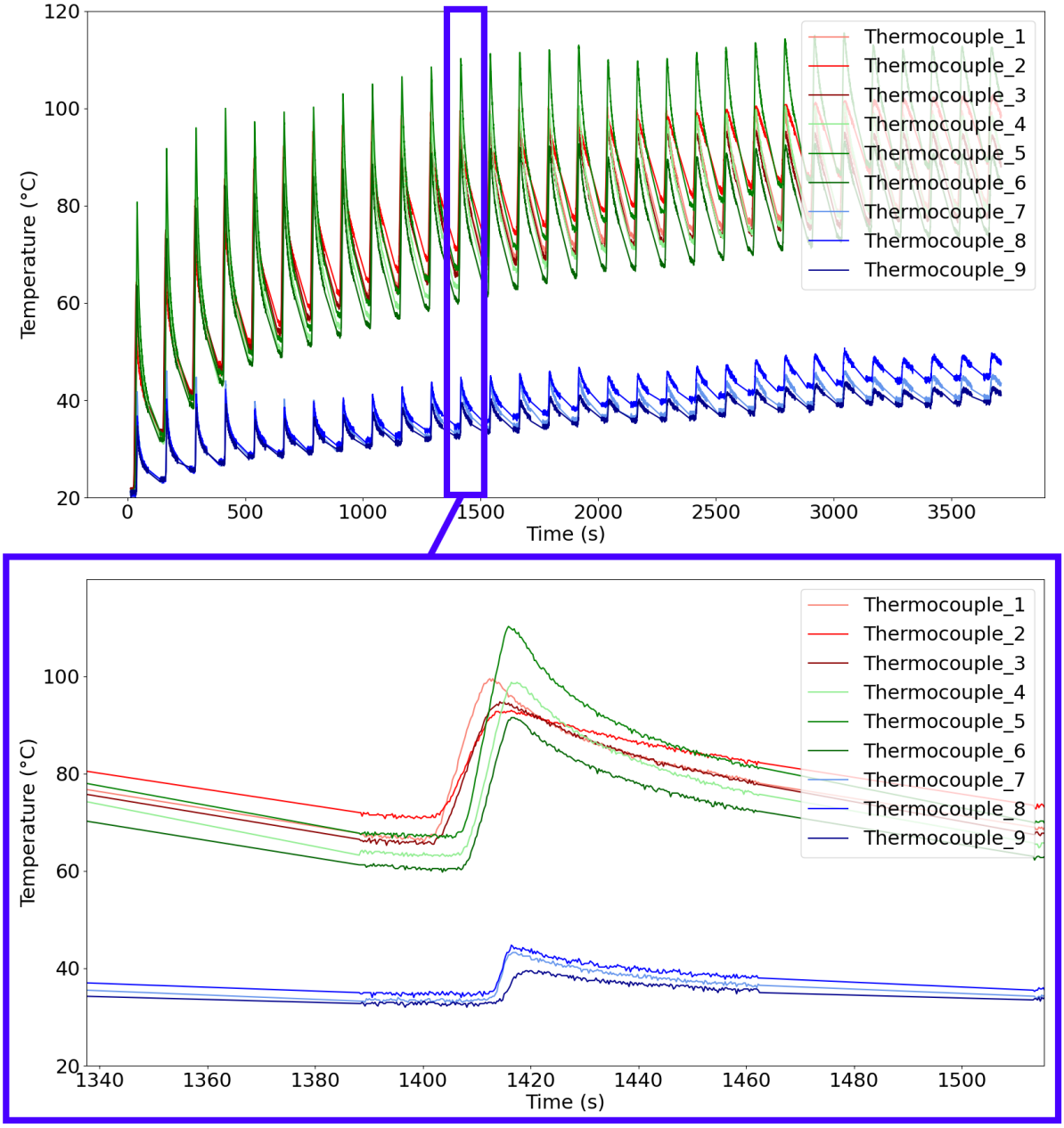


Figure 5.1: Example thermocouple data, showing temperature data over nine thermocouples taken at a heater power of 349 W and a heater speed of 5 mm/s. A zoomed-in view of the temperature trend across a single layer is shown below the full plot.

It is important to note that, since printing does not occur during the dry experiments, the cooling-down period (during which no heating occurs) after attaining the peak temperature is extended, such that in results where the dry and printed experiments are being compared, the per-layer time for both the dry and printed experiments are approximately the same. The cooling-down period contains measurements, which means that the measurement period after heating for dry experiments is longer than in the printed experiments, as shown in Figure 5.2 and Figure 5.3 respectively.

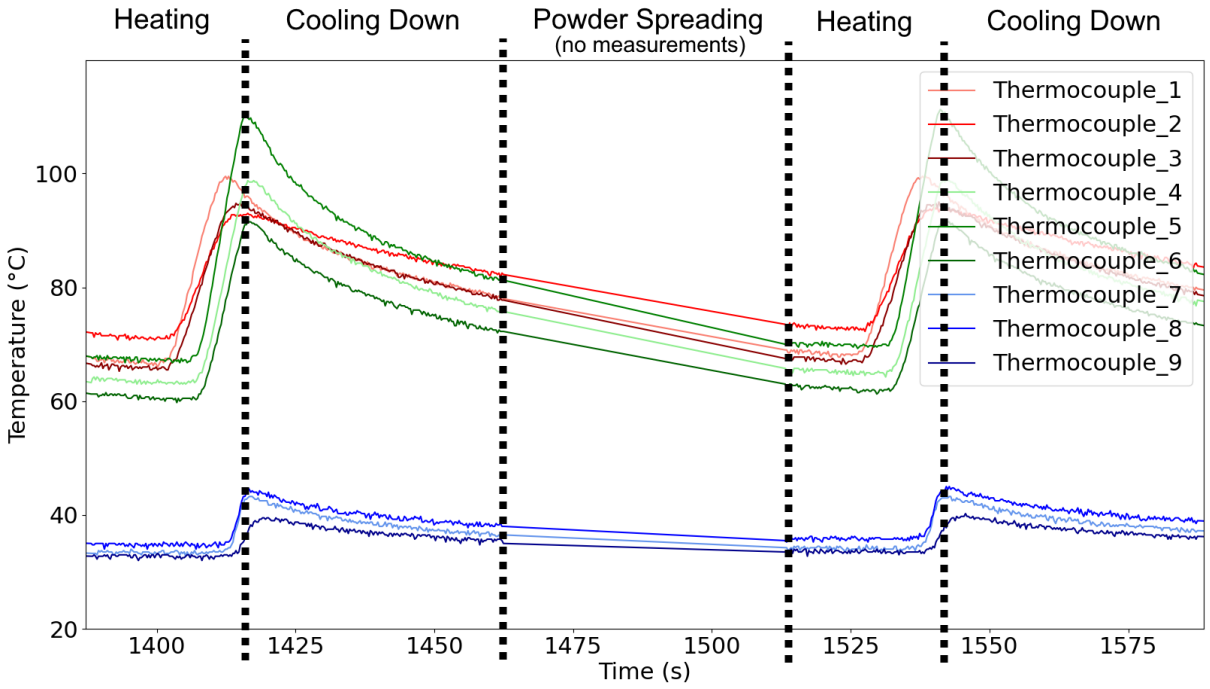


Figure 5.2: Procedure steps, dry experiments. Each layer consists of a heating step, a cooling down step, and a powder spreading step. No temperature measurements take place during the powder spreading step. Example taken with a heater power of 349 W and a heater speed of 5 mm/s.

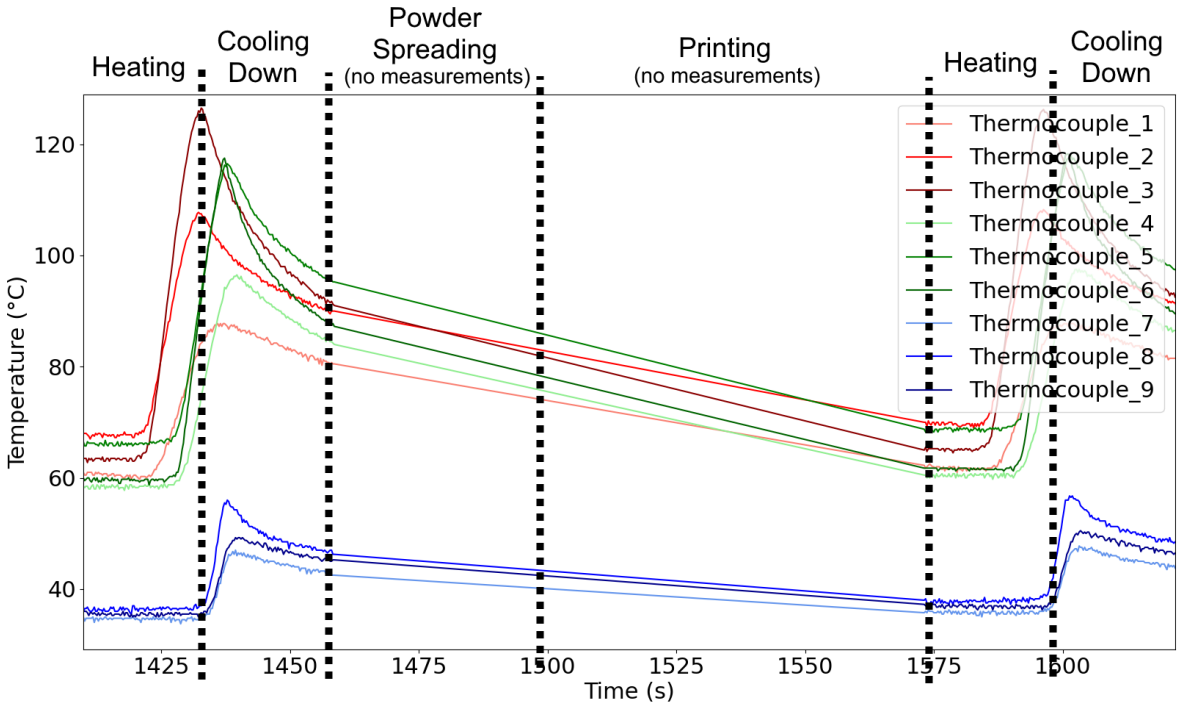


Figure 5.3: Procedure steps, printed experiments. Each layer consists of a heating step, a cooling down step, a powder spreading step, and a printing step. No temperature measurements take place during the powder spreading and printing steps. Example taken with a heater power of 349 W and a heater speed of 5 mm/s.

An instance of thermal camera data is shown in Figure 5.4 below as a colour map, selected from one of the printing experiments shortly after the heater pass was completed. Here, the bed is visible and the circular printed regions stand out from the rest of the dry powder. The bottom three printed circles are barely visible due to the incomplete heater coverage. In the dry experiments without binder, these circles do not appear, as seen in Figure 5.5.

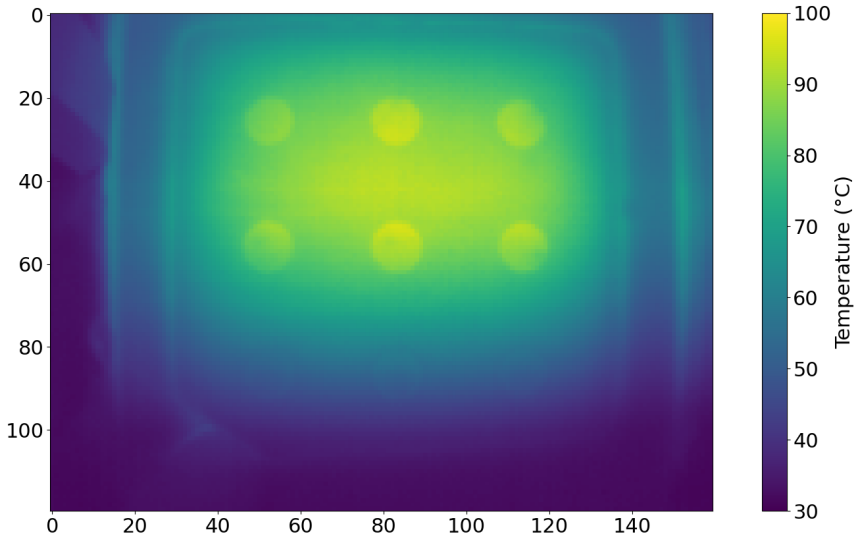


Figure 5.4: Example thermal camera image, printed. Example taken with a heater power of 349 W and a heater speed of 5 mm/s at layer 15.

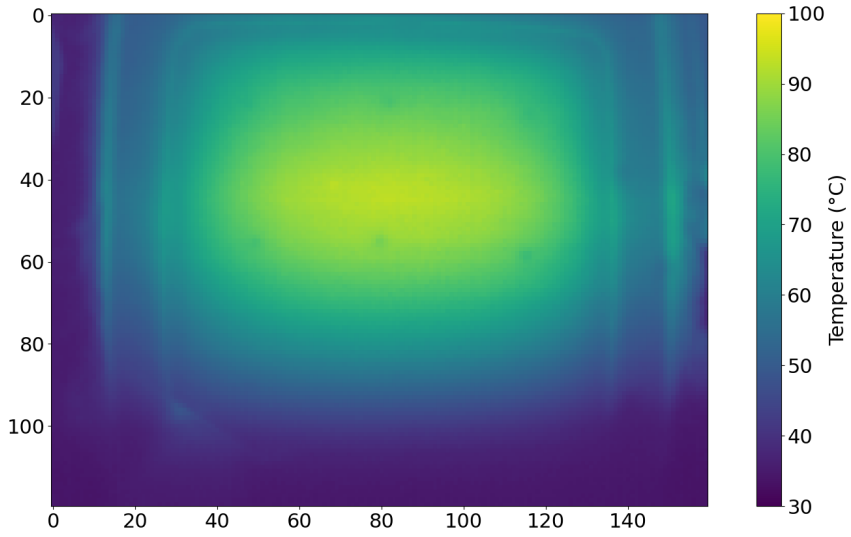


Figure 5.5: Example thermal camera image, dry powder. Example taken with a heater power of 349 W and a heater speed of 5 mm/s at layer 15.

5.2 Measurement - Physical Reasoning and Lead-in

The temperature changes observed at the surface and below the surface of the powder bed are a combination of incident, absorbed radiant heat, which increases the temperature, and conduction and emission out of the powder, which decreases the temperature. Given this, there are a few questions about the thermal behaviour of the heater-powder system:

1. Is the temperature rise due to absorbed radiation large compared to heat loss due to conduction and re-radiation? Is the heating rate strictly dependent on the heater power and velocity over the temperatures and timespans tested?
2. Is the cooling behaviour consistent? What is the impact of the starting temperature and depth on cooling rates?
3. Is there spatial variation parallel or perpendicular to the heater? Is there evidence to quantify heat loss to the walls of the build bed? How uniform is the bed temperature in general?
4. Does the binder affect the absorptivity of the surface? Does its thermal mass affect the heating rate or the peak temperatures obtained? At high temperatures, does evaporative cooling of the binder-solvent material affect the temperature compared to dry powder?
5. Can the thermal camera resolve the outline of printed parts at the surface of the build bed (as in, is the temperature difference large enough and the temperature gradient sharp enough to do so)? Can it resolve the outline of parts under a layer of powder? Can it detect defects of a particular size scale? Defects are defined as poor powder spreading inconsistencies (striations, cracking) or binder dispersing inconsistencies (misfiring nozzles, over-saturation).

Additionally, there are other phenomena which are out-of-scope for this research but will be briefly discussed in a later chapter.

1. How does depth impact the time between heat application and a rise in temperature?
2. Are conventional vision systems (i.e. normal cameras) better suited to viewing and detecting deviations during printing?
3. How does the degree of drying and curing (and by extension, the degree of heating) impact green part strength prior to sintering?

5.3 Analysis - Impact of Infrared Heater on Dry Powder Bed

To isolate some aspects of the heater impact on powder, we will begin with the temperature changes observed on 316L powder without any binder present.

5.3.1 Analysis - Effect of Heating Rate

The heating rate of the powder affects process optimisation and control - it is directly related to properties like peak temperature and evaporation rate, which affects green part properties like thermal warping/curling [26], imbibition of the binder into the powder [6], and any binder chemical reactions that may occur at high temperatures. The heating rate also influences how fast the substrate heats up to ensure appropriate evaporation of the binder to prevent over-saturation of previous layers [8], which can result in a so-called "elephant foot" defect, where liquid migrates to the bottom of the part creating significant green part distortion [26].



Figure 5.6: Example of binder bleeding and elephant's foot defect in ceramic cuboid samples due to insufficient drying. Adapted from [23].

The detected heating rate is defined here as the temperature rise between the start of a layer and its peak, divided by the time over which it occurs. Since the thermocouples

are in different locations, each one will experience a different heating rate for a given combination of heater power and speed. Additionally, as each experiment proceeds, and the thermocouples are located lower below the surface of the powder with every layer of powder added, the heating rate may decrease due to the poor thermal conductivity of the SS316L powder [34]. Therefore, there are three sub-analyses to conduct with respect to understanding the effects of heater parameters on powder heating rate.

1. The change in heating rate for a selected thermocouple as depth increases, to determine the significance of depth changes. This is an important analysis, as it can inform how many layers below the surface evaporation and polymer thermal reactions may occur.

2. The change in heating rate for a selected thermocouple as a function of the heater power and speed (at the same depth). If the radiant heating far outstrips the heat loss across the temperatures tested, then the overall heating rate will be only proportional to the heater power and inversely to the heater speed. This analysis is valuable in understanding the direct effects of heating parameters for a constant powder thickness to inform what can occur layer-by-layer.

3. The difference in heating rates between the same thermocouple row. Due to the heater's overlap over the edges of the build bed, the heating rate may be similar, but uneven heating and loss of heat to the walls may result in lower overall heating rate compared to the center. This analysis is valuable in understanding if there are regions in the powder bed where the effect of the heating lamp is non-uniform, as it may translate to non-uniform green part properties.

To convert both heater parameters (power and speed) to a single parameter for comparison purposes, we will define a measure called linear energy density, which is the power divided by the speed. This measure estimates the heat energy delivered by the heater per distance unit of the build bed traversed, and will be given in units of J/mm.

$$\text{Linear Energy Density } [J/mm] = \frac{\text{Heater Power } [J/s]}{\text{Heater Speed } [mm/s]} \tag{5.1}$$

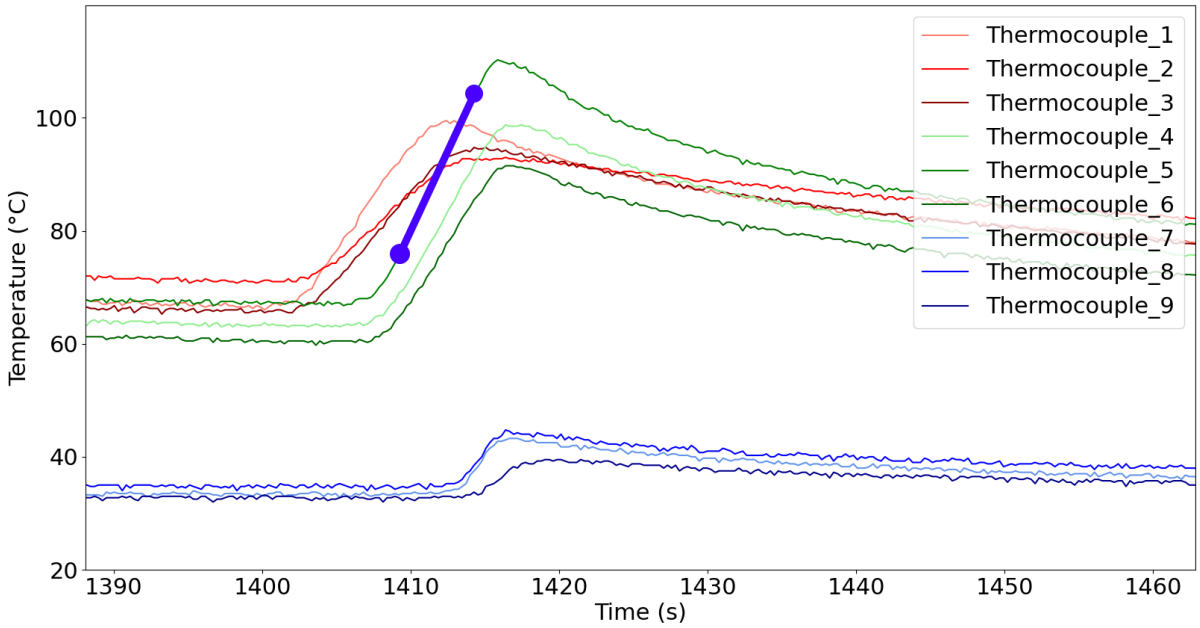


Figure 5.7: Linear approximation of heating rate

To develop an intuition on heating rate, we will first examine changes in heating rate within an experiment, to see how additional layers impact the speed at which the powder heats up. The thermocouple data is noisy and so we will define a heuristic to use to estimate the heating rate, under the assumption that the heating up section of the data may be approximated by a linear curve, as seen in Figure 5.7. Specifically, the heuristic is as follows:

1. Select a range of data spanning twenty data points (approximately five seconds).
2. Calculate the temperature difference between the two endpoints of the range.
3. The data range with the largest difference is used to approximate the heating rate, defined as the temperature delta over the time between the two endpoints of the range.

Generally, it is expected that the heating rate decreases with layer index, as the additional powder is insulating the thermocouples from the heater, and the bulk temperature of the powder bed is higher than when it started, increasing the rate of heat loss relative

to the heat input. In the limit, the heating rate would exponentially decay to zero due to the distance from the heater resulting in a steady state temperature.

The following set of figures will display the heating rate in the center of the build bed (thermocouple 5) as a function of layer index for different sets of heater parameters.

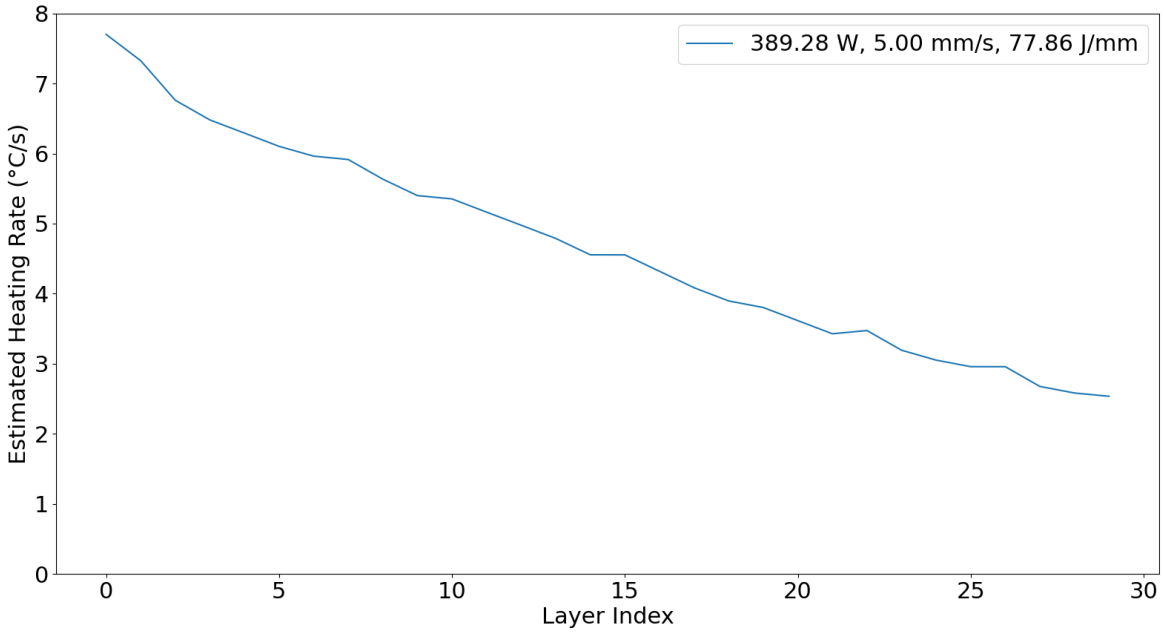


Figure 5.8: Dry Heating Rate vs. Layer Index, 389 W, 5 mm/s, 79.86 J/mm for thermocouple 5 located at the center of the build bed.

Figure 5.8 shows the heating rate versus layer index for thermocouple 5 at the upper end of the heater powers tested, and we can see the expected trend in heater rate - it starts initially high, then decreases as more layers are added. At the surface, it experiences a heating rate of about 8°C per second, while at a depth of 1.5 mm (30 layers) it experiences a heating rate of about 3°C per second, less than half its initial value. The expected exponential decay function is not easily apparent, but the slope does appear to be steepest during the initial layers, and an exponential function can be fitted to these results and experimentally validated during later testing.

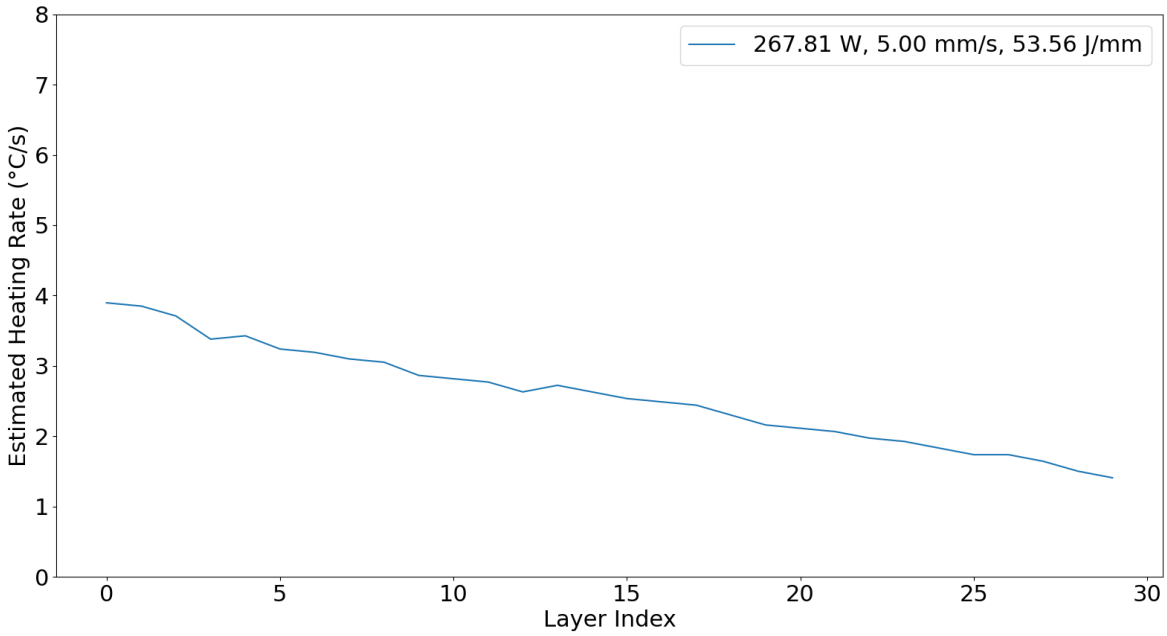


Figure 5.9: Dry Heating Rate vs. Layer Index, 268 W, 5 mm/s, 53.56 J/mm for thermocouple 5 located at the center of the build bed.

The more moderate power displayed in Figure 5.9 has a lower heating rate overall, but otherwise displays the expected trend. The exponential decay is harder to see here and the function essentially appears linear.

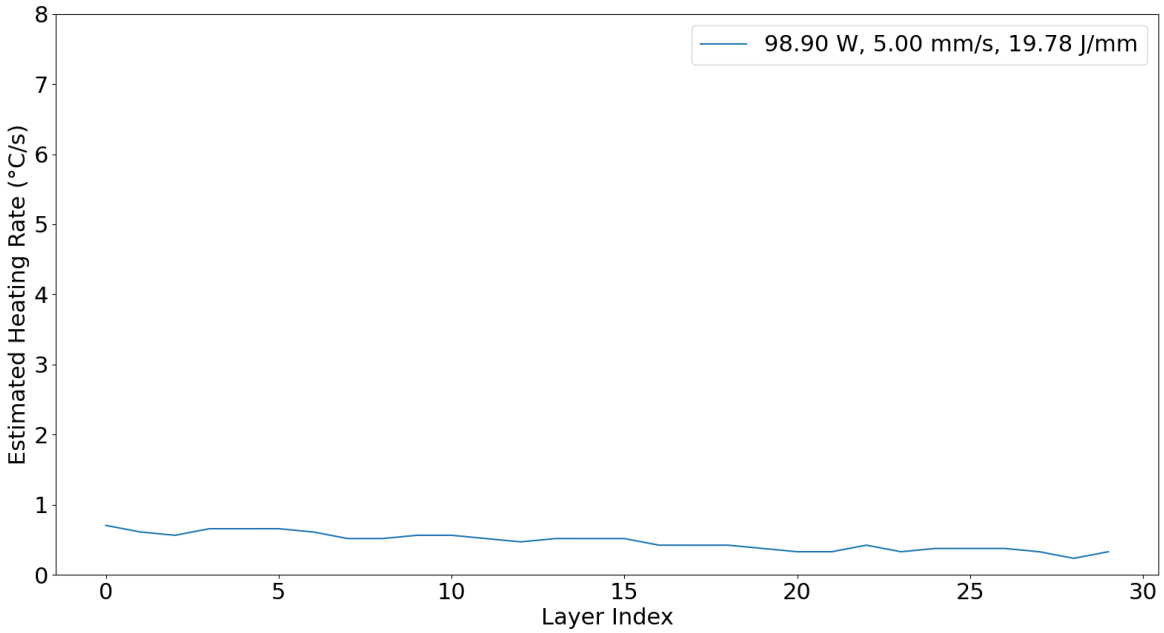


Figure 5.10: Dry Heating Rate vs. Layer Index, 99 W, 5 mm/s, 19.78 J/mm for thermocouple 5 located at the center of the build bed.

At the low power in Figure 5.10, the function appears almost flat compared to the previous figures, with a decreasing trend barely visible. Of note is that, even though it has one-fourth of the power in Figure 5.8, it has less than one-eighth of the surface heating rate. Since the rate of rise of temperature is not proportional to the input power and the heater speed was held constant, this either indicates that the measured input power at the outlet is not a true measure of the radiant lamp output at lower powers, or that transient heat loss effects become comparatively more significant at lower temperatures. The reason why this is the case is not clear at the moment, though it is speculated to be a combination of the following, to be investigated.

1. Higher heater powers act more like an impulse: the timescale at which heating occurs is relatively short compared to the conduction timescale.

2. Higher heater powers result in more depthwise conduction compared to lateral conduction, which may increase the tendency of the powder bed to act as a thermal heat sink (insulated by upper layers of powder), as well as heating the wires themselves.

3. The powder bed walls may experience significant heating at higher heater powers that does not occur (or occurs significantly less) at lower temperatures, inhibiting the amount of lateral conduction that occurs.

A plot showing a representative range of heater powers is shown in Figure 5.11 - the exponential decay is more visible at higher powers, with the absolute differences in heating rate decreasing as depth increases.

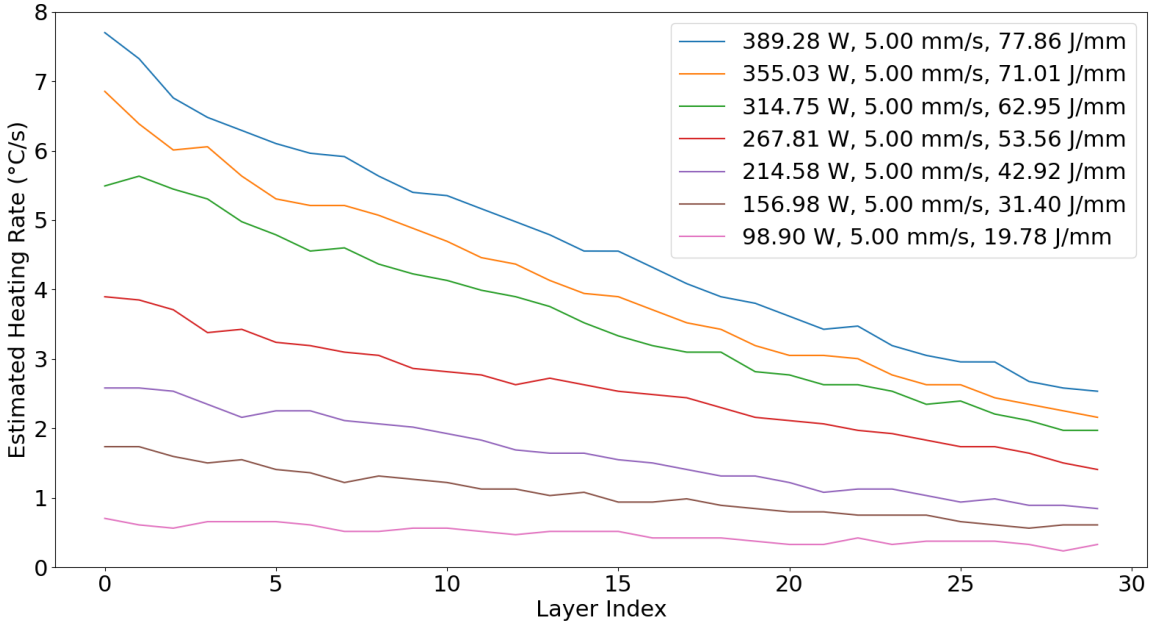


Figure 5.11: Dry Heating Rate vs. Layer Index

To examine the significance of heater parameters on heating rate, we will normalize the heating rate by dividing by the linear energy density. If the heating rate is strictly a function of heater power and speed, then the resulting plot will have the lines lie on top of one another (i.e. halving the linear energy density halves the heating rate). This has been shown to *not* be the case as seen in Figures 5.8, 5.9, and 5.10, and plotting the relationship will give an impression as to the scale to which other factors impact the heating rate.

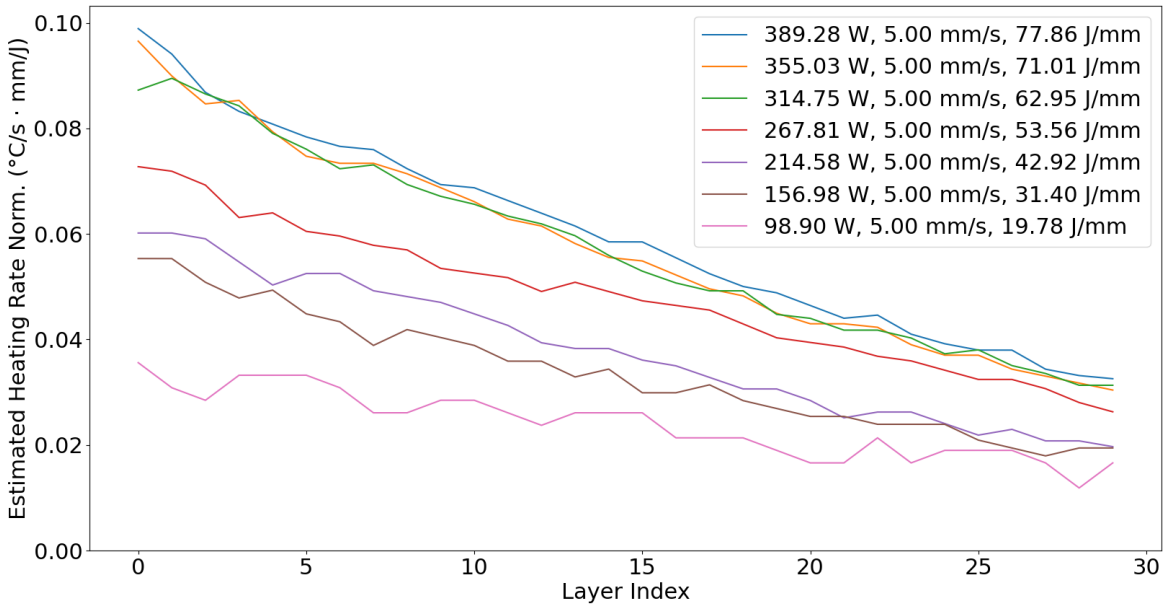


Figure 5.12: Dry Heating Rate Normalized vs. Layer Index

Overall, the lines are closer together in Figure 5.12 than they are in Figure 5.11, which is as expected. Notably, the heating rates at higher heater powers are clustered close together, while the lower heater powers are not clustered together, suggesting that the factors that affect heating rate outside of heater parameters have a initially non-linear dependence on heater power at low values of heater power, but a reduced impact at higher heater powers. This is a weak indication that at very high heater powers, the heating rates are linearly dependent on heater power and speed, with an exponential decay relationship with depth. This is additional evidence that transient heat loss effects are more significant at low temperatures, though quantifying this impact and providing a physical explanation would require more data.

Another way to view this relationship is by plotting the heating rate at the surface (denoted as the 0th layer) against the linear energy density, which should show a non-linear region at lower linear energy densities, and a linear region at higher linear energy densities, shown in Figure 5.13 below.

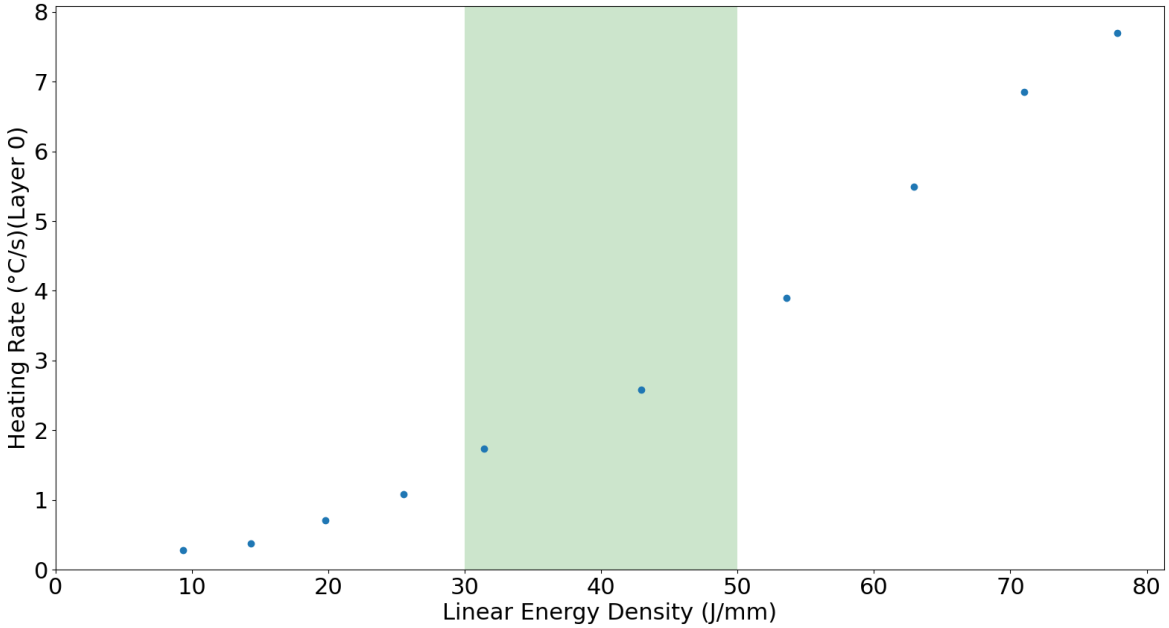


Figure 5.13: Dry Heating Rate at Surface (0th Layer) vs. Linear Energy Density, proposed transition region highlighted.

There is some indication of the relationship mentioned previously in Figure 5.13, with the transition region seeming to occur between approximately 30 J/mm and 50 J/mm, highlighted in green. We can recreate this plot using all dry experiments taken. Of note, the previous figures used only those experiments that had matching time-per-layer with printed experiments, to avoid the effects of different layer times on temperature; since we are only looking at initial layer heating, including data points with different layer times should not have an impact on the results captured in Figure 5.14.

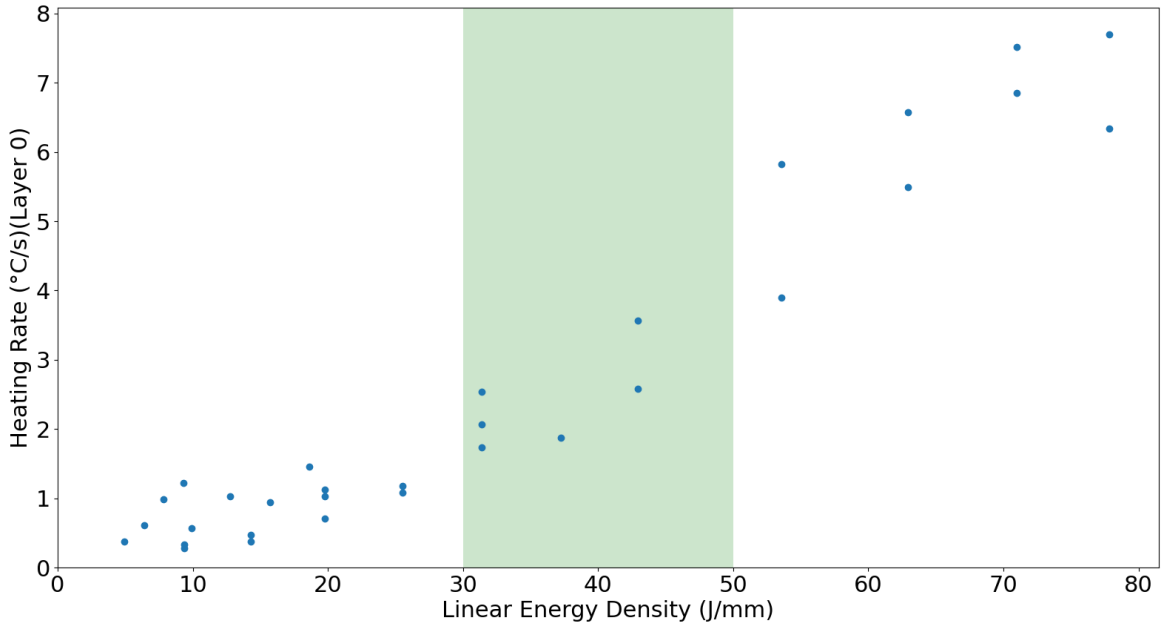


Figure 5.14: Dry Heating Rate at Surface (0th Layer), Full vs. Linear Energy Density

Figure 5.14 does not have a significantly different shape than Figure 5.13, but many of the new data points have heating rates above those in the previous plot, that is particularly noticeable at lower linear energy densities. This may be because some of the data points use higher heater powers at higher speeds, which results in the same amount of radiant energy over a shorter time.

The last phenomena to analyze is the difference in heating rates within the same row of thermocouples. We can see from the full temperature plots in Figure 5.1 that a thermocouple row does not reach equal temperatures - we would like to see how the heating rate differs within the same row to look at possible lateral variation, either due to uneven heating or loss of heat to the wall. The figures below show the heating rates for thermocouples 4, 5, and 6 with respect to the layer index for two experiments with the same heater power and speed (so in principle, the heating rates should be very similar).

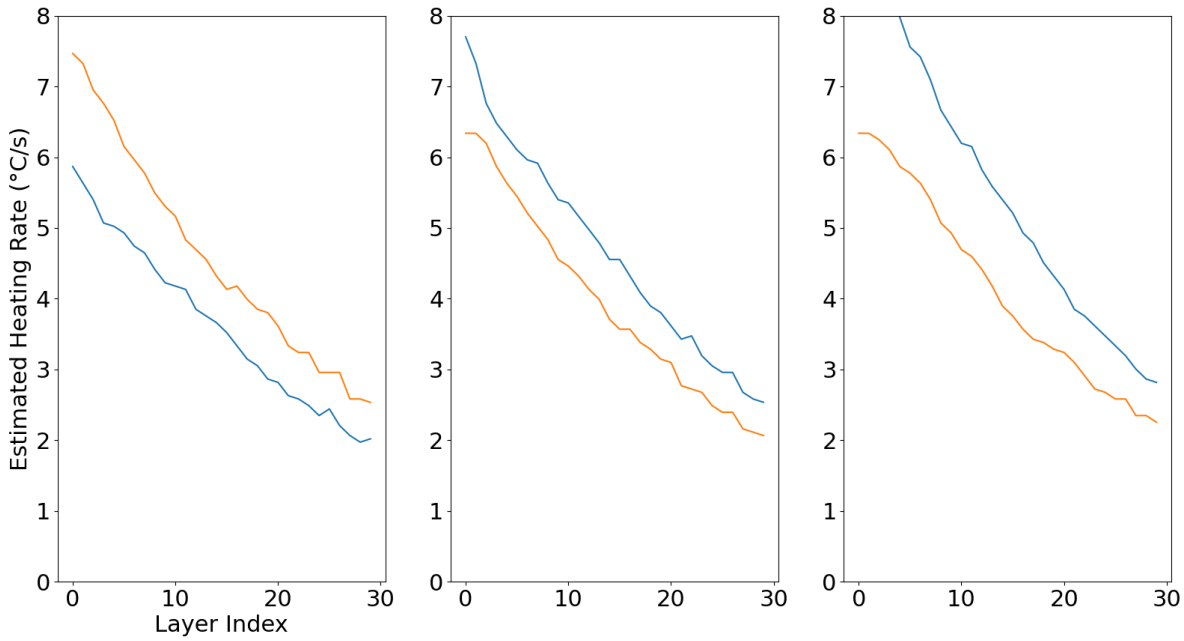


Figure 5.15: Dry Heating Rate across Thermocouples 4, 5, and 6, 389 W, 5.0 mm/s, 77.86 J/mm. One experiment is shown in blue, and one is shown in orange.

For these two experiments, as plotted in Figure 5.15, we can see that for the experiment in blue, the leftmost thermocouple (index 4) experienced the lowest heating rate and the rightmost thermocouple (index 6) experienced the highest heating rate. For the experiment in orange, the result is quite different, with thermocouple 4 showing the highest heating rate.

The main conclusion to be drawn here is that inter-trial variation and initial conditions significantly affects the measured heating rate, and defining a row-wise relationship will need a more robust experimental setup, or the collection of more data to form a representative distribution.

To summarise the results in context of the three sub-analyses mentioned at the beginning of this section:

1. The heating rate decreases as depth increases, with the initial heating rate at the surface fairly high but quickly falling off as more layers of powder are added, due to the very low thermal conductivity of metal powders [12]. This indicates that the most effective heating occurs at the surface, with a rapid drop-off in curing efficiency with additional depth.

2. The heating rate with respect to linear energy density appears to be a non-linear function - doubling the linear energy density more than doubles the heating rate at the surface, at least within the parameter ranges tested.

3. The differences in heating rate within the same row are sensitive to conditions that were not controlled for in this experimentation, and so a general relationship cannot be found from this data set.

5.3.2 Analysis - Peak Temperatures

The peak temperatures that occur in the build bed affects the binder behaviour, as certain binders that rely on polymer reactions will undergo cross-linking at high temperatures or the polymer content will change viscosity. Furthermore, certain solvents, like water, will be completely evaporated at high temperatures, which gives some indication as to the composition of the remaining binder. The work presented here is largely meant to observe the comparison to the same experimental input conditions during the dry vs. printed experiments.

Over the course of one set of heater parameters, thirty layers occur, giving thirty different peak temperatures for each of the nine thermocouples. At some point, a combination of the increase in depth and the heating of the build bed powder from room temperature will result in a "steady-state" temperature where the peaks do not get any higher or begin to drop, due to the thermocouples' distance from the powder surface. The following will be considered.

1. The definition of "steady-state" and whether it is reached within the experimental domain. Has the experiment gone on long enough that the maximum peak temperature has been reached for both dry and printed experiments? This will provide a general understanding of what is the depth at which the effect of the heating lamp is no longer felt.

2. The relationship between the maximum peak temperature and heater parameters. Is there a clear dependence between the two for both dry and printed experiments? The analysis will clarify the maximum peak temperature at different layer depths to infer what may be occurring with the binder and water content (as part of future studies).

3. The differences in peak temperature between thermocouples due to location. How significant is the temperature gradient within the same row or the same column of thermocouples for both dry and printed experiments?

The peak temperatures that occur during an experiment can be presented on a per-layer basis, essentially reducing the full thermocouple data plot to a series of thirty distinct values that happen at a given time and depth. An example of this is shown in Figure 5.16.

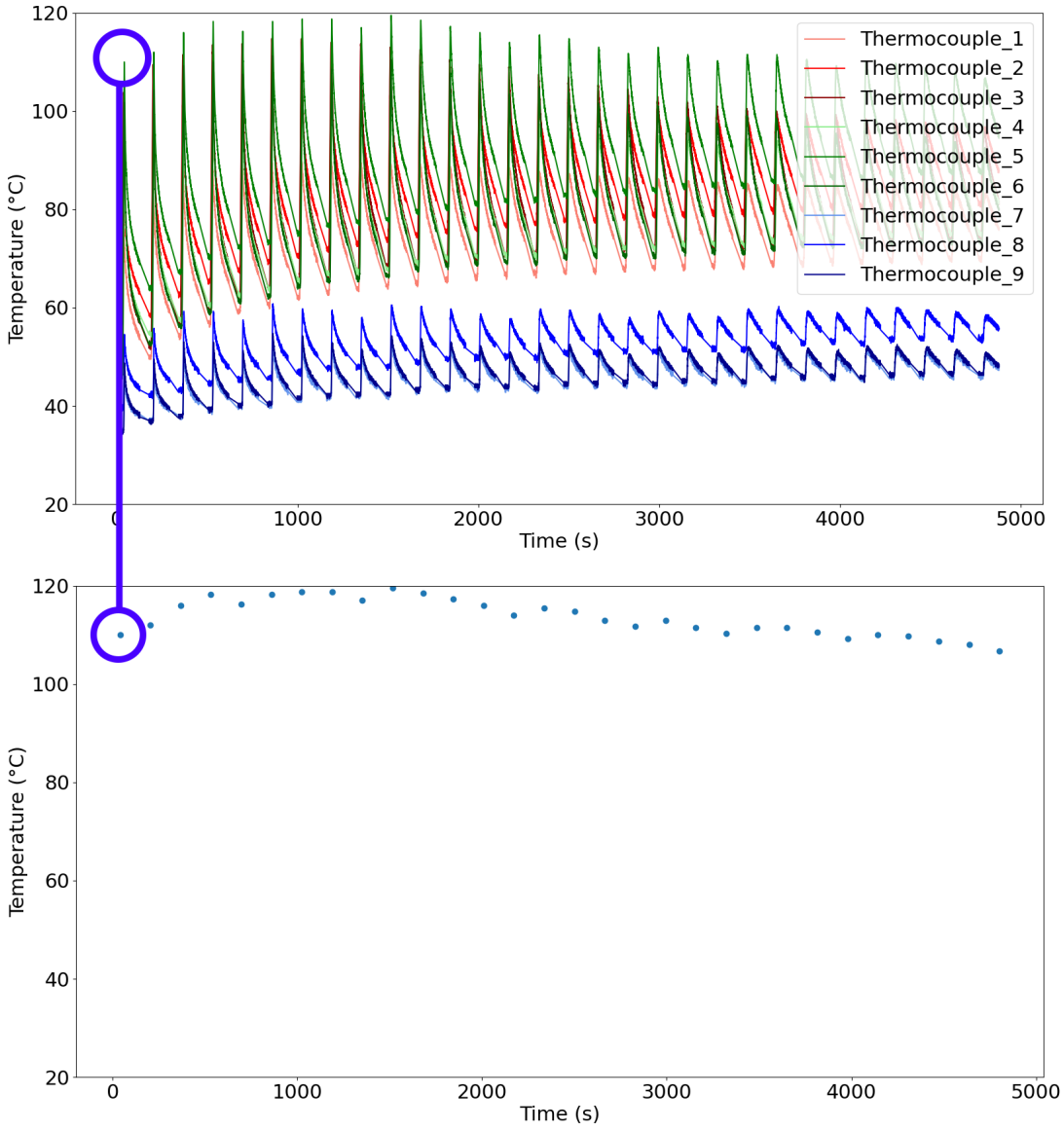


Figure 5.16: Example thermocouple data and corresponding per-layer temperature peaks of thermocouple 5, taken at a heater power of 349 W and a heater speed of 5 mm/s.

The steady-state temperature is the temperature experienced in the bulk powder at depth, and is not necessarily representative of the temperatures reached at the surface due to the insulating effect of the powder and indirect heat lamp exposure. It does indicate the conditions under which the powder and binder are exposed to over a longer-term period, compared to the relatively short time it is exposed to direct heat. This makes the steady-state temperature an indicator of the kinds of chemical and physical reactions that could be occurring in the binder at a specific powder depth, but not necessarily their degree of completion, since the heating is cyclical and the time spent at the peak temperature is very short.

When estimating what the steady-state temperature actually is, based on the reasoning described at the beginning of the section, we will initially assume that the insulating powder layers in this experiment do not cause a large drop in the peak temperatures, and that the main factor for the increase in peak temperature over the course of the experiment is the powder bed heating up from room temperature. The peak temperature as a function of layer index can therefore be modelled as an exponential function asymptotically approaching some value in the limit as the number of layers increase. This relationship can be modelled as the solution to the first order linear time-invariant step response, the general solution of which is given below.

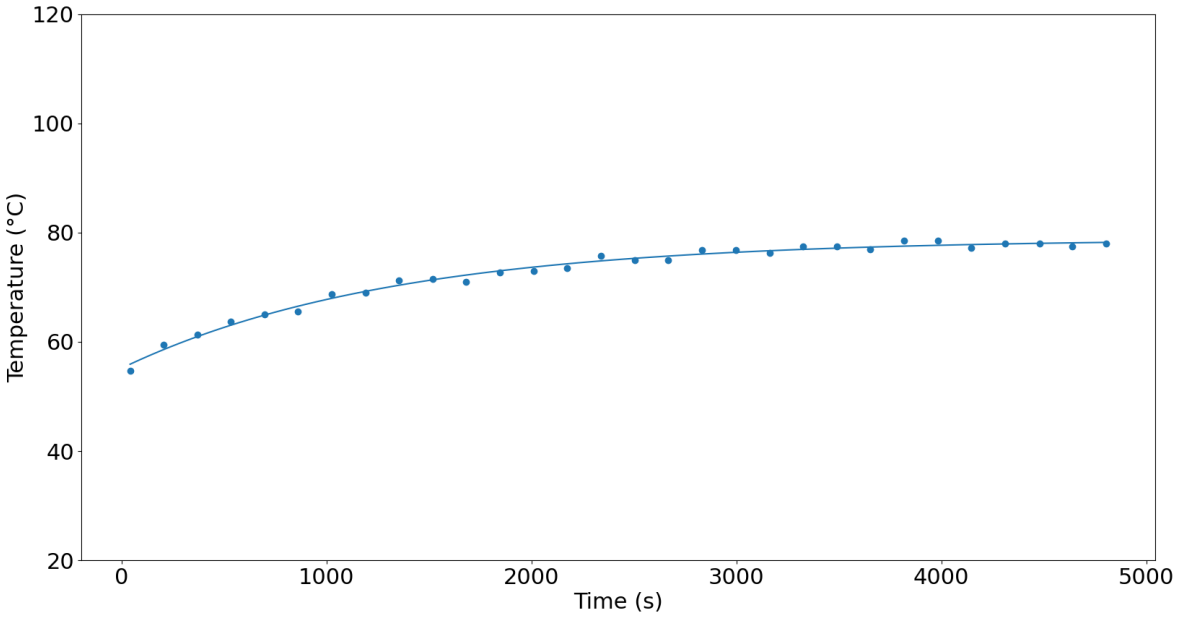
$$
\begin{aligned}
V(t) &= V_0 e^{-t/\tau} + A\tau(1 - e^{-t/\tau}) \\
V_0 &= \text{initial condition } [^\circ\text{C}] \\
t &= \text{time [s]} \\
\tau &= \text{time constant [s]} \\
A &= \text{step function coefficient } [^\circ\text{C/s}] \\
V_\infty &= A\tau = \text{steady state value } [^\circ\text{C}]
\end{aligned}
$$

$$
\begin{aligned}
V(t=0) &= V_0 \\
\lim_{t\to\infty} V(t) &= V_\infty \\
\lim_{t\to\infty} [V_\infty - V(t)] &= 0
\end{aligned}
$$

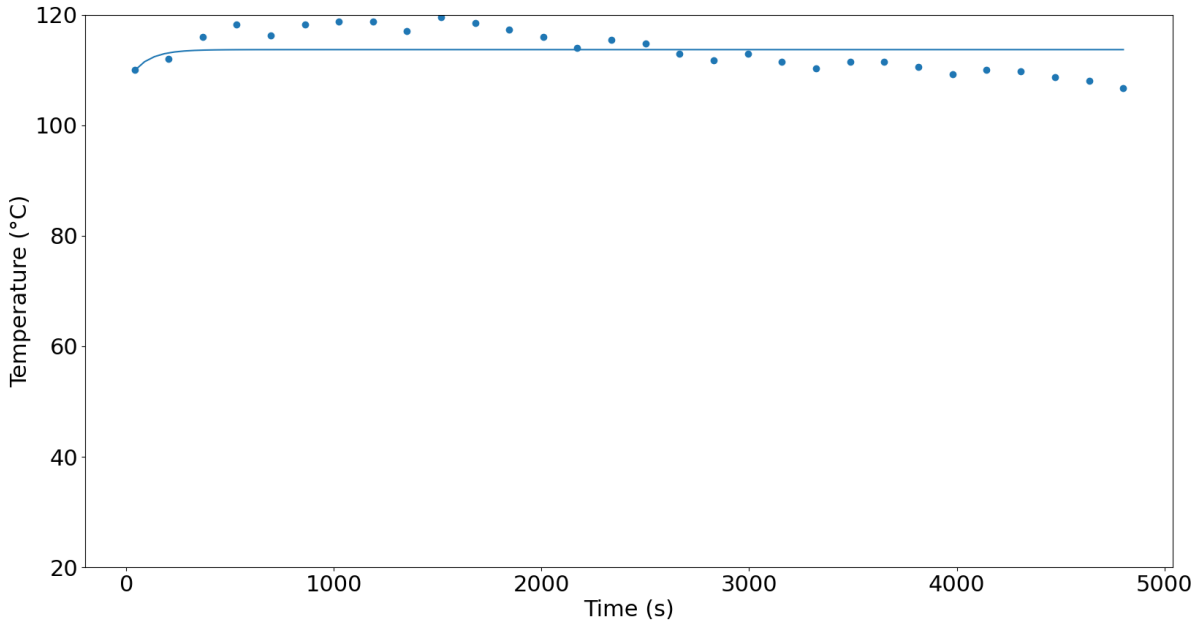
From this, we can use V_0, τ, A as the parameters to be fit in the method of least squares. Ideally, V_0 would be room temperature, but differences in the initial temperature and setup

makes that adding this as an initial condition reduces the quality of fit, especially as we are primarily interested in the time constant. The time to steady-state is dependent on the computed time constant: at $t = 3\tau$, the temperature delta between steady-state and the current temperature is within 5% of its original delta, while at $t = 5\tau$, the delta is less than 1% of its original value.

First, we can select a single thermocouple at the center of the build bed, thermocouple 5, and look at peak sequences that are well-fitted to this relationship and sequences that are not well-fitted. The curves that do not closely fit this relationship (because they reach a maximum and then begin dropping off, or because the solver was unable to converge on a set of parameters) may be due to various reasons. For example, they may have reached a maximum and begun dropping off due to the insulating effects of powder. However, because they do not follow the assumptions made at the beginning of the section, they may need additional consideration. Some examples are shown in Figure 5.17.



(a) Example of a well-fitted curve of peak temperatures for thermocouple 5, taken at 268 W and 5 mm/s.



(b) Example of a poorly-fitted curve of peak temperatures for thermocouple 5, taken at 355 W and 5 mm/s.

Figure 5.17: Well-fitted and poorly-fitted examples of peak temperature curves

Following this, we can take a look at the time constants calculated as a function of the linear energy density as seen in Figure 5.18, and determine the degree to which the experiments reached steady-state temperatures.

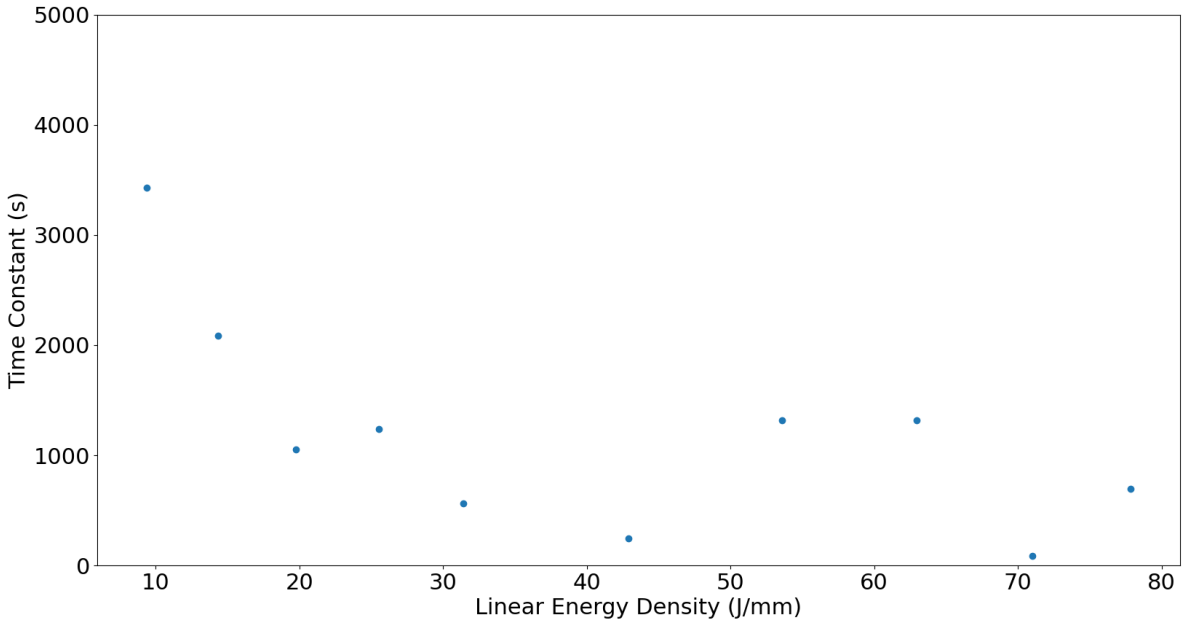


Figure 5.18: Time Constants for Dry Heating Peaks

With some outliers, the general trend appears to be that an increase in linear energy density decreases the time constant (and thus reduces the time and number of layers needed to reach steady-state). This seems reasonable - at high powers, the temperatures rise quickly, resulting in quicker arrival at an equilibrium where heat input and heat output are matched.

Outside of very low energy density values, the time constants are less than 1500 seconds, which indicates that over the course of an experiment (which happens over about 5000 seconds), the measured dry temperatures reach within about 5% of their expected maximum value. For this set of experiments, we can therefore justify claiming that a steady-state temperature is reached during the latter parts of the experiment. Generally, we expect that with lower per-layer times or lower layer thicknesses, the time constant would decrease, due to more rapid heating and lower insulating effect respectively, with the opposite occurring for higher per-layer times and greater layer thicknesses. The per-layer times here are artificially slowed down to match the per-layer times in the printed experiments, which themselves are non-optimal - with improvements to the printing speed, it is expected that the time constants displayed here are close to the upper bound of what would be expected for peak temperatures.

To view the relationship between maximum peak temperature and heater parameters, we can approximate the steady-state temperature as an average of the last five layers, and plot the averaged maximum peak against the linear energy density, as shown below.

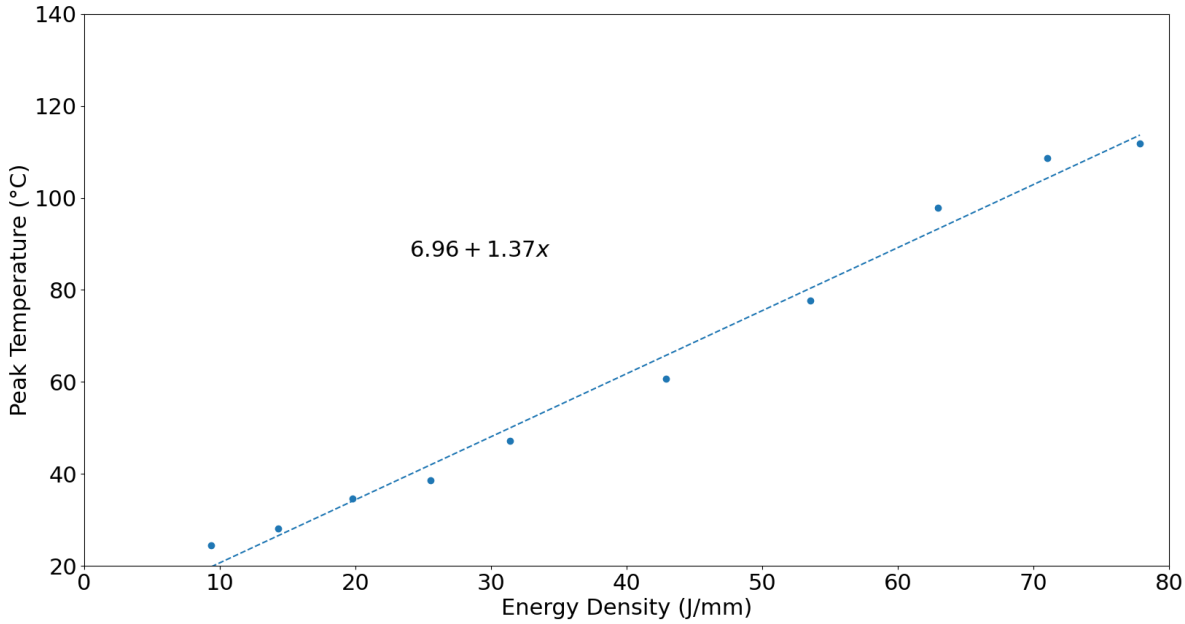
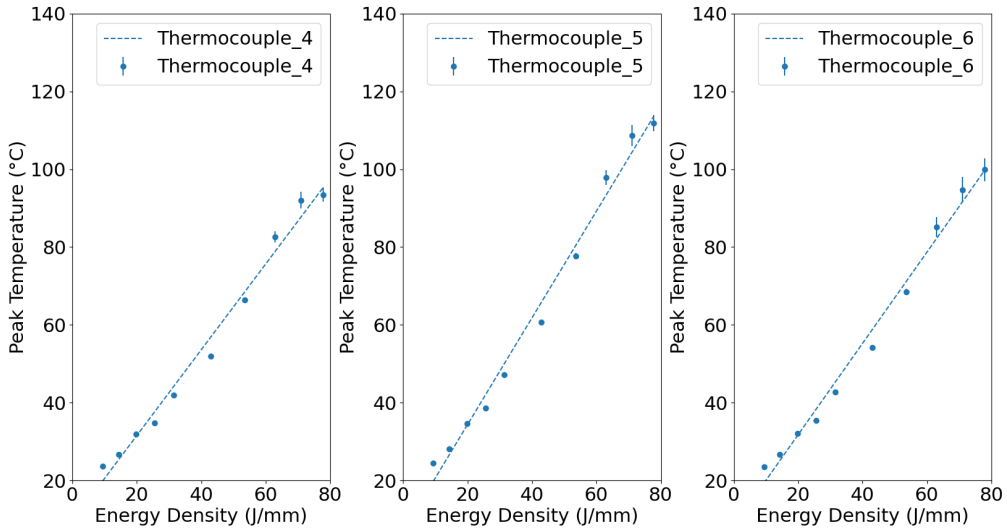


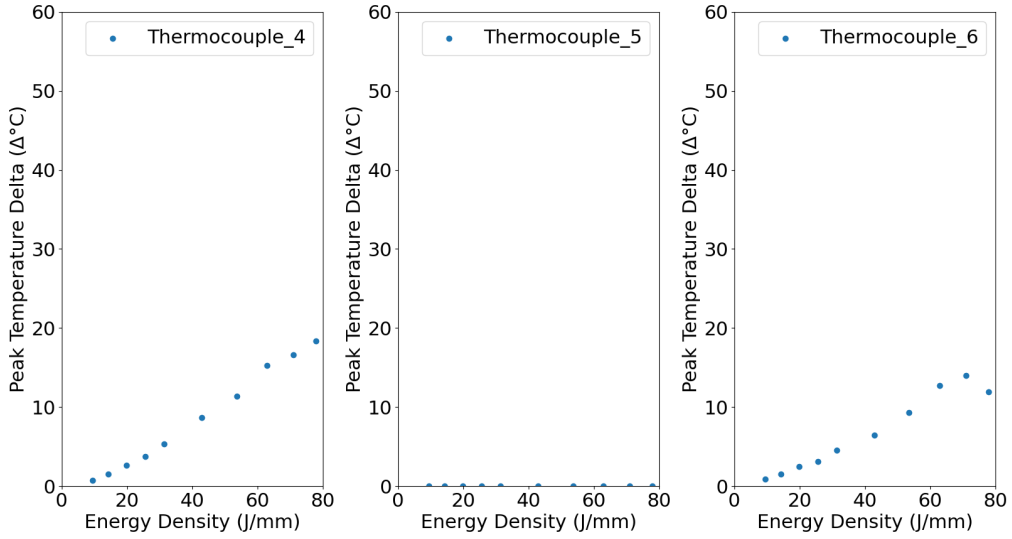
Figure 5.19: Averaged Peak Temperatures of Thermocouple 5 over last five layers vs. Linear Energy Density

From the data displayed in Figure 5.19, we can see that there is a roughly linear relationship between linear energy density and the approximated steady-state temperature at depth across the range of parameters tested. Additionally, the heater parameters tested cover the range of peak temperatures that would be desirable to reach in the bulk powder (insofar as they are capable of evaporating water while minimizing the risk of surface warping), and so provides a predictor for estimating steady-state temperatures at depth for a particular heater and powder system. This dataset indicates that it can be possible for the evaporation and chemical reactions to continue to occur at specific depths, which is an important factor when considering the powder and binder material system.

Thus far, we have only considered the peak temperatures observed at the center of the build bed. We can compare the different positions by plotting the same relationship shown in Figure 5.19 alongside one another for measured peak temperatures.



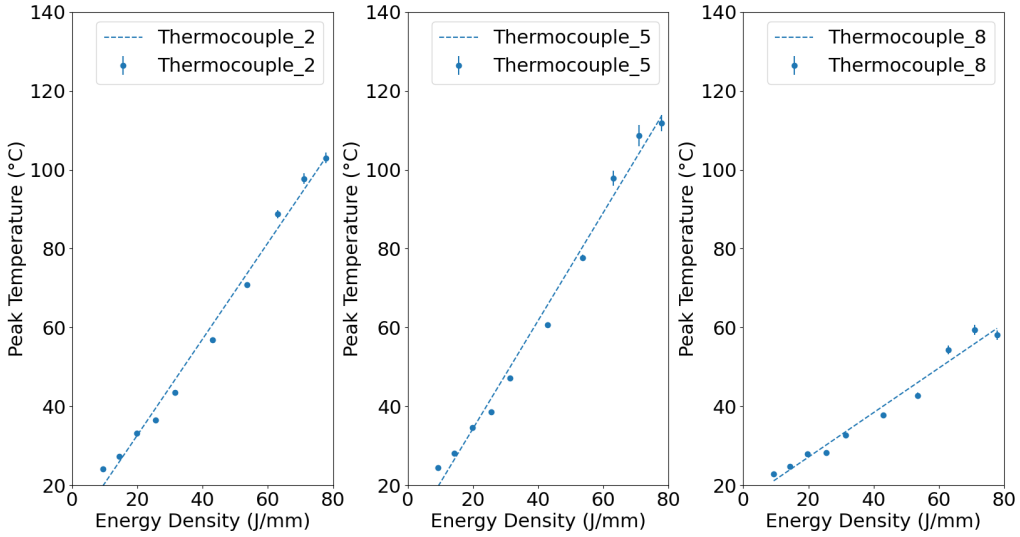
(a) Averaged Peak Temperatures (Thermocouple 4, 5, 6) vs. Linear Energy Density



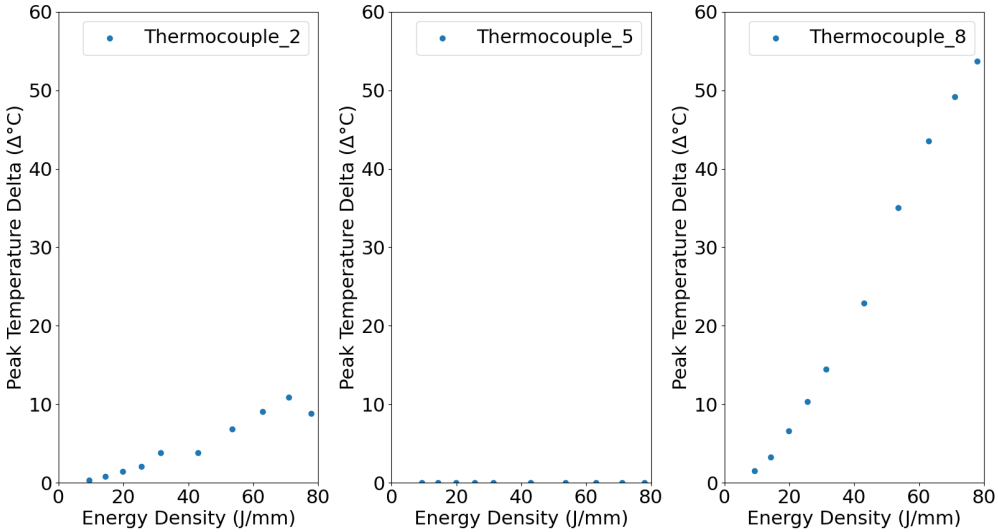
(b) Temperature differences from thermocouple 5. At 80 J/mm, thermocouple 5 reaches an averaged peak temperature about 20°C hotter than thermocouple 4 and over 10°C hotter than thermocouple 6.

Figure 5.20: Averaged Peak Temperatures over the last five layers (Thermocouple 4 to 6) vs. Linear Energy Density. This figure is for the thermocouple measurements in the center row, showing that the temperatures are highest in the center, as expected.

When comparing the peak temperatures obtained at the center row of the build bed (thermocouples 4, 5, and 6) as seen in Figure 5.20, the thermocouple at the center records the highest temperatures, with the two measurement locations taken closer to the walls having lower temperatures, with the difference increasing with linear energy density. The difference is large enough to indicate an uneven heat distribution across the row of thermocouples, or equivalently across the powder bed. The peak temperatures can vary by more than 10 °C across the bed, which can influence the fluid evaporation and binder curing properties. These aspects have been shown to result in different green part properties, such as strength and deformation [4].



(a) Averaged Peak Temperatures (Thermocouple 2, 5, 8) vs. Linear Energy Density



(b) Temperature differences from thermocouple 5. At 80 J/mm, thermocouple 5 reaches an averaged peak temperature of about 10°C hotter than thermocouple 2 and over 50°C hotter than thermocouple 8.

Figure 5.21: Averaged Peak Temperatures (Thermocouple 2, 5, 8) vs. Linear Energy Density. As noted previously, the bottom row of thermocouples (Thermocouple 7, 8, 9) are not fully covered by the heater pass.

The peak temperatures across the center column (thermocouples 2, 5, and 8) as seen in Figure 5.21, the measurements show an expected temperature distribution, with the top and center thermocouples measuring significantly higher values, while the thermocouple near the bottom (which is in a region not fully covered by the heater) having comparatively low peak temperatures.

Summarizing the results in this section,

1. The temperatures measured at the thermocouples during the latter layers is expected to be within 5% of the steady-state value of the fitted curve for all but very low heater powers, indicating that the temperature of the bulk powder has minimal effect on peak temperature (and thus curing) beyond the first few layers.

2. There is a linear relationship between the steady-state temperatures and the linear energy density of the heater, as observed by Dressler et al. [12], suggesting a straightforward calibration of heater power to surface temperature.

3. The peak temperatures are the highest at the center of the build bed. The thermocouples in the same row reach lower peaks, as do the ones in the top row. The lowest temperatures occur because of the incomplete heater traversal over the build bed. This shows that even for large heaters that fully cover the powder bed, there are significant differences in the temperatures achieved, and curing is likely location dependent.

5.3.3 Analysis - Cooling Rates

Cooling rate affects temperatures post-heating and gives some insight about the heat loss and approximate heat capacity of the powder bed. As in the previous plots, the temperatures drop quickly immediately after reaching their peak, then less rapidly for the remainder of each layer measurement. We will primarily consider the peak-to-trough delta (that is, the difference between the peak temperature of one layer and the starting temperature of the next, over a given time span) and the non-linear cooling function. More specifically, the work will elucidate:

1. The effect of powder depth on peak-to-trough temperature delta. Typically, we would expect a smaller delta at greater depths due to the insulating effect of the powder above the thermocouple. This measurement is important, as it gives an indication of temperature fluctuations as a function of powder bed depth. Such temperature fluctuations may influence part shrinkage and distortion, as well as layer shifting (shown in Figure 5.22) and cracking.

2. The time constant of the cooling rate with respect to the depth. Generally, we expect to have a higher time constant (slower temperature drop) at greater depths; this can also be attributed to the insulating effect of the powder stacked above the thermocouple layer-by-layer. Additionally, the heating of the build bed from room temperature due to cyclic exposures to the heat lamp layer-by-layer means that the temperature gradients in the depthwise direction will be smaller, further slowing down heat loss.

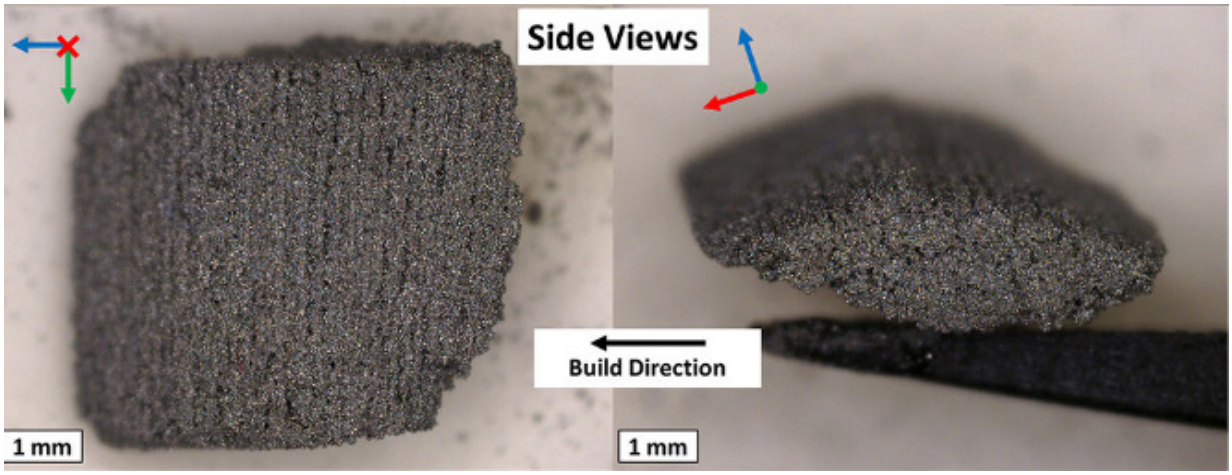


Figure 5.22: Layer shifting defect of SS316L part intended to be cuboid. Adapted from [27].

For this analysis, we will consider the cooling rate based on the temperature delta that occurs between the peak temperature of one layer and the initial temperature of the next layer, and the time between them. We can consider this cooling rate both based on a simple linear approximation, as well as an exponential decay, similar to the exponential model used in the previous section.

The trend of the peak-to-trough delta can be observed by plotting the peaks, troughs, and associated deltas on the same plot, with the following figures showing measurements taken from the center of the build bed (thermocouple 5). This can be seen in Figure 5.23.

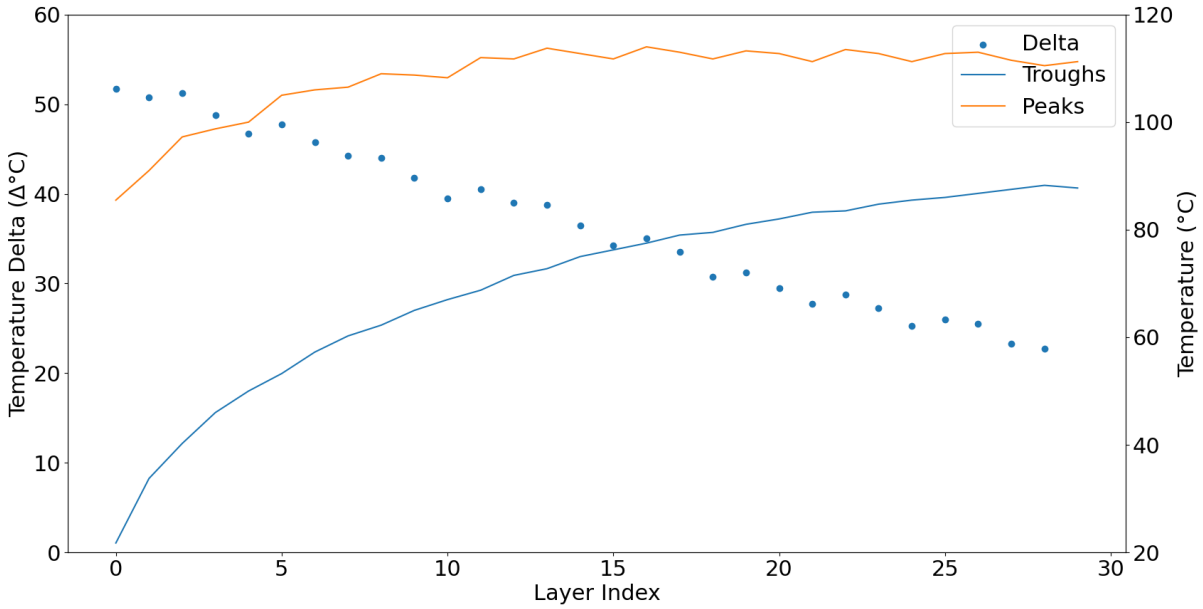


Figure 5.23: Peak-to-Trough Delta, 389 W, 5 mm/s, 79.86 J/mm for thermocouple 5. The orange line is the peak temperatures for each layer, and the blue line is the minimum temperatures for each layer, with the temperature indicated on the right axis. The dots indicate the difference between the peak and trough values, with the delta indicated on the left axis.

In Figure 5.23, the upper line shows the peak temperature and the lower line shows the trough temperature (with their values on the right axis). The dots show the difference between them, with its value on the left axis. In this, we can see that the delta starts out initially high, with a 50°C difference between the peak and trough, then steadily decreases as more layers are added and the bed continues to heat up, down a minimum difference of about 25°C. The peaks level out at a maximum relatively quickly, while the trough temperatures continue to rise as more heat is added to the powder material system layer-by-layer.

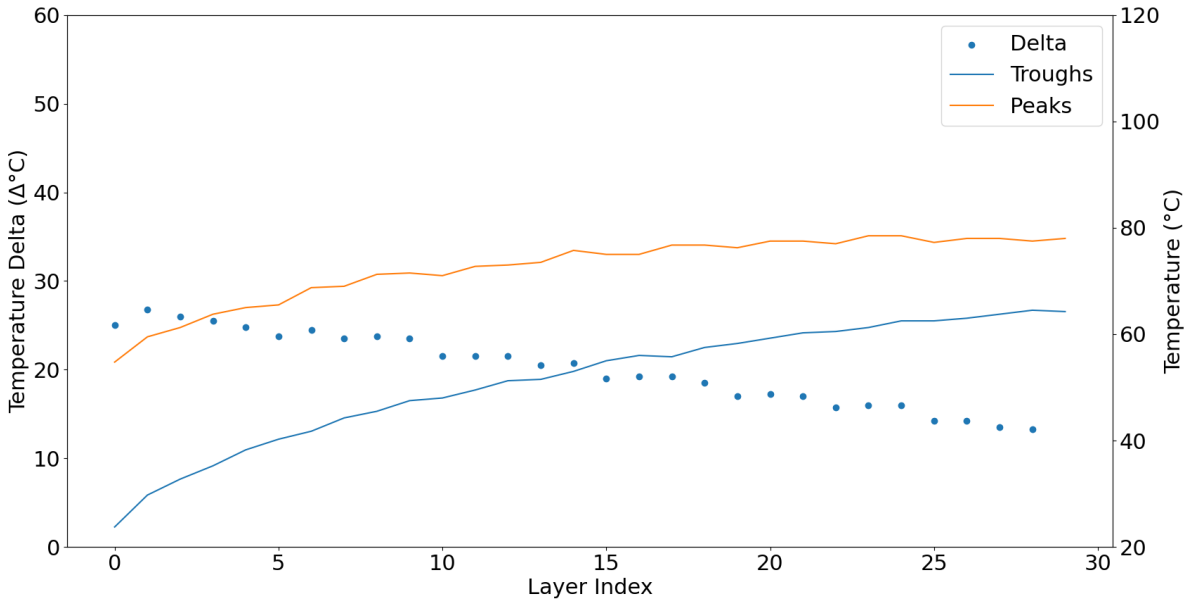


Figure 5.24: Peak-to-Trough Delta, 268 W, 5 mm/s, 53.56 J/mm for thermocouple 5.

At lower heater powers, as shown in Figure 5.24, there is a similar trend with the deltas decreasing with layer index, with the differences being that the temperatures involved are lower, and the peak temperatures do not reach a maximum as quickly. Based on the previous two plots, we expect that, were this experiment to continue for more layers, the peak and trough would continue to get closer together, with the delta eventually shrinking to zero, as the effect of the heating lamp will be diminished the more powder layers are stacked on top of the thermocouples.

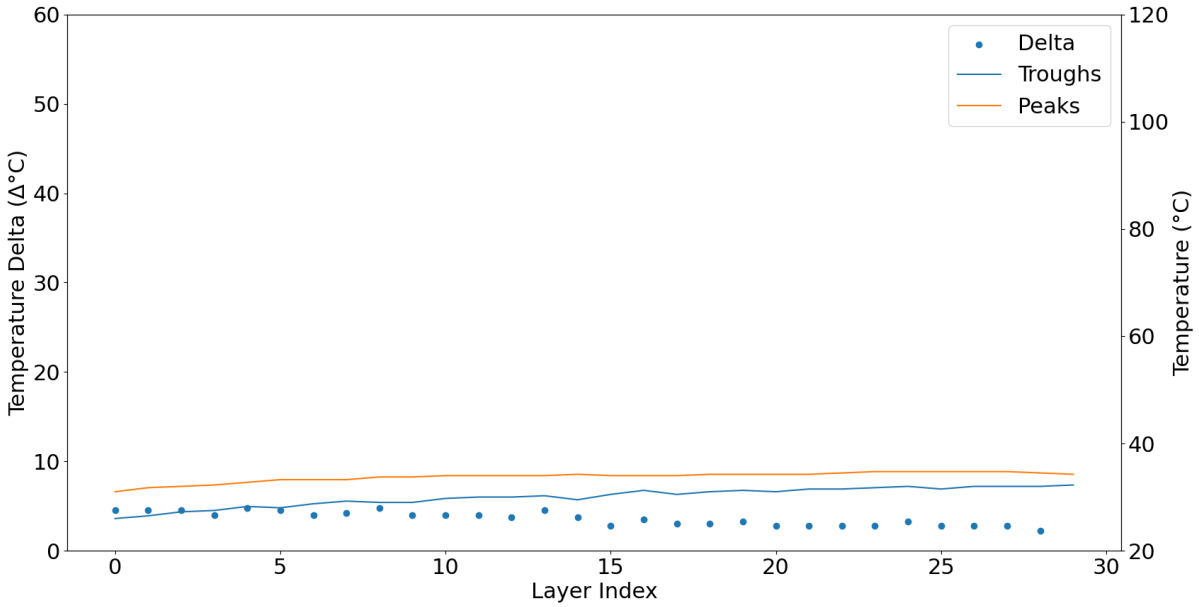


Figure 5.25: Peak-to-Trough Delta, 99 W, 5 mm/s, 19.78 J/mm for thermocouple 5.

At very low heater powers, as seen in Figure 5.25 the patterns observed previously are just barely visible, due to the low thermal energy present. While the temperatures continue to rise, they do so at a very slow rate, with the peak and trough differing by 5°C or less.

Overall, the peak-to-trough delta behaves as expected, with the caveat that the trough temperature rises over a longer period of time than the peak temperature over the course of the experiment. Otherwise, we see a typically expected exponential decay in the delta as the layers increase and the bed heats up.

The second phenomena we would like to observe is the time constant of the cooling with respect to the depth. As the depth increases, powder is laid over top of the measurement location, partially insulating it. Additionally, as the bed heats up, the difference between the peak and trough temperatures decreases, as does the temperature gradient for heat loss through conduction. In general, we would expect to see the time constant increase, and the temperature at the thermocouple to be higher for a longer period of time.

We can define the function to be fit identically to the equation in the previous section, shown below. The sample points to be fit for the cooling rate begin at the peak of the layer ($t = 0$) and end when measurements for that layer conclude (immediately before powder spreading begins).

$$
\begin{aligned}
V(t) &= V_0 e^{-t/\tau} + A\tau(1 - e^{-t/\tau}) \\
V_0 &= \text{initial condition } [^\circ\text{C}] \\
t &= \text{time [s]} \\
\tau &= \text{time constant [s]} \\
A &= \text{step function coefficient } [^\circ\text{C/s}] \\
V_\infty &= A\tau = \text{steady state value } [^\circ\text{C}]
\end{aligned}
$$

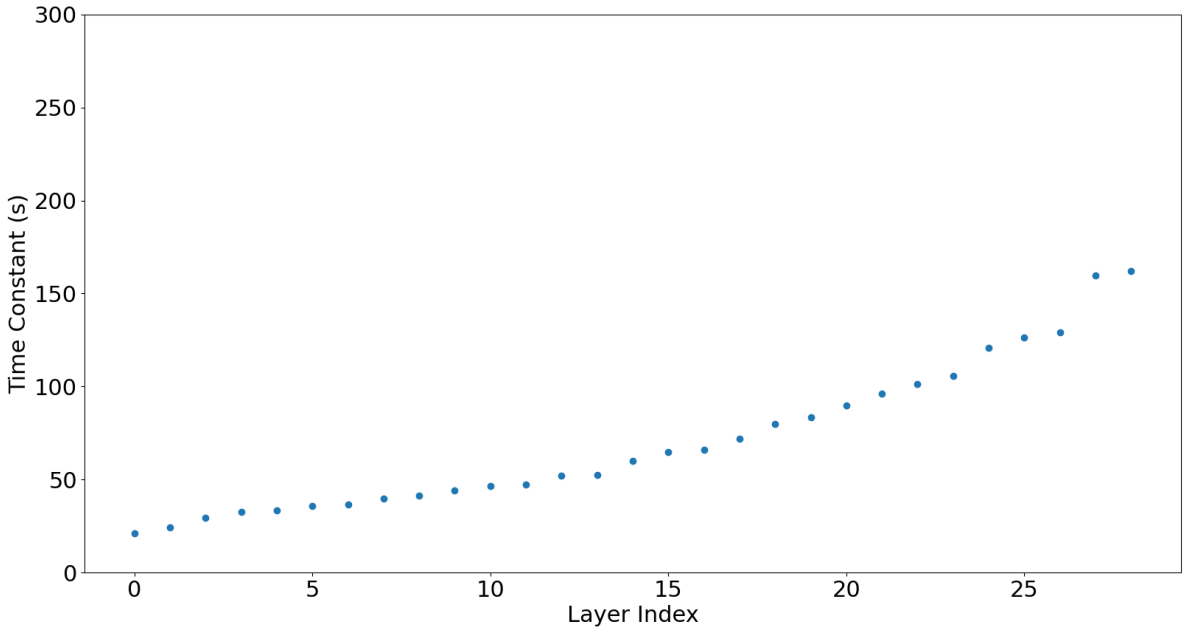


Figure 5.26: Cooling Time Constants vs. Layer Index, 389 W, 5 mm/s, 79.86 J/mm for thermocouple 5. This indicates that the cooling is rapid for the earlier layers, when the thermocouples are closer to the surface.

According to Figure 5.26, the time constants for cooling increase with additional layers, indicating that the speed at which the powder cools down decreases as the experiment progresses, with the increase being non-linear with respect to the layer index. As the peak-trough delta is also decreasing, the absolute rate at which cooling occurs is much slower than during the beginning layers.

Since the parameters in this experiment represent a "worst-case" in terms of time (with actual printing on industrial systems being faster), this indicates that, over the course of twenty to thirty "high-power" heating cycles, the powder at depth maintains an elevated temperature for substantially longer compared to the beginning layers.

To examine the fitness of the step response curve for capturing the cooling down behaviour of the powder, we can examine the fitted curves on a per-layer basis, which are shown in Figures 5.27, 5.28, and 5.29.

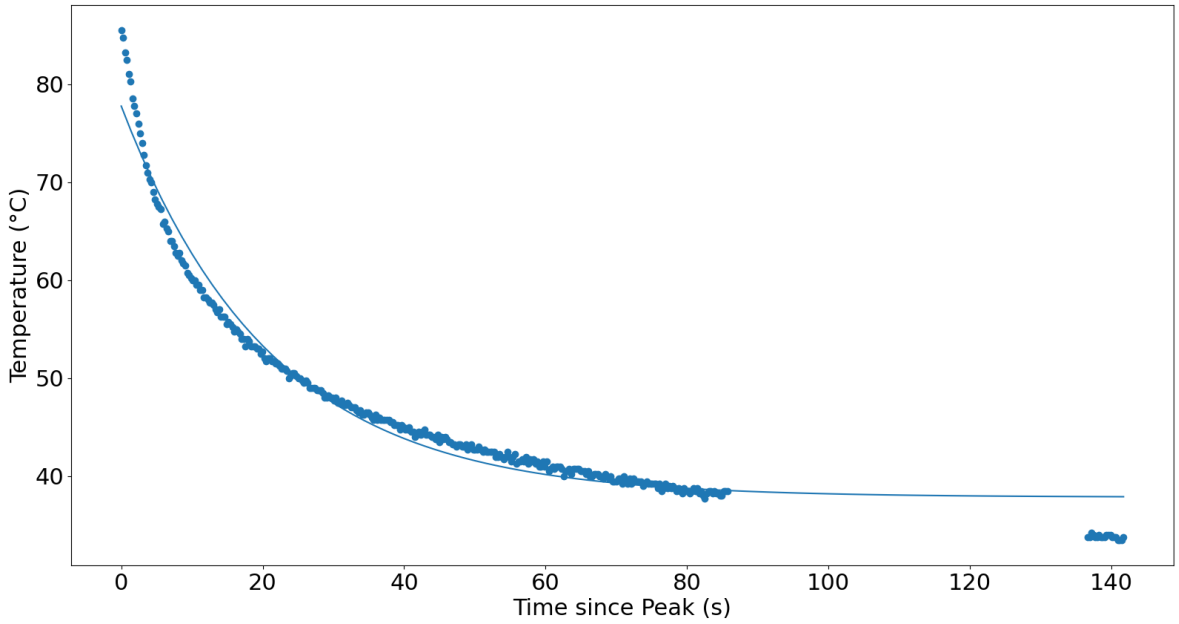


Figure 5.27: 0th Layer Cooling, 389 W, 5 mm/s, 79.86 J/mm for thermocouple 5. The temperature measurements for the cooling down period of the surface (0th layer), plus some additional measurements from the start of the next layer are shown. The fitted curve is also plotted.

Figure 5.27 shows the temperatures and fitted curves during the cooling down portion of the heating cycle.

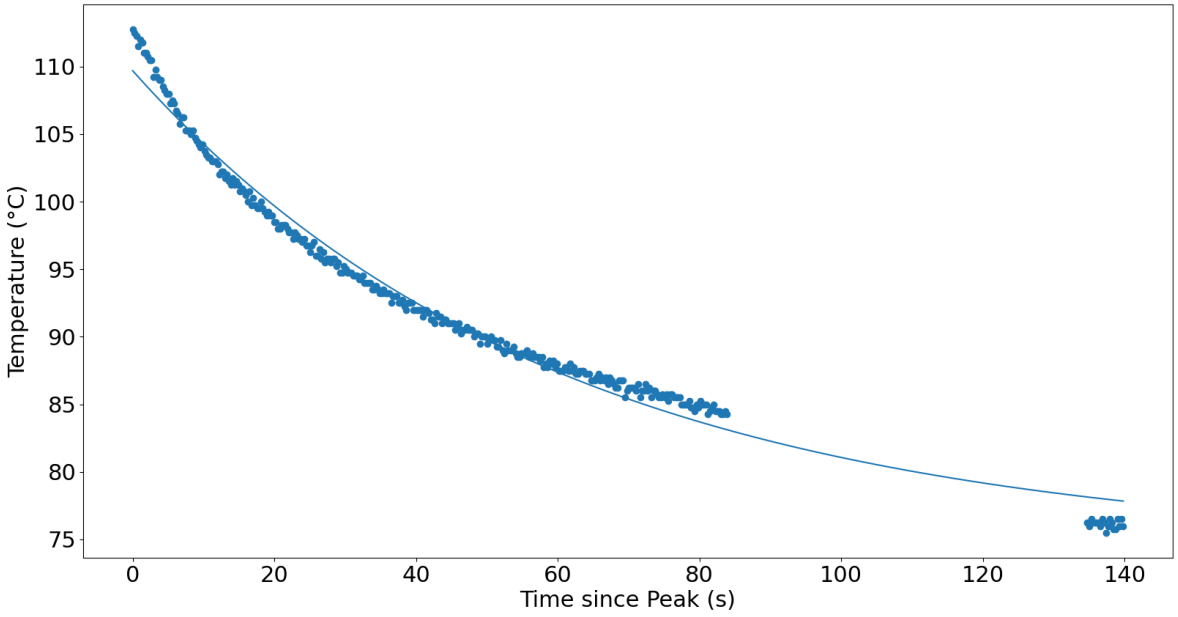


Figure 5.28: 14th Layer Cooling, 389 W, 5 mm/s, 79.86 J/mm for thermocouple 5.

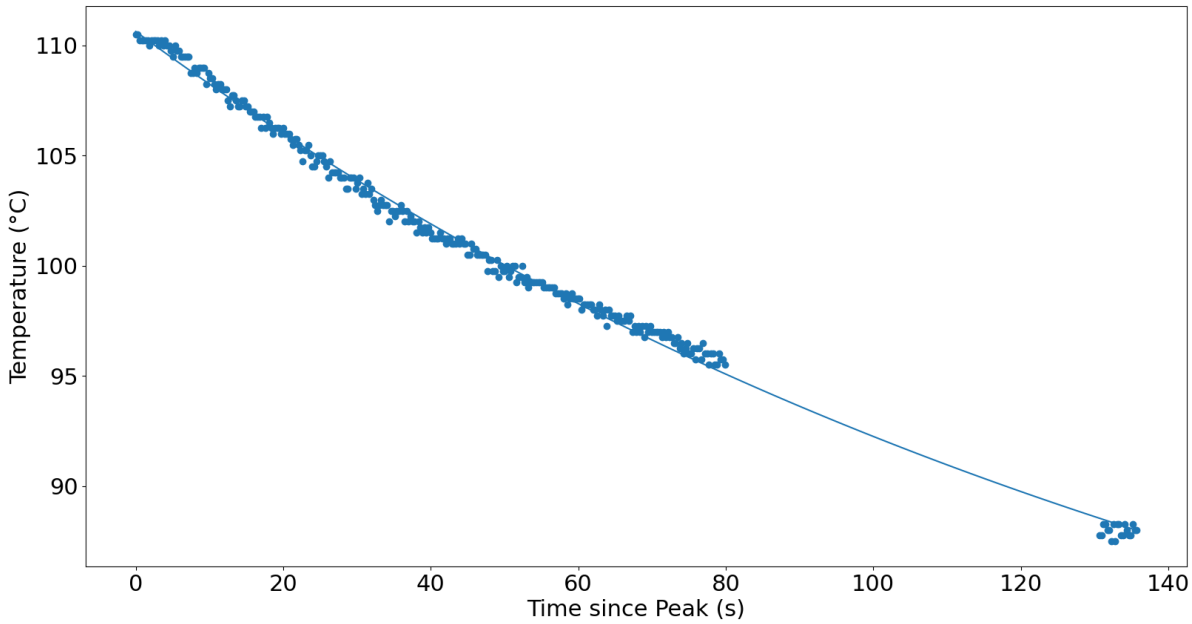


Figure 5.29: 28th Layer Cooling, 389 W, 5 mm/s, 79.86 J/mm for thermocouple 5.

During the initial layers of the experiment, the second derivative of the temperature is much higher than later on. That is, the cooling at the 0th layer shows an initially sleep slope before flattening, as in Figure 5.27, with the slope changing dramatically over the course of the heating and powder spreading cycle. During the last layers, the temperature plot is nearly linear by comparison, as in Figure 5.29.

Lastly, we can examine the time constants at a lower heater power, to examine the difference in cooling time constants.

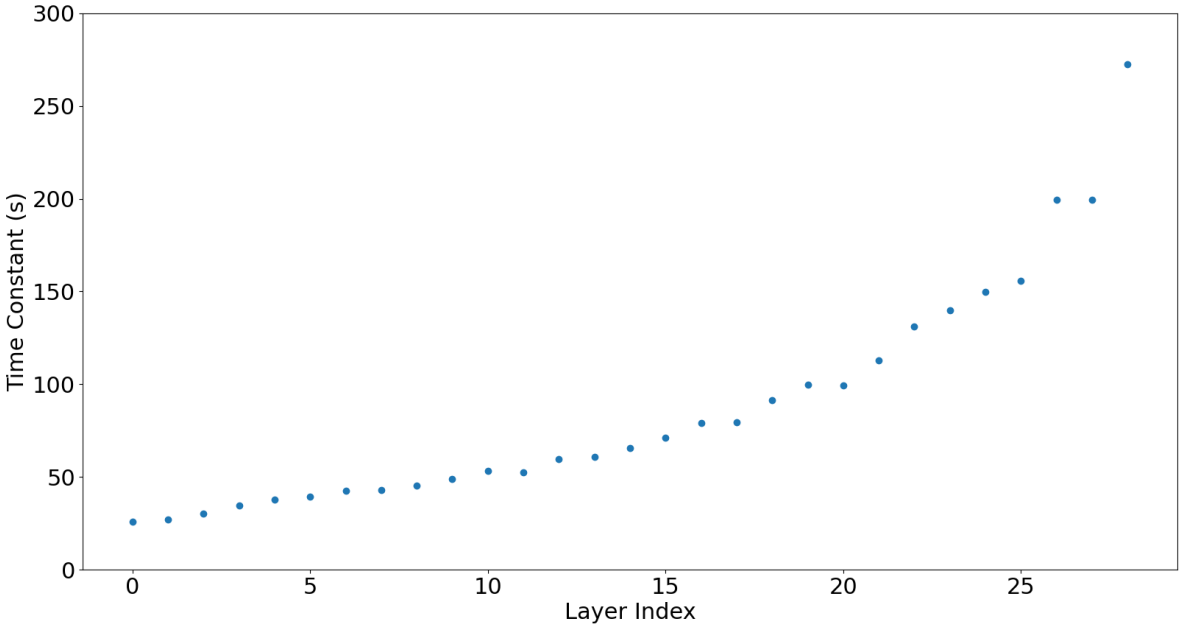


Figure 5.30: Cooling Time Constants, 268 W, 5 mm/s, 53.56 J/mm for thermocouple 5. Compared to Figure 5.26, the time constants are higher, especially for the latter layers.

In Figure 5.30, the cooling rate time constants at a lower power show a similar trend to the higher heater power in Figure 5.26, but reaches higher time constants sooner, indicating that the temperature does not decay as quickly, as expected.

In summary:

1. The peak-to-trough delta experiences a gradual drop over the course of the experiments performed, with the trough temperatures increasing more rapidly than the peak temperatures, producing a more gradual temperature curve and decreasing the defect rate due to slower thermal cycling.

2. The cooling rate decreases during later layers, with the fitted time constants increasing non-linearly with respect to the layer index.

5.4 Analysis - Impact of Aqueous Binder on Temperature Measurements

The presence of an aqueous binder increases the thermal mass of the substrate, by adding water and other chemicals to the metal powder. At the same time, liquid evaporation is expected to be endothermal. The behaviour of the binder under heating in terms of thermal signatures is the primary interest of this study, and we would like to compare the temperature changes here to those in the dry powder section, to assess if there is a significant change caused by the presence of binder. To the best of the author's knowledge, this type of comparison has not been accomplished before.

5.4.1 Analysis - Heating Rates of Dry vs. Printed Layers

In principle, the heating rate for the same heater power and speed would be lower compared to the dry powder bed due to the additional thermal mass of the binder and evaporation effects - we will use a similar heating rate estimation as in the previous section to look for any differences due to binder addition. We will consider the following questions:

1. The change in heating rate for a selected thermocouple as depth increases - between dry and printed substrates, is there a measurable difference in the relationship between temperature and powder depth? This information will help inform how to tune the heating lamp to ensure appropriate binder evaporation and polymer characteristics.

2. The change in heating rate for a selected thermocouple with the heater power and speed (at the same depth) - between dry and printed substrates, does the presence of binder substantially slow down the rate of heating?

3. The difference in heating rates between thermocouples in the same row - are the extremities of the build bed affected differently with binder present?

We will use the same linear approximation of heating rate described in Section 5.3.1, where the largest rise over run across twenty samples is taken as the heating rate. Similar to what was observed in dry powder, we expect that the heating rate decreases with layer index, and that the additional thermal mass of the binder will decrease the overall rate at which the powder-binder material system heats up.

In Figure 5.31, the temperature plots display the heating rates as a function of layer index in the center of the build bed (thermocouple 5). The blue line shows the dry powder heating rates, and the orange line shows the wetted or printed powder heating rates under the same heating conditions.

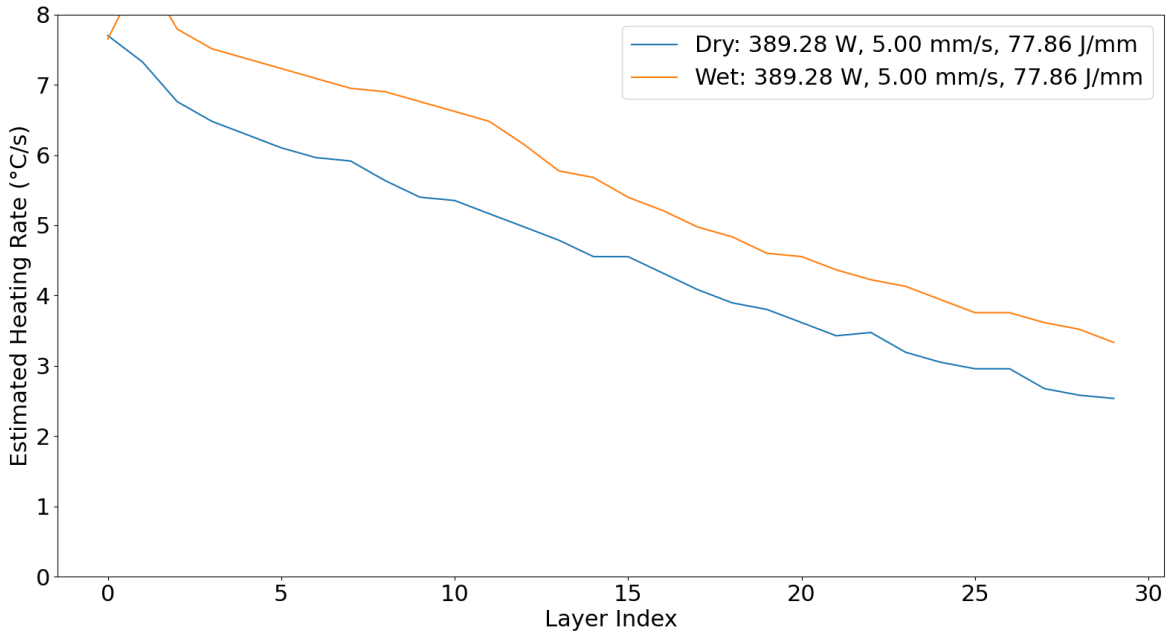


Figure 5.31: Dry and Printed Heating Rate vs. Layer Index, 389 W, 5 mm/s, 79.86 J/mm for thermocouple 5. The dry heating rates vs. layer index are shown in blue, while the printed heating rates are shown in orange.

At the highest heater power tested, shown in Figure 5.31, the heating rate in the wetted powder is higher across the board, with an average difference of 0.98°C/s and a standard deviation of 0.26°C/s between the two curves. The temperature here does almost immediately reach a peak of over 100°C, which indicates that most of the water has boiled off, leaving a small volume of liquid binder. The higher heating rate across the experiment may be due to the better contact between the thermocouple sensor and the powder-binder material compared to the powder alone. Another possibility is that the kinetic energy of the binder droplets impacting the powder substrate further compact the powder, locally increasing the effective thermal capacity and conductivity of the material system [1].

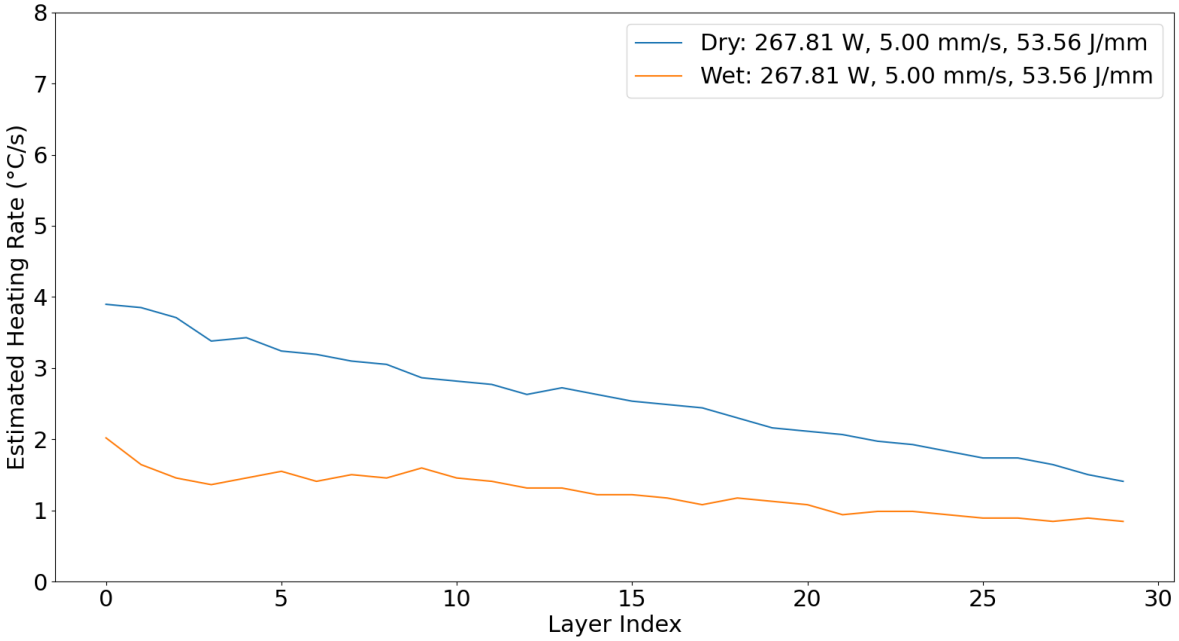


Figure 5.32: Printed Heating Rate vs. Layer Index, 268 W, 5 mm/s, 53.56 J/mm for thermocouple 5.

In Figure 5.32, which uses a more moderate heating power, the heating rate is lower across the course of the experiment, potentially due to the higher heat capacity of the powder-binder material system. The average difference between the two curves is 1.33°C/s, with a standard deviation of 0.45°C/s.

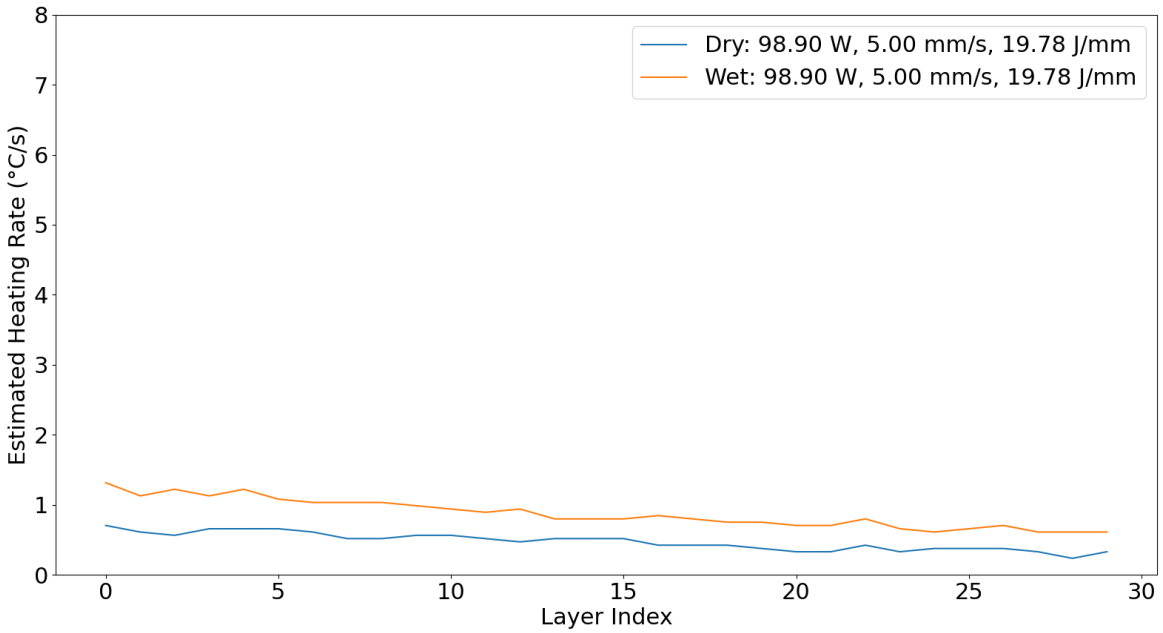


Figure 5.33: Printed Heating Rate vs. Layer Index, 99 W, 5 mm/s, 19.78 J/mm for thermocouple 5.

Figure 5.33 shows the heating rate comparison at a low heating power. The experiments selected show that the experiment with the presence of binder has a higher heating rate, but the difference is quite small, with an average difference of 0.40°C/s and a standard deviation of 0.10°C/s between the two curves.

Figures 5.34 and 5.35 show the heating rates as a function of layer index across multiple different heater powers, both as an absolute value and normalized with respect to the linear energy density.

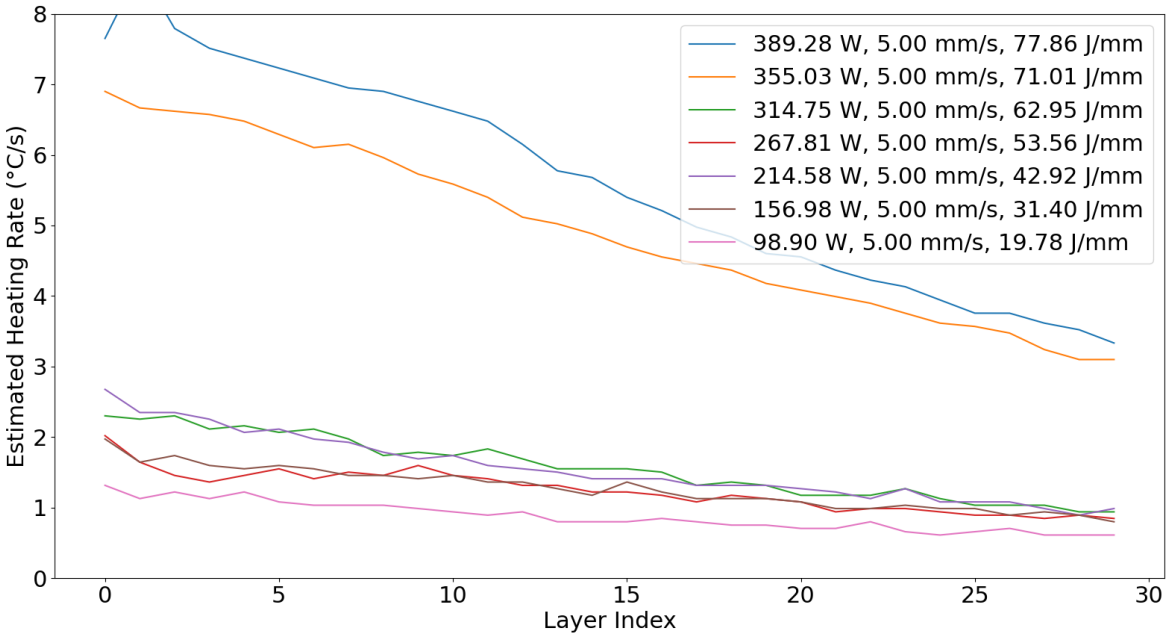


Figure 5.34: Printed Heating Rate vs. Layer Index

In Figure 5.34, there are two apparent groups of heating rates, where once the heater power passes a certain threshold, the heating rate jumps up significantly. Incidentally, the top two heater powers tested are able to consistently produce temperatures above 100°C, while the lower heater powers are never able to reach that temperature, so there is an indication that the presence of water produces a moderating effect on the rate of temperature rise.

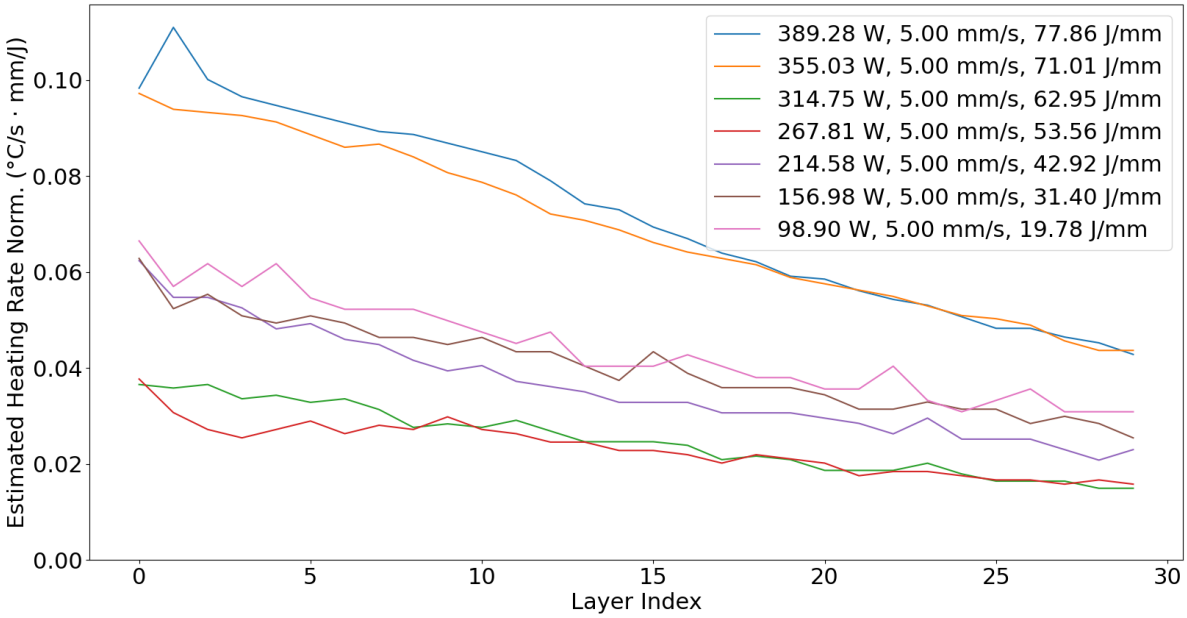


Figure 5.35: Printed Heating Rate Normalized vs. Layer Index

In Figure 5.35, the trend is similar, with the top two heater powers close to each other (i.e. the rate of heat rise is proportional to the heater power). The lower heater powers are clearly separated from the top two, indicating that in printed powder beds, there is a sharp transition in heating rate for aqueous binders depending on the presence of water and whether it has evaporated. Of note, in dry powder beds, the transient temperature change from room temperature also results in a non-linear relationship between heating rate and heater power, but with a less stark transition between lower and higher heater powers.)

As in the dry powder heating rate analysis, the heating rate at the surface (0th layer) can also be plotted as a function of heater power, shown in Figure 5.36 below.

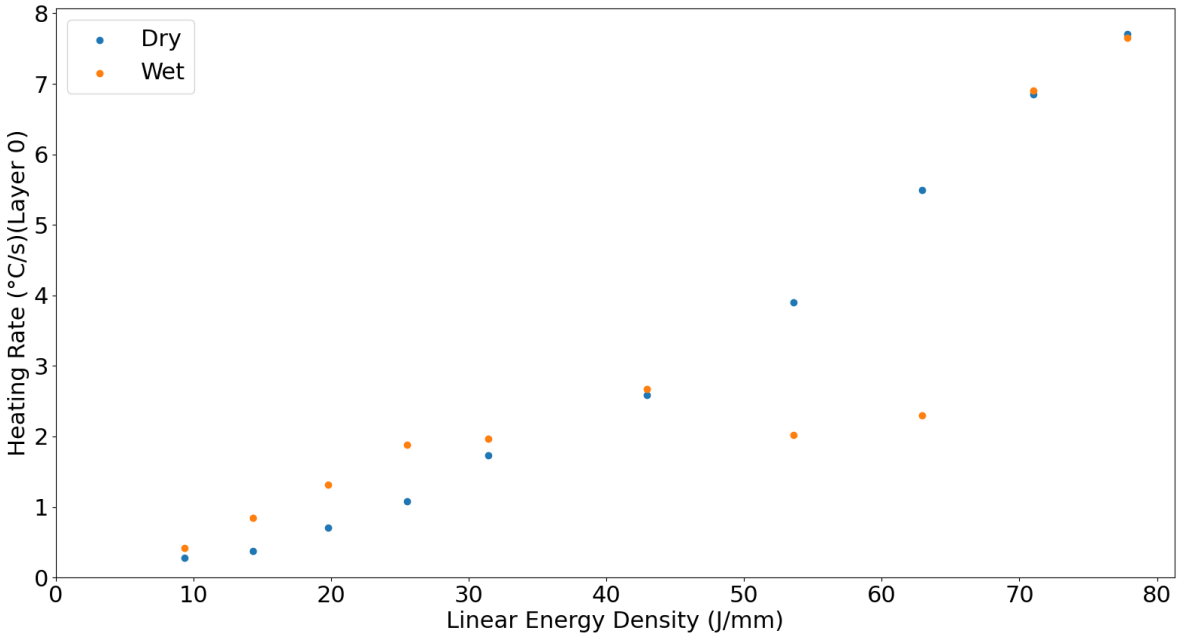


Figure 5.36: Heating Rates at Surface (0th Layer) vs. Linear Energy Density. Dry and printed heating rates presented for comparison. Noted discontinuity occurs between 60 J/mm and 70 J/mm.

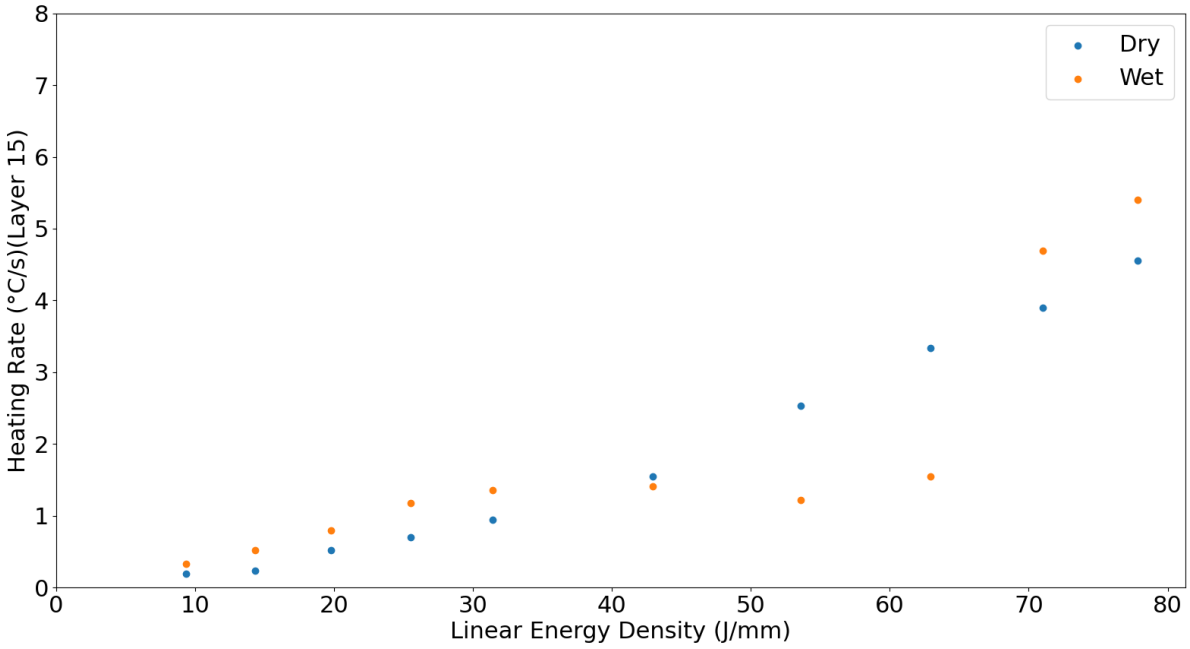


Figure 5.37: Heating Rates 0.75 mm deep (15th Layer) vs. Linear Energy Density

Unlike in the dry powder tests, where the trend between the linear energy density and the heating rate was continuous, in Figure 5.36, there is evidence of the discontinuity previously mentioned around the 60 J/mm to 70 J/mm mark, with this trend continuing at deeper layers, as in Figure 5.37. This discontinuity observed for the wet powders can be attributed to the fluid evaporation effects at lower linear energy density values, where evaporation is endothermal, rapidly removing heat from the system, whereas at higher linear energy density values, the binder solvent is fully evaporated and thus has little impact on heating rate.

Lastly, the difference in heating rate is presented between thermocouples in the same row in Figure 5.38. We expect to see the same variation seen in the dry experiments present here.

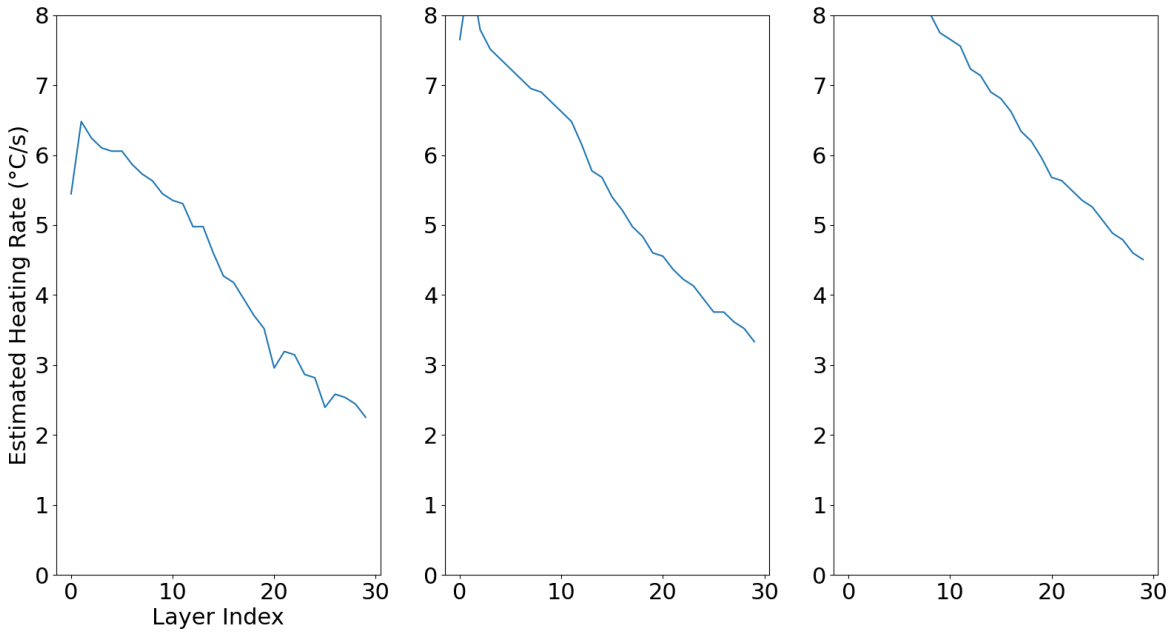


Figure 5.38: Printed Heating Rate across Thermocouples 4 to 6, 389 W, 5 mm/s, 77.86 J/mm

The heating rates shown in Figure 5.38 does show a variation across the row, but as mentioned in Section 5.3.1, this is likely due to a combination of minor variations in thermocouple depth and the heater position relative to the powder bed.

In summary:

1. The differences in heating rates (dry vs. wet) as a function of depth do not have a clear relationship in the experiments tested. More data would be needed to draw a conclusion and quantify any differences in heating rate caused by the presence of binder.

2. There is a discontinuity in heater power and heating rate - that is, at a certain power, the heating rate increases dramatically. The hypothesized reason is the total evaporation of the water present in the aqueous binder - with the majority volume of the binder boiled off, the heating rate at high heater powers is on par with the dry experiments. At lower heater powers, this is not the case, and the heating rate is equal or lower than the corresponding dry powder heating rates. This can lead

to the powder being heated more gradually prior to evaporation, lowering resultant thermal stresses.

3. As in the dry experiments, the variation within a row suggests that minor differences in experimental setup (due to the manual nature of the levelling procedure) can lead to very different results, and a different method of setting up the temperature measurements may be needed to improve consistency.

5.4.2 Analysis - Peak Temperatures

Similarly to the heating rate, in theory, the peak temperatures obtained should be lower for the same heater parameters due to the addition of the binder. The following phenomena will be considered as part of the research questions, as a direct contrast to the dry experimental results.

1. Has the experiment gone on long enough that the maximum peak temperature has been reached? Does the wetted powder take appreciably longer to reach this "steady-state" temperature?

2. For the relationship between the maximum peak temperature and heater parameters, does the relationship differ from that of dry powder?

3. For the differences in peak temperature between thermocouples due to location, do the different locations reach very different peak temperatures with binder or in the dry state?

Similarly to Section 5.3.2, the peak temperatures obtained can be plotted as a function of layer index and fitted with the LTI first order response and the time constant can be evaluated.

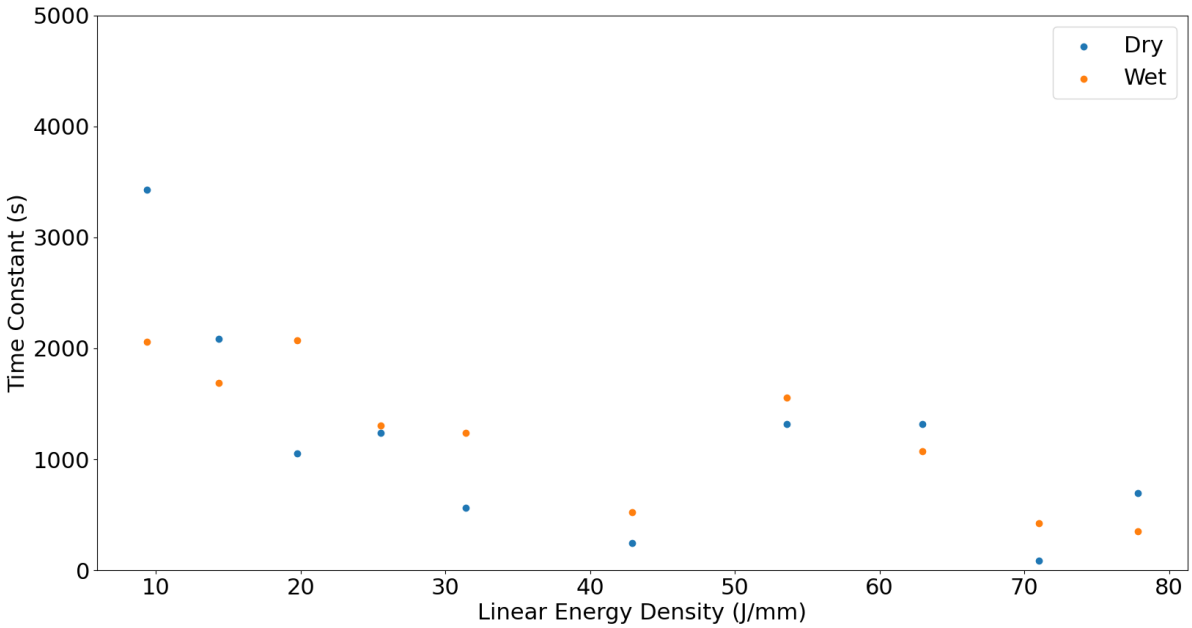


Figure 5.39: Time Constants for Dry and Printed Heating Peaks

From Figure 5.39, we can see that the time constants are approximately the same for the wet experiments as for the experiments without binder. Similar to the dry experiments, the peak temperatures are reached within 5% of the fitted steady-state value by the final layer. Overall, the rate at which they reach this steady-state remains about the same.

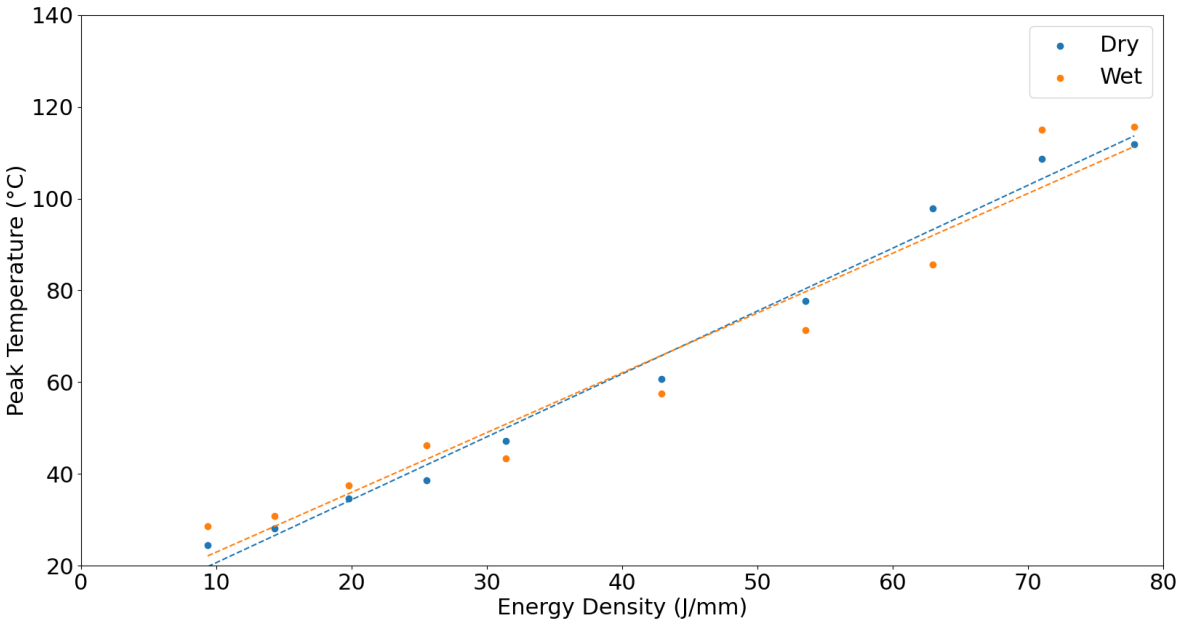
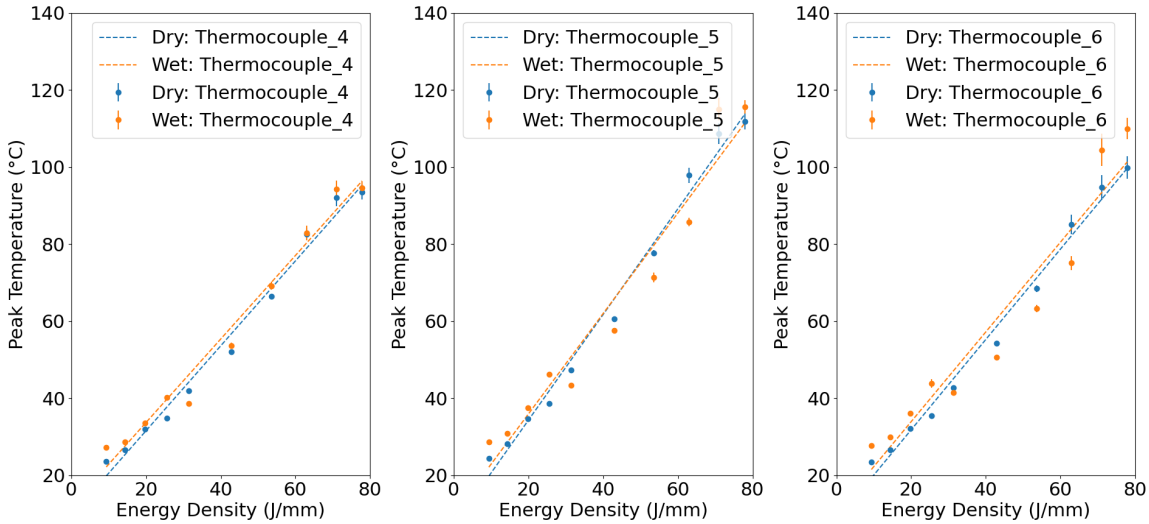
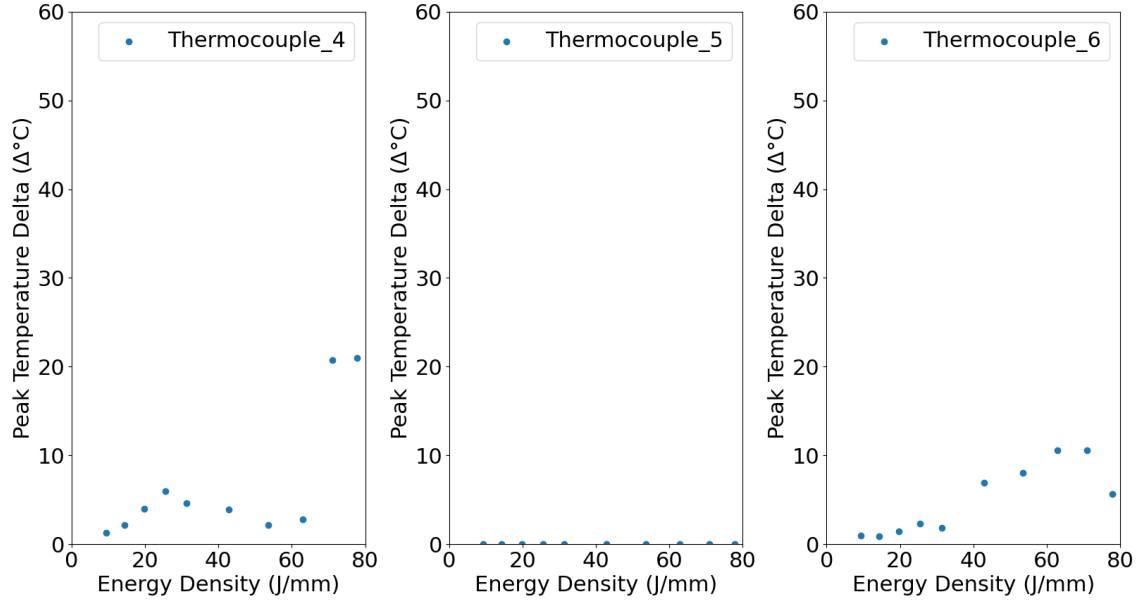


Figure 5.40: Averaged Peak Temperatures vs. Linear Energy Density

In Figure 5.40, the average peak temperature over the last five layers of the experiment is plotted against the linear energy density of the heater. Compared to the dry experiments, the slope of the linear fit is almost the same: that is, given a set of heater parameters, after several heating cycles, the temperatures at depth are the same with and without binder. As the differences between the peak temperatures between dry and printed experiments have been fairly minimal, we expect the spatial variation to be similar to what appeared in the dry experiments: with the bottom row the coolest, and minor differences across a row, with the center of the build bed getting the warmest.

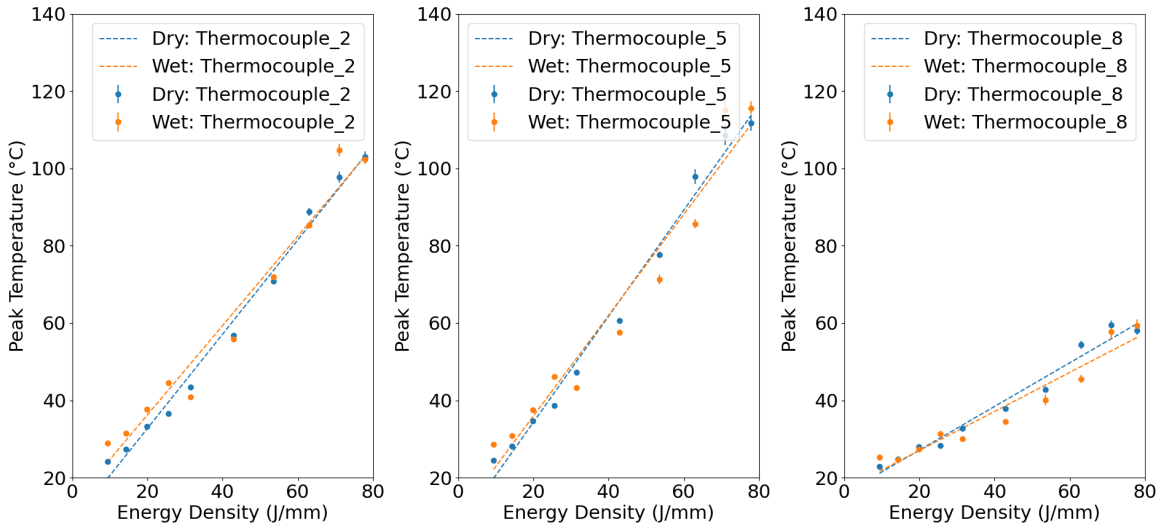


(a) Averaged Peak Temperatures (Thermocouple 4, 5, 6) vs. Linear Energy Density

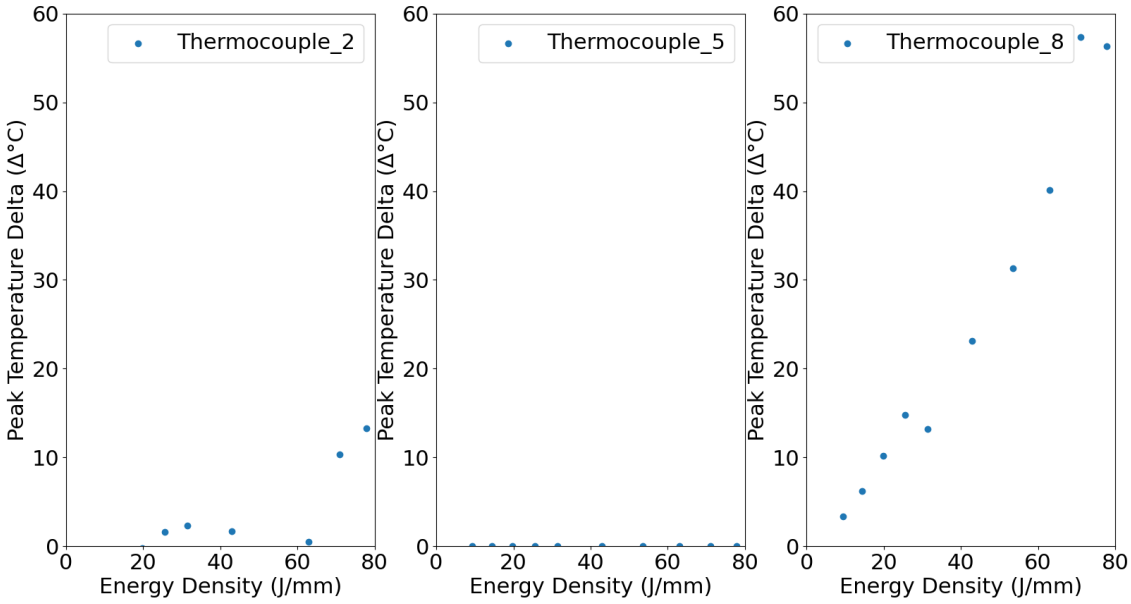


(b) Temperature differences from thermocouple 5. At 80 J/mm, thermocouple 5 reaches an averaged peak temperature about 20°C hotter than thermocouple 4 and about 10°C hotter than thermocouple 6.

Figure 5.41: Averaged Peak Temperatures over the last five layers (Thermocouple 4 to 6) vs. Linear Energy Density.



(a) Averaged Peak Temperatures (Thermocouple 2, 5, 8) vs. Linear Energy Density



(b) Temperature differences from thermocouple 5. At 80 J/mm, thermocouple 5 reaches an averaged peak temperature of about 10°C hotter than thermocouple 2 and over 50°C hotter than thermocouple 8.

Figure 5.42: Averaged Peak Temperatures over the last five layers (Thermocouple 2, 5, 8) vs. Linear Energy Density

There is very little difference in terms of peak temperatures achieved between the printed experiments shown in Figure 5.41 and Figure 5.42, compared to the corresponding dry powder experimental data, as expected.

Generally, the conclusions for peak temperature are the same as they are in the dry bed, with the additional note that the presence of binder does not seem to have affected the peak temperatures obtained after several heating cycles. There are slight differences in the peak temperatures obtained between the dry and printed beds, but the overall relationship between the heater parameters and the peak temperatures are not significantly different.

5.4.3 Analysis - Cooling Rates

There is no clear intuition on the effect of binder on cooling rate - the binder provides additional heat capacity, but may be subject to evaporative cooling. We would like to consider the following research questions:

1. The impact of binder on the peak-to-trough delta at the same distance from the surface - does the binder evaporation provide any cooling effect, or does the additional thermal mass and heat capacity result in a longer hold time at a higher temperature?

2. The effect of depth on peak-to-trough delta - does the presence of binder increase the insulating effect of the powder above the thermocouples?

3. The differences in cooling rate time constants between dry and printed experiments - does the binder increase or decrease the rate at which the temperature drops relative to the peak-to-trough delta?

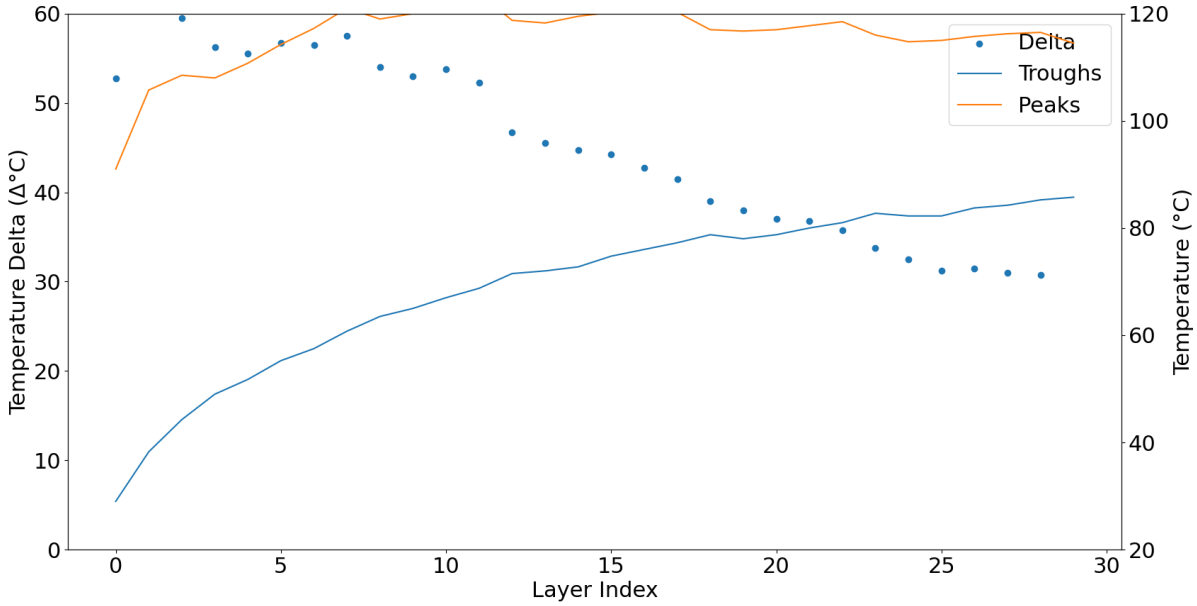


Figure 5.43: Peak-to-Trough Delta, 389 W, 5 mm/s, 79.86 J/mm for thermocouple 5.

In Figure 5.43, both the peak temperatures obtained and the rate at which they are reached are about the same for both dry and printed experiments, with both reaching a maximum of about 120°C within ten layers. The trough temperatures also show a similar trend, reaching about 90°C by the 30th layer of the experiment. The minimal difference is likely due to the evaporation of water - the heater power is high enough that the small amount of remaining binder material does not make a large difference.

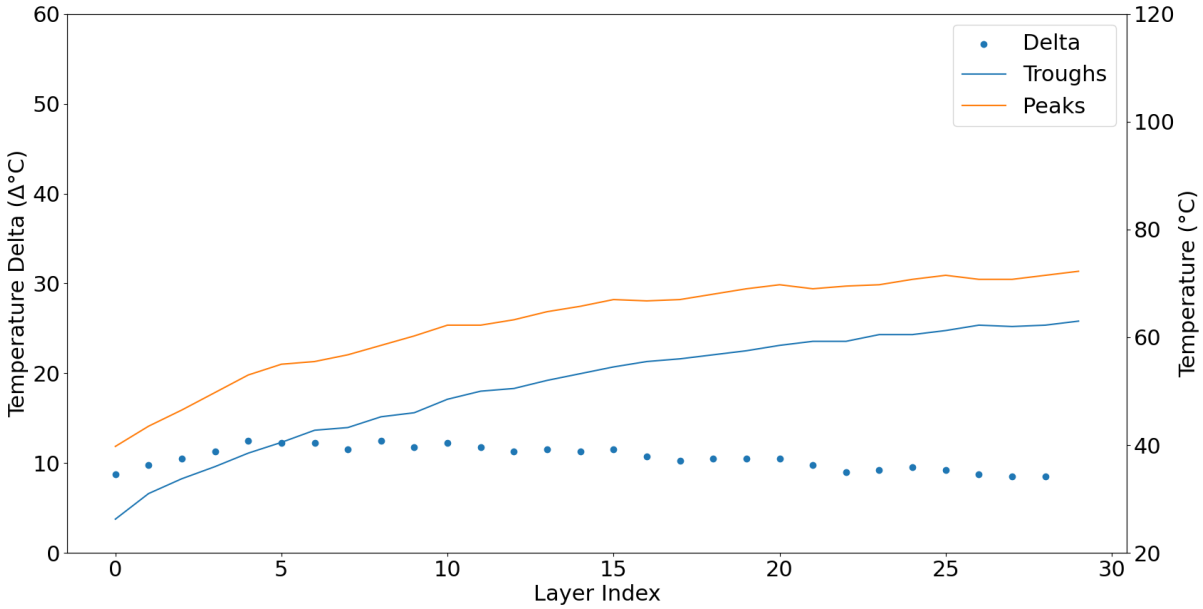


Figure 5.44: Peak-to-Trough Delta, 268 W, 5 mm/s, 53.56 J/mm for thermocouple 5.

At lower heater powers, as in Figure 5.44, the peak temperatures start off lower and take longer to rise. The peak temperature at the 30th layer is close between dry and printed experiments, but the peak temperatures during the early layers are noticeably lower, suggesting that the heat capacity added by the water has a noticeable effect on the initial temperatures of the binder jetting that gradually tapers off as the layers progress.

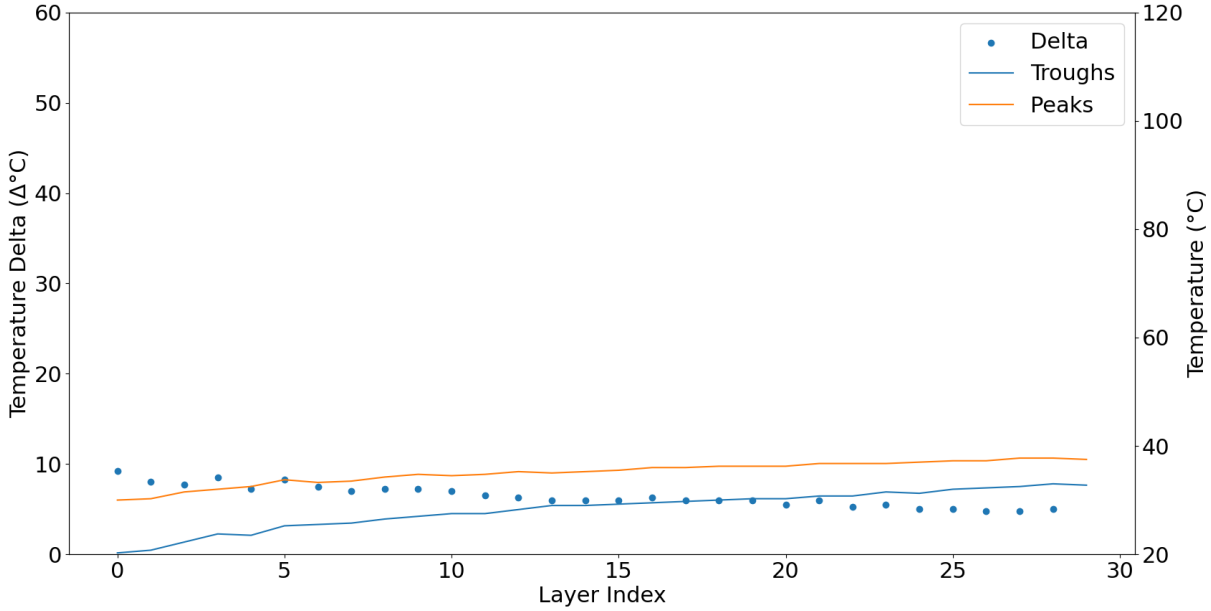


Figure 5.45: Peak-to-Trough Delta, 99 W, 5 mm/s, 19.78 J/mm for thermocouple 5.

In Figure 5.45, during the lowest heater powers, the difference between the peaks and trough temperatures are small, with the temperatures rising slowly.

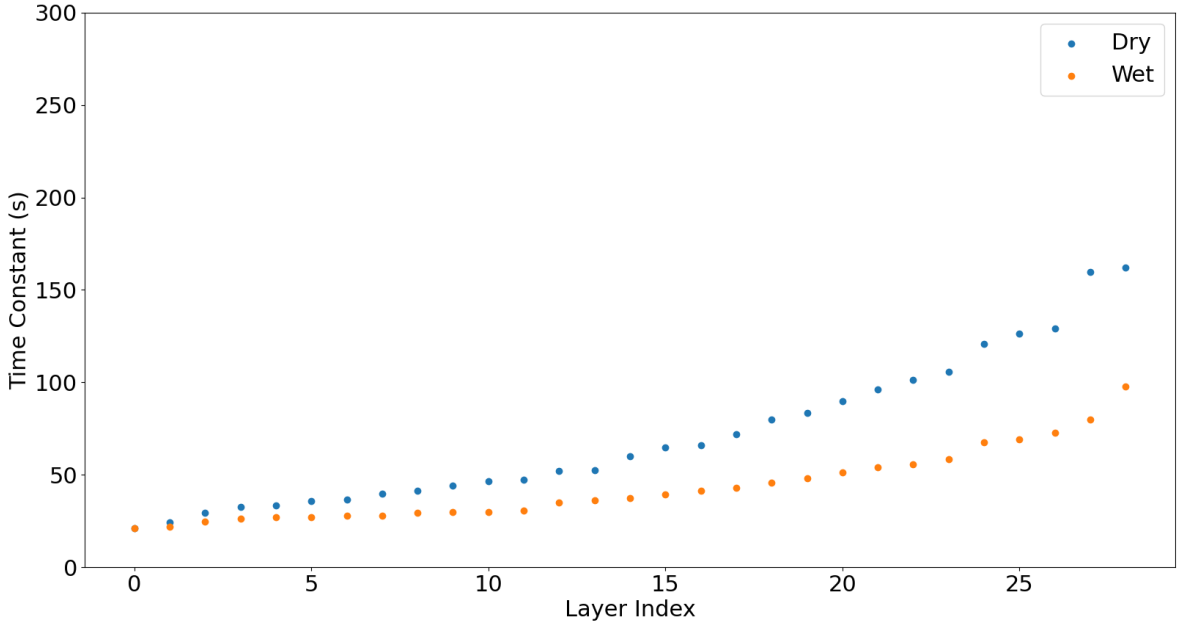


Figure 5.46: Cooling Time Constants, 389 W, 5 mm/s, 79.86 J/mm for thermocouple 5. Dry and printed results are presented for comparison.

Compared to the cooling time constants in dry powder for the same set of heater parameters, the trend in Figure 5.46 has a similar shape (non-linear, with the rate of increase higher as the layer index increases) and a similar starting value at the 0th layer, but with a noticeably lower final value, with $\tau \approx 100$ at the final layer in printed powder, as opposed to $\tau \approx 160$ in dry powder. This indicates that, at the highest heater power, the temperature loss after the peak temperature is more rapid during the latter layers of the bed. Since there should be essentially no water remaining, this result doesn't seem to have a physical explanation other than, potentially, the combined effect of the remaining polymer and powder compaction as a function of droplet impact creating denser layers that can increase heat transfer, as suggested in [1]. On examining the cooling curve fit in Figure 5.47, it looks like there may not be enough samples taken to accurately model the cooling. (As described in Figure 5.3, to make the per-layer times in the dry and printed experiments the same, the printed experiments have a longer period between layers during which no temperature measurements occur.)

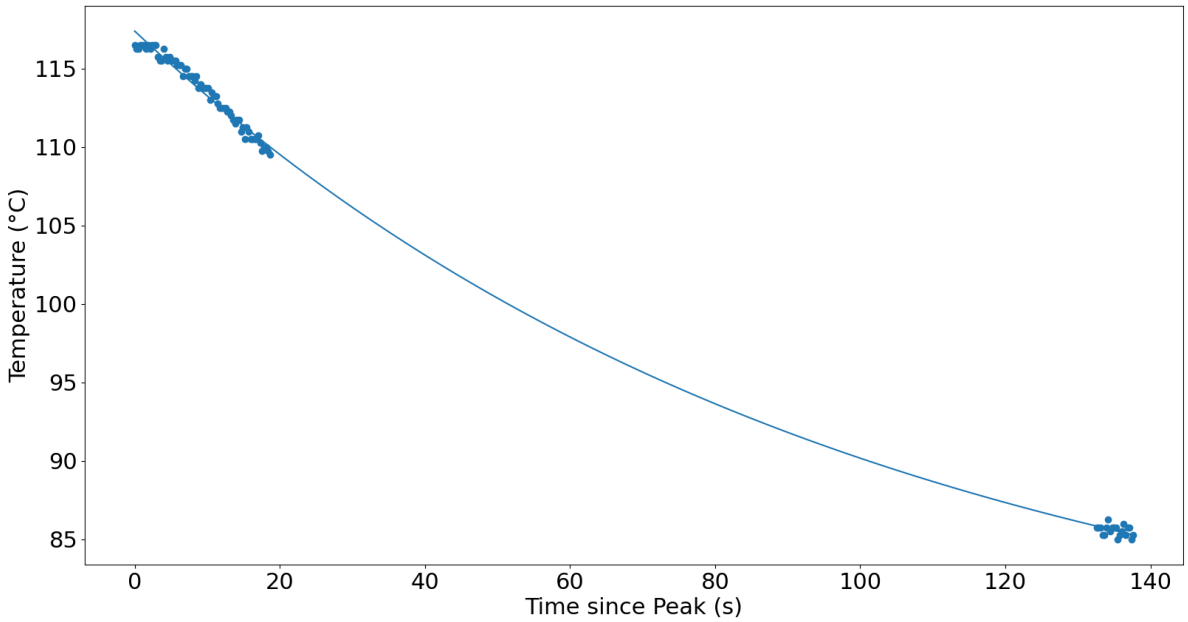


Figure 5.47: 28th Layer Cooling, 389 W, 5 mm/s, 79.86 J/mm for thermocouple 5.

Developing a more reliable software procedure for continuous measurement during the experiment is an avenue for further research, but does mean that an accurate comparison between dry and wet cooling rates is not possible with the data collected here. Overall, the conclusions are:

1. At higher heater powers, the peak-to-trough delta appears to be less affected by the presence of binder, and the overall temperature trend is close to that observed in the dry powder bed. The energy density where this occurs is important to be identified for each powder and binder utilized, as it is indicative that the majority of the liquid has evaporated, thus no further fluid imbibition is occurring, improving geometric fidelity.

2. At lower heater powers, the moderating effect of the binder on temperature is more apparent, and the temperature drop between the highest and lowest temperatures over a layer is smaller. For these ranges of energy density, the thermocouple behaviour is indicative that the samples may not be fully dry, thus fluid imbibition may continue to occur, resulting in potential shape fidelity issues.

3. Due to how the experiments were setup for comparison, an accurate fit for the cooling rate during the wetted experiments is not possible, and would require sampling during the printing and powder spreading periods.

5.5 Analysis - Surface Temperature and Detectable Geometry

The heater acts directly on the surface region of the build bed. Ideally we would like to have a roughly uniform temperature, indicating that the entirety powder bed has been exposed to an equal amount of heat. It has been shown in previous sections that, due to the incomplete heater traversal across the build bed, this is not the case.

The thermal camera captures images of the top surface of the build bed at specific times. For dry experiments, the camera captures occur twice per layer: directly before and directly after heating, as shown in Figure 5.48. For printed experiments, the captures occur three times per layer: once before printing, once after printing (and before heating), and once after heating, as in Figure 5.49.

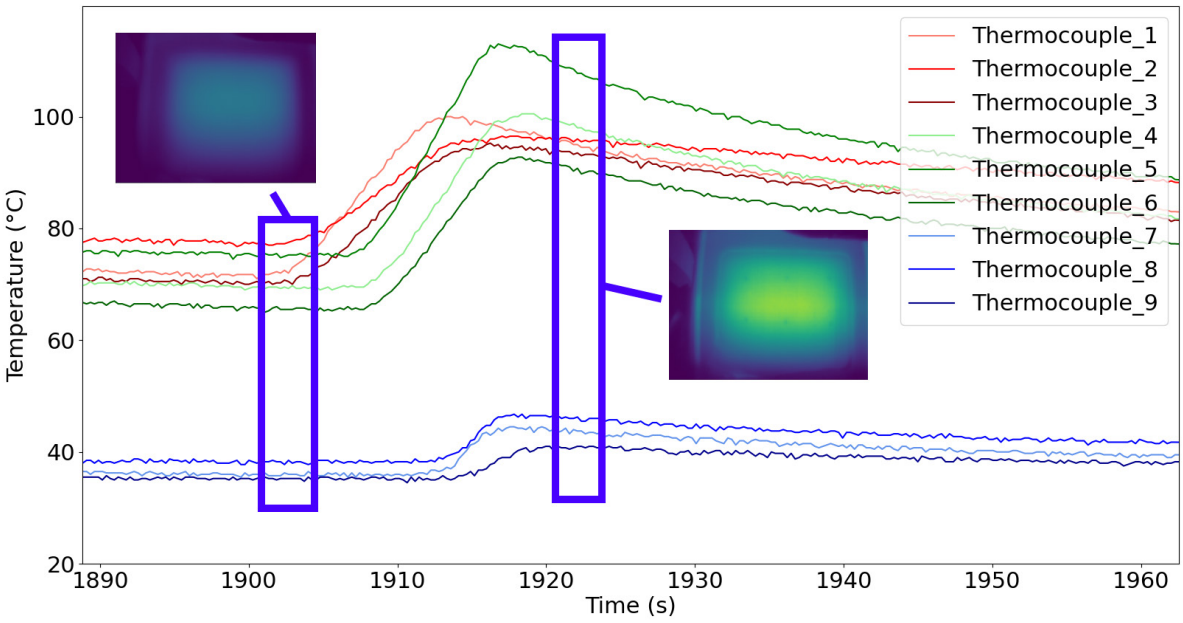


Figure 5.48: Thermal camera imaging overlaid on corresponding thermocouple data, dry powder, taken at a heater power of 349 W and heater speed of 5 mm/s. For each layer, two thermal images are captured: once before heating and once shortly after heating. The thermocouples indicate the temperature below the surface of the powder at a depth of 0.75 mm.

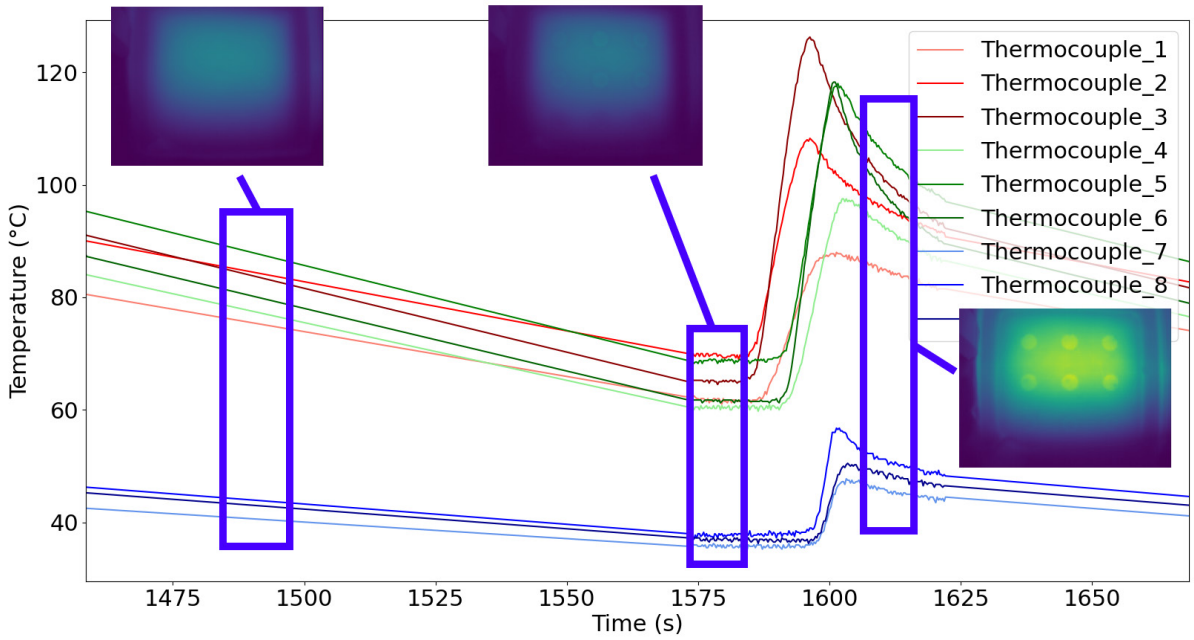


Figure 5.49: Thermal camera imaging overlaid on corresponding thermocouple data, printed powder, taken at a heater power of 349 W and a heater speed of 5 mm/s. For each layer, three thermal images are captured: once before printing, once after printing, and once after heating. The thermocouples indicate the temperature below the surface of the powder at a depth of 0.50 mm.

The thermal imaging sensor can be used to gather information about the temperature of the powder bed, both by itself for measuring the surface temperature, as well as in combination with the thermocouple data for developing a relationship between the surface temperature and temperature at a specific powder depth.

5.5.1 Analysis - Visible Spatial Dependencies based on Vision Data Surface Measurements

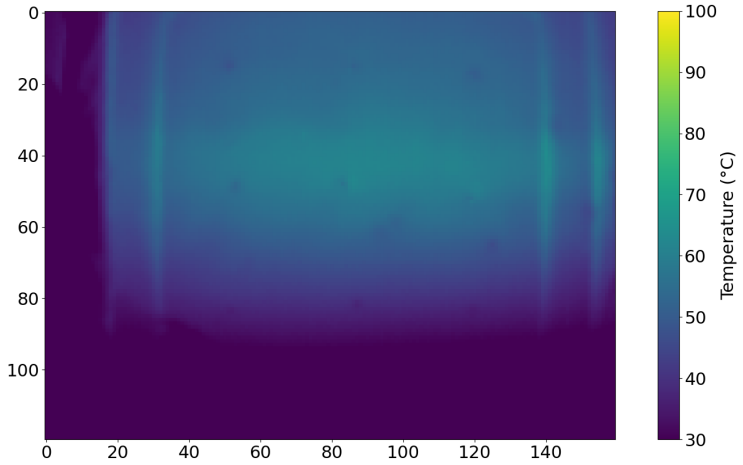
The thermal camera provides spatially-resolved insight into the temperature patterns that form on the surface of the build bed compared to the thermocouple array, where each thermocouple is adept at collecting specific location data at a depth away from the surface. In this section, we would like to examine and ideally quantify the following:

1. The locations of the peak temperatures obtained and their dependence on heater parameters.

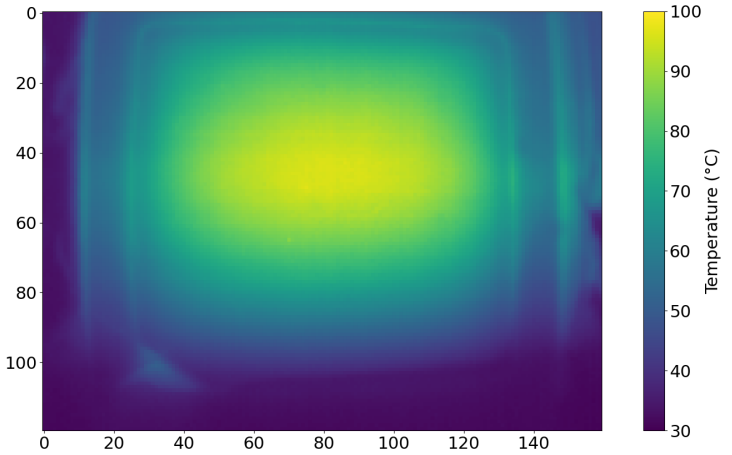
2. The relationship between surface temperature and horizontal and vertical position on the build bed.

Based on the results in previous sections and the general path of the heater and time it spends over the powder bed, the expected location of the peak temperatures is somewhere near the centre of the bed, with the highest temperatures occurring near the centre row. As the imaging occurs a short time after the heater has fully passed over the powder, the top row has been without heat for longer than the centre row, and the bottom row is not fully traversed and receives less heat overall. As an addendum, the ability of the thermal camera to resolve part boundaries within the powder bed is considered in Appendix C.

The thermal camera images will be presented as heat maps, with the corresponding colour bar showing the temperature in Celsius. First, we will examine some thermal images from the dry powder beds at different heater powers.



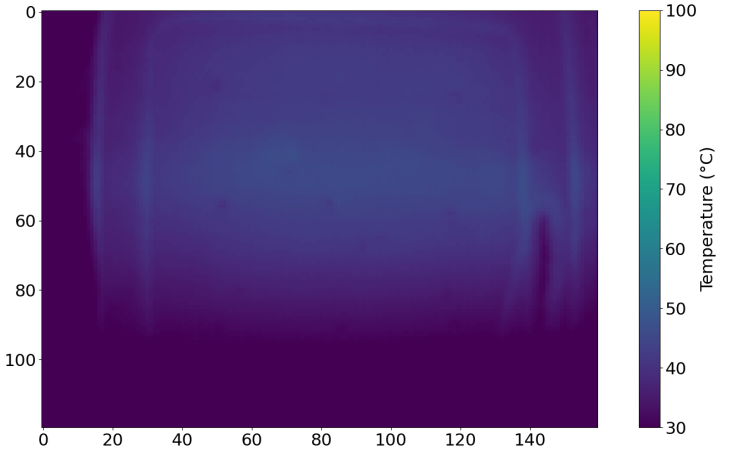
(a) Thermal image after heating, dry powder, 0th layer, 389 W, 5 mm/s, 79.86 J/mm



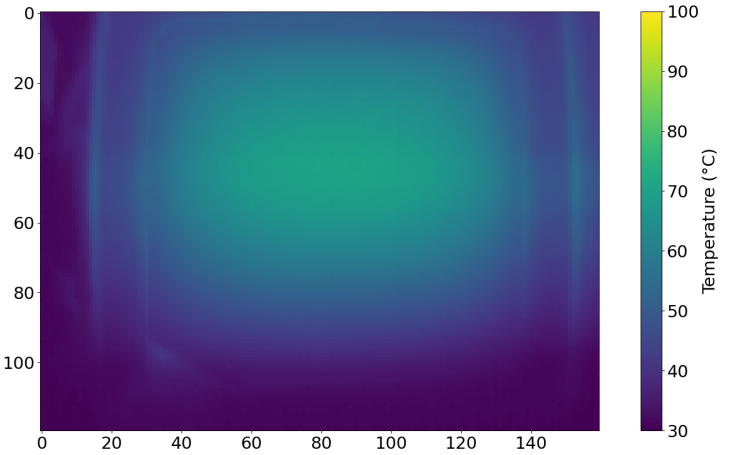
(b) Thermal image after heating, dry powder, 29th layer, 389 W, 5 mm/s, 79.86 J/mm

Figure 5.50: Dry powder after heating, high power, 0th and 29th layers

As can be seen in Figure 5.50, the highest temperatures detected by the thermal camera occur near the centre row, with the temperature dropping off near the edges of the powder bed. Additionally, the powder heats up as the experiment progresses and more layers are added, resulting in higher peak temperatures during the later layers.



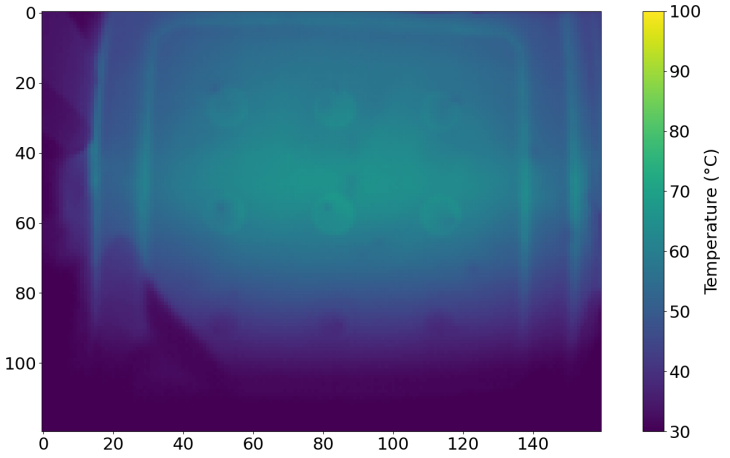
(a) Thermal image after heating, dry powder, 0th layer, 268 W, 5 mm/s, 53.56 J/mm



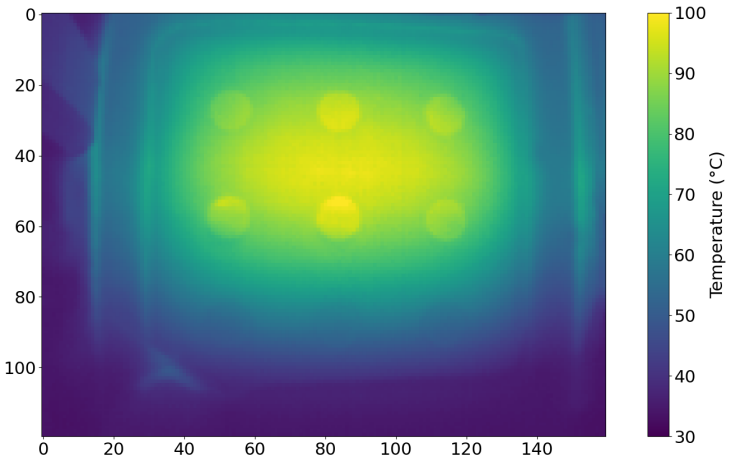
(b) Thermal image after heating, dry powder, 29th layer, 268 W, 5 mm/s, 53.56 J/mm

Figure 5.51: Dry powder after heating, moderate power, 0th and 29th layers

In Figure 5.51, which shows the same locations at lower heater powers, we can see the previously mentioned trends, with the peak temperatures occurring at the same location and the bed heating up with additional layers and repeated heating cycles. Next, we will examine the thermal images from the same heater powers, but with the presence of binder, and compare their temperatures to the corresponding dry powder beds.



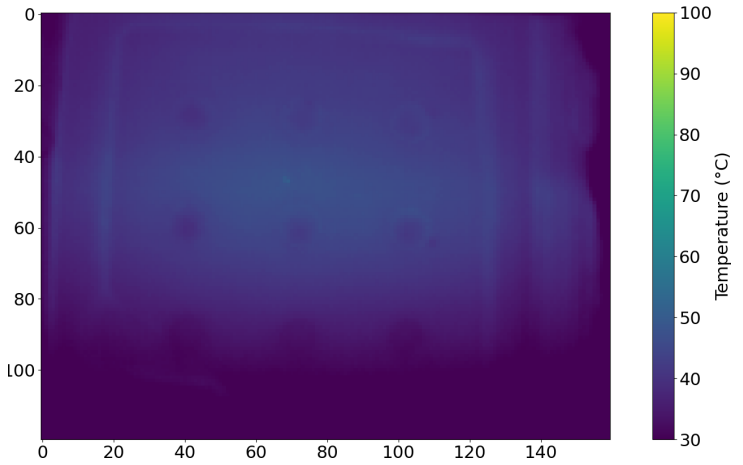
(a) Thermal image after heating, printed powder, 0th layer, 389 W, 5 mm/s, 79.86 J/mm



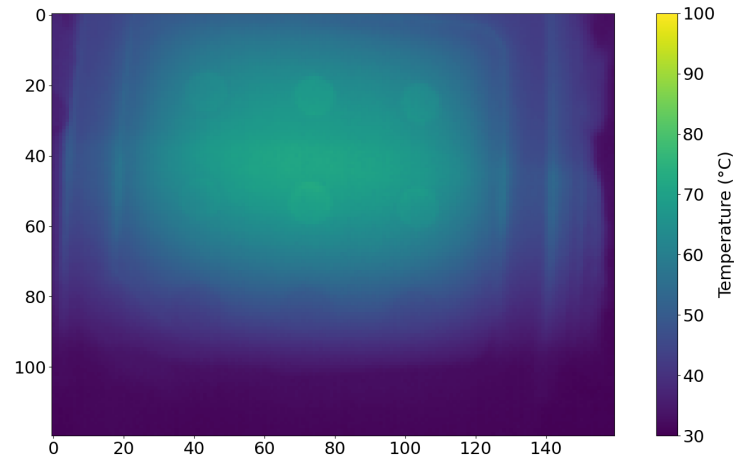
(b) Thermal image after heating, printed powder, 29th layer, 389 W, 5 mm/s, 79.86 J/mm

Figure 5.52: Printed bed after heating, high power, 0th and 29th layers

Figure 5.52 shows the same heater parameters and layers as Figure 5.50, but with the inclusion of binder jetted in an array of circles. Interestingly, the temperatures detected in the bound regions are higher than the surrounding powder, indicating that the binder is either absorbing more heat or conducting less of it to its surroundings.



(a) Thermal image after heating, printed powder, 0th layer, 268 W, 5 mm/s, 53.56 J/mm

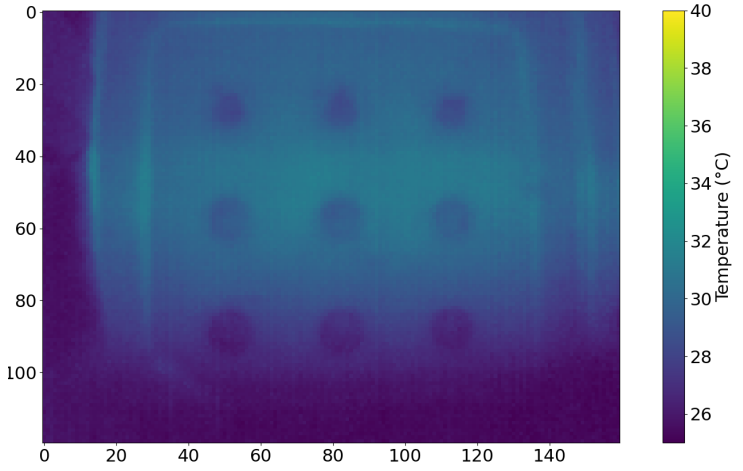


(b) Thermal image after heating, printed powder, 29th layer, 268 W, 5 mm/s, 53.56 J/mm

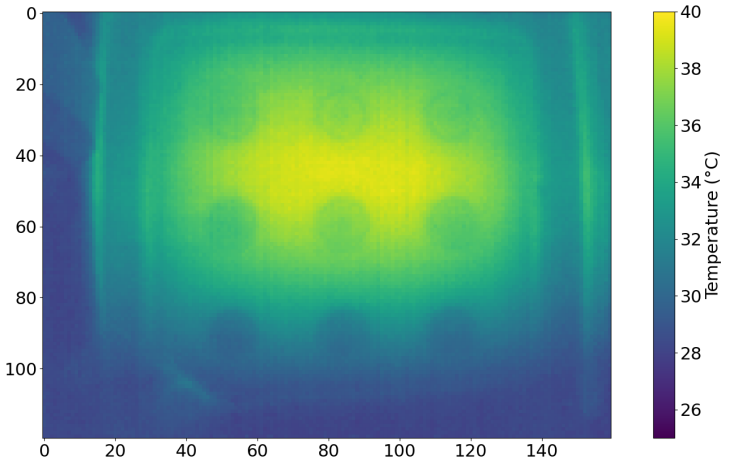
Figure 5.53: Printed bed after heating, moderate power, 0th and 29th layers

In a slight reversal from what was observed at higher heater powers, at lower powers, shown in Figure 5.53, the wetted regions initially appear slightly cooler than the surrounding powder at the initial layer, though this changes over the next few layers. The regions with binder eventually show the same trend of being slightly warmer than the surrounding powder. This is indicative of evaporative cooling from the binder in competition with higher absorptivity due to the wetted regions being darker than the dry powder. These

results seem to be in agreement with the differences between the thermocouple readings between high power and low power trials for the wet experiments.



(a) Thermal image after heating, printed powder, 0th layer, 99 W, 5 mm/s, 19.78 J/mm



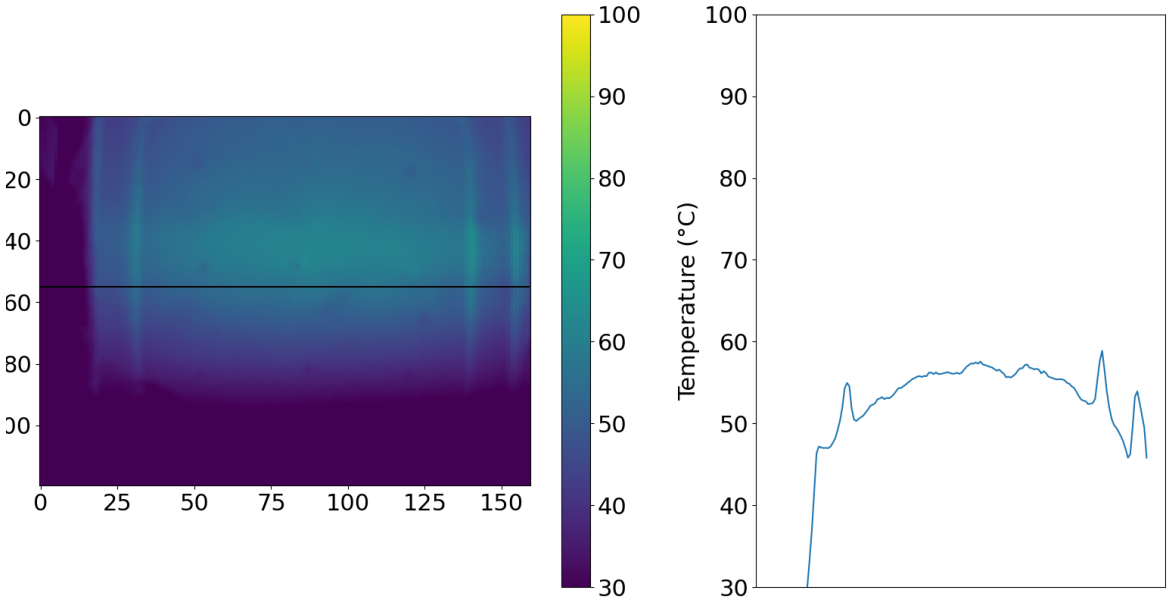
(b) Thermal image after heating, printed powder, 29th layer, 99 W, 5 mm/s, 19.78 J/mm

Figure 5.54: Printed bed after heating, low power, 0th and 29th layers

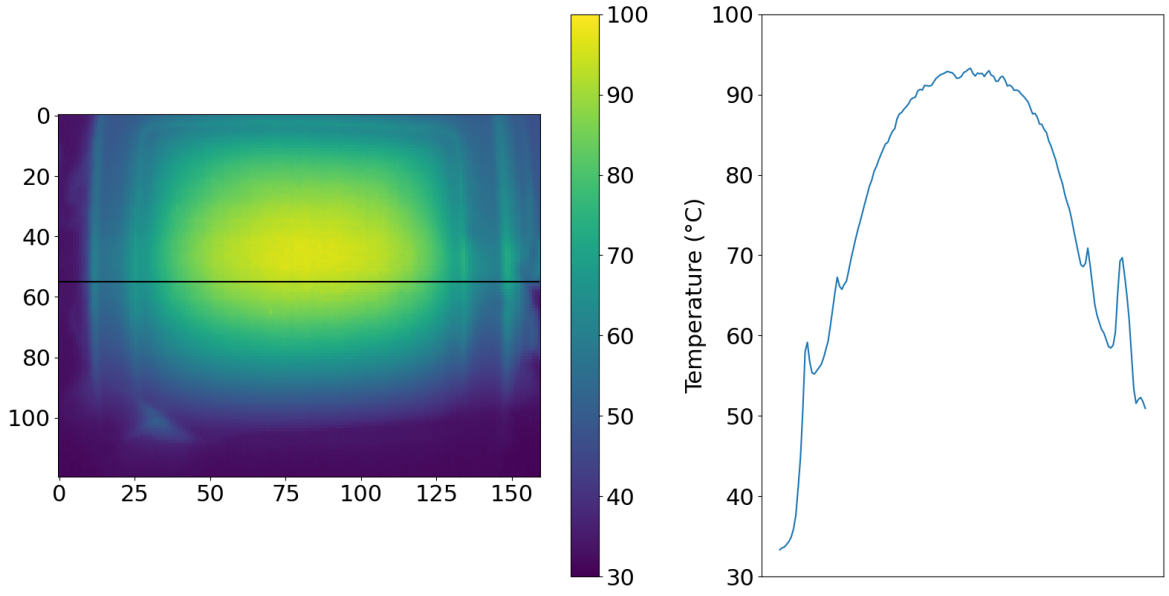
In Figure 5.54, contrary to the higher heater powers, the trend never reverses itself, and (with the exaggerated colour scales shown) we can see than the wetted regions are

always cooler than the surrounding powder. This is indicative of the powder substrate being still substantially wet. The experiments indicate that there are different trends in terms of thermal signatures between high-, medium-, and low-power experiments. This is an important finding, as it demonstrates that a low-cost camera system can be used to indicate thresholds in liquid binder evaporation. Controlling the amount of liquid in the green part through evaporation is an important factor that can contribute to controlling part qualities such as geometric fidelity of parts [4], green part density [25] and green part strength [26]. Further research is required to correlate pixel intensity to liquid saturation and part qualities.

When examining the change in temperature across the bed by using the vision data, one option that can be explored is to consider a single row or column of pixels, and take the change in temperature across that to assess differences in the x and y directions.



(a) Row measurement, dry powder, 0th layer, 389 W, 5 mm/s, 79.86 J/mm



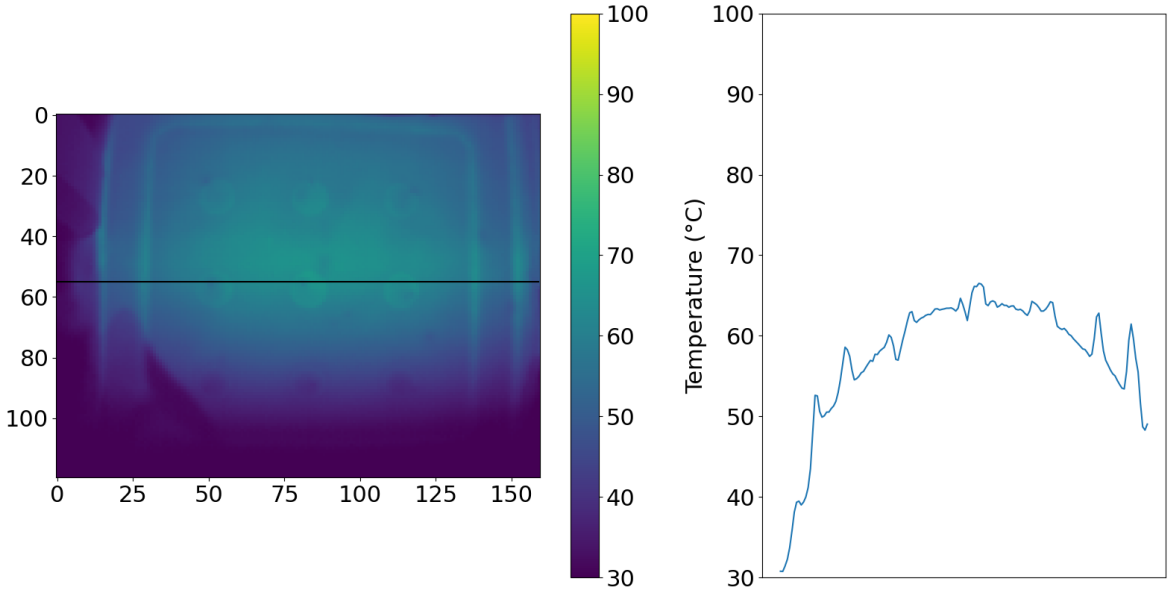
(b) Row measurement, dry powder, 29th layer, 389 W, 5 mm/s, 79.86 J/mm

Figure 5.55: Row measurements of dry powder, high power, 0th and 29th layers

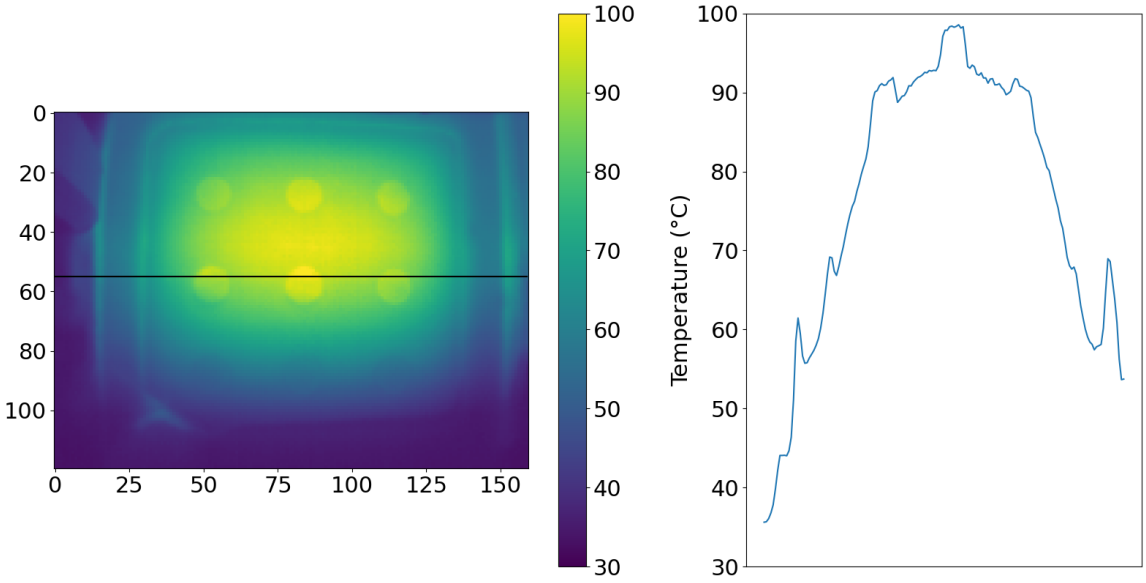
In Figure 5.55a, a horizontal line is drawn across the thermal image, with the corresponding temperature measurements taken and plotted in the right graph. This shows that the peak temperature occurs in the center, and that it is about 5°C to 10°C higher than the outer parts of the powder bed (which are bordered by physical metal walls that show up as small spikes in temperature).

As the experiment progresses, the horizontal temperature trend becomes more extreme. In Figure 5.55b, the peak temperature in the centre of the build bed differs by about 20°C compared to the edges of the bed, resulting in a steeper drop off at the sides of the powder bed. This shows that a low-cost camera system is able to identify regions in the build bed that exhibit more uniform thermal signatures, which would likely correlate to uniform part qualities, as compared to regions in the build bed where the temperature drops significantly. Further studies are necessary to elucidate these relationships.

These results can be contrasted with the images taken at the same points during the corresponding printed experiment.



(a) Row measurement, printed powder, 0th layer, 389 W, 5 mm/s, 79.86 J/mm



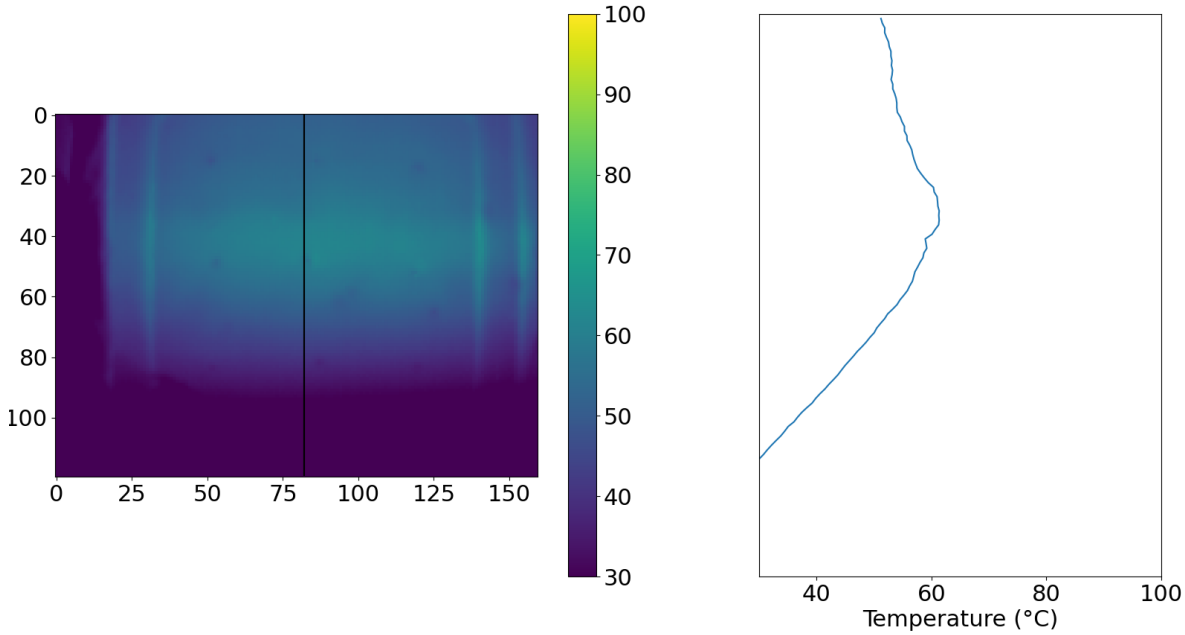
(b) Row measurement, printed powder, 29th layer, 389 W, 5 mm/s, 79.86 J/mm

Figure 5.56: Row measurements of printed bed, high power, 0th and 29th layers

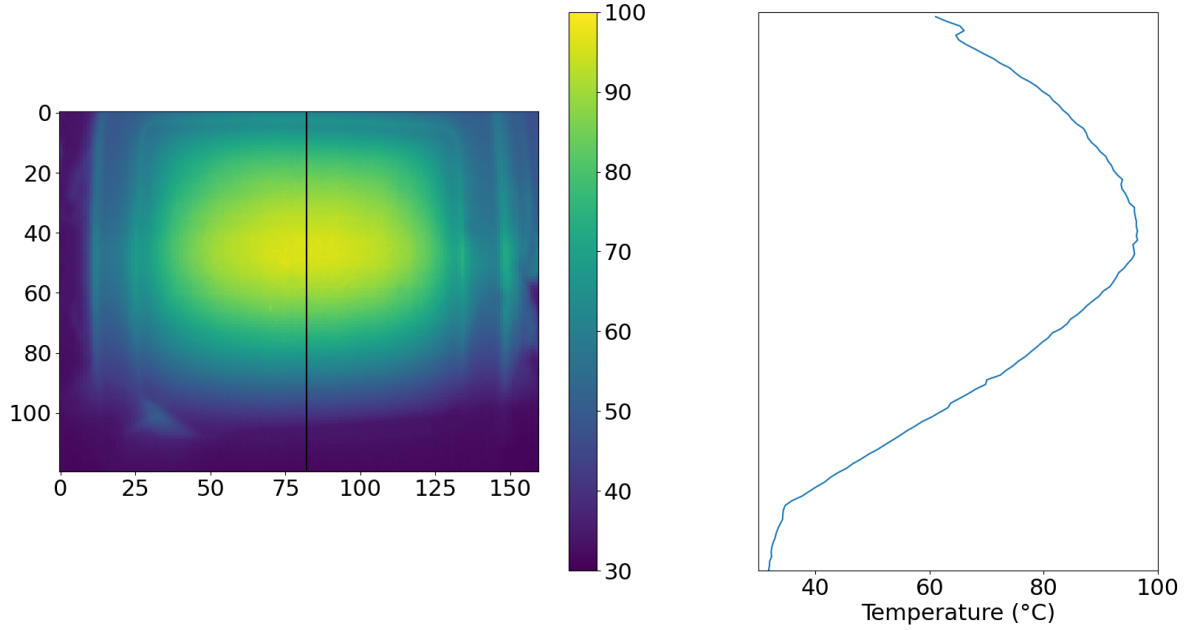
As mentioned earlier in this section, the printed regions of the powder bed visible in Figure 5.56a cause visible disturbances in the temperature profile, compared to the relatively smooth profiles in Figure 5.55.

During the later layers, the printed regions are visible as peaks compared to the surrounding unbound powder, as shown in Figure 5.56b. Interestingly, the absolute temperatures obtained during the final layer seem to be higher overall compared to the dry experiment (a reversal compared to the initial layers), reaching about 100°C compared to just under 90°C observed in the corresponding dry experiment in Figure 5.55b. This seems to be entirely due to the binder and powder compaction phenomena improving the coordination number between particles, as the surrounding powder is the same temperature as it was in the dry experiments.

This same data analysis can be performed in the vertical direction, showing the temperature variation in the direction of heater traversal.



(a) Column measurement, dry powder, 0th layer, 389 W, 5 mm/s, 79.86 J/mm

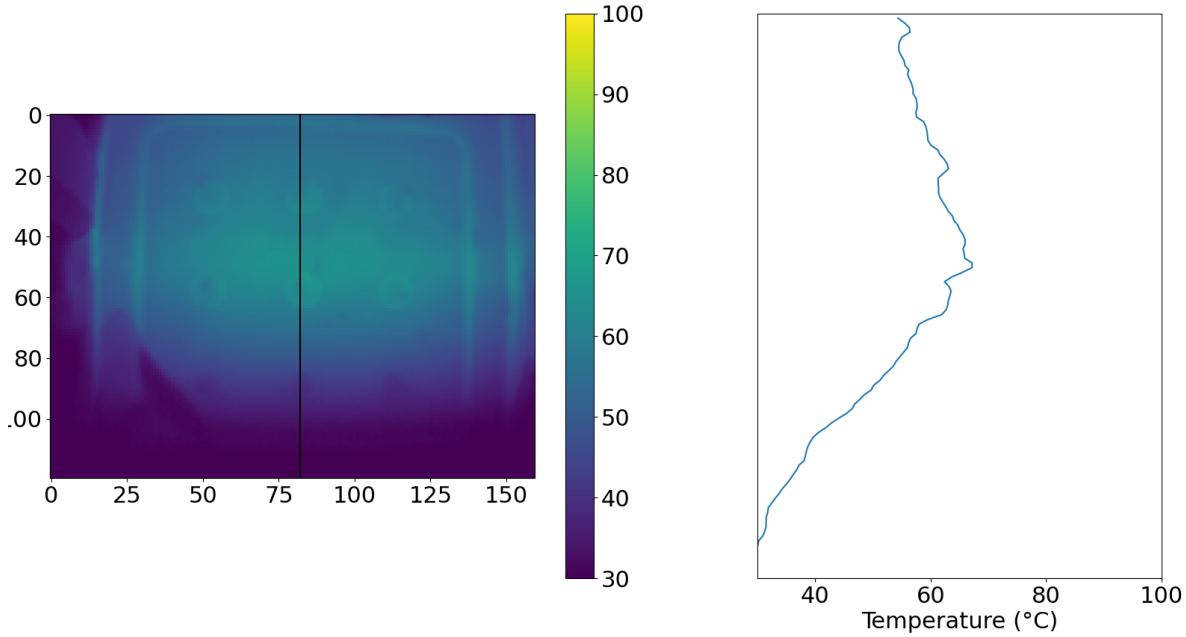


(b) Column measurement, dry powder, 29th layer, 389 W, 5 mm/s, 79.86 J/mm

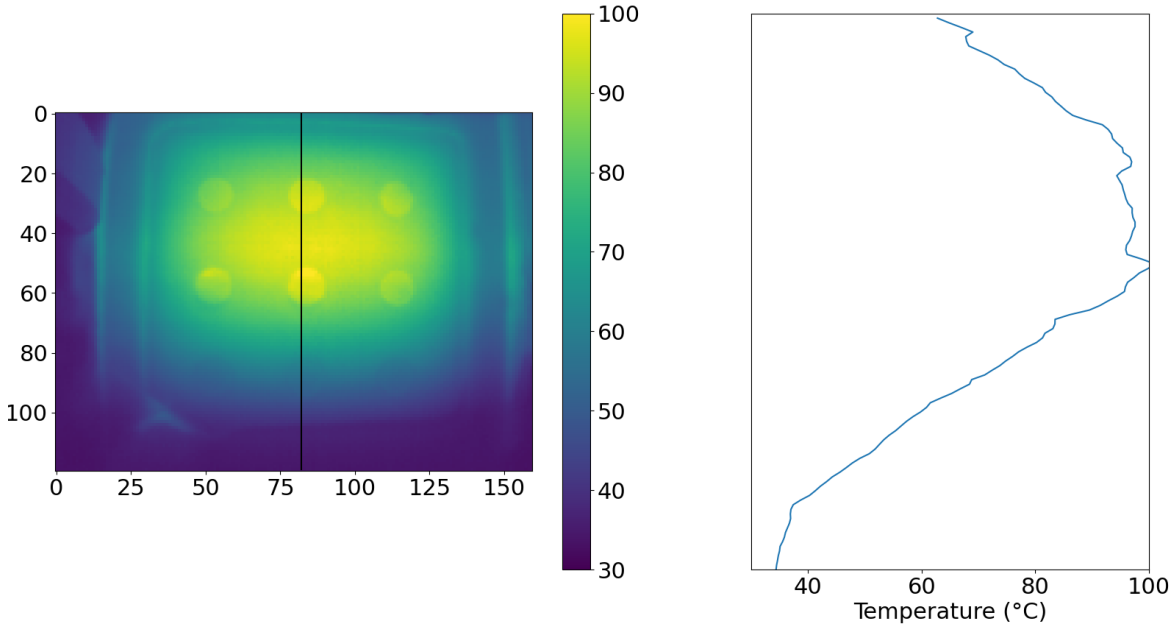
Figure 5.57: Column measurements of dry powder, high power, 0th and 29th layers

In Figure 5.57a, we see a shape similar to the horizontal measurements, where the peak occurs near the centre. In this case, the peak is slightly biased to the top side of the build bed and the lower part of the build bed is much cooler because of the incomplete traversal of the heater. Comparing the top of the build bed to the center, we can see that there is a difference of about 10°C between the two.

As the experiment continues, the overall temperature of the powder bed continues to rise. In Figure 5.57b the difference between the top of the build bed and the centre is about 30°C.



(a) Column measurement, printed powder, 0th layer, 389 W, 5 mm/s, 79.86 J/mm



(b) Column measurement, printed powder, 29th layer, 389 W, 5 mm/s, 79.86 J/mm

Figure 5.58: Column measurements of printed bed, high power, 0th and 29th layers

In Figure 5.58b, the same spike in thermal response in the printed regions can be seen as in Figure 5.56b, with the exception of the lower row, which is too cool to appear on the plot, though it is barely visible in the picture.

In summary,

1. The highest temperatures at the surface occur in the near the centre, being slightly closer to the top of the build bed due to the incomplete traversal of the heater (if the heater was able to fully cover the build bed, we would expect it to occur near dead-centre).

2. The surface temperature during the first heating cycle is significantly cooler than that reached during the later layers.

3. Powder regions with binder have an interesting relationship as a function of power input - at low heater powers and during earlier layers, they are cooler than the surrounding powder, and vice versa for higher heater powers and during later layers. This may be due to the competition between evaporative cooling and increased absorptivity.

4. The centre of the build bed is significantly hotter than the regions closer to the walls. Given that that heater is wide enough to fully cover the build bed, it suggests that the heat loss to the walls is significant.

5.5.2 Analysis - Surface-to-Depth Temperature Deltas

The temperatures measured at the surface of the powder can be compared to corresponding temperature measurements at depth to determine the temperature difference that develops over the course of spreading powder layers. This may give some insight about heat transfer from the surface downwards, as well as what effect the heater continues to have on subsurface powder-binder interactions during indirect heat exposure. The images do not occur frequently enough to form a high-resolution plot of surface-to-depth temperature delta over time, but we can look at point comparisons to observe trends related to:

1. The change in surface temperature with respect to the layer index.

2. The temperature deltas that occur at each of the image capture points, and how they change with heater parameters and depth.

The figures below show the measured temperatures by the thermocouple in the centre of the build bed (displayed by the line plot) and the corresponding temperature at the same location above the thermocouple measured by the thermal camera (displayed as the discrete points), computed as the mean intensity of a five-by-five square of pixels centered on the thermocouple.

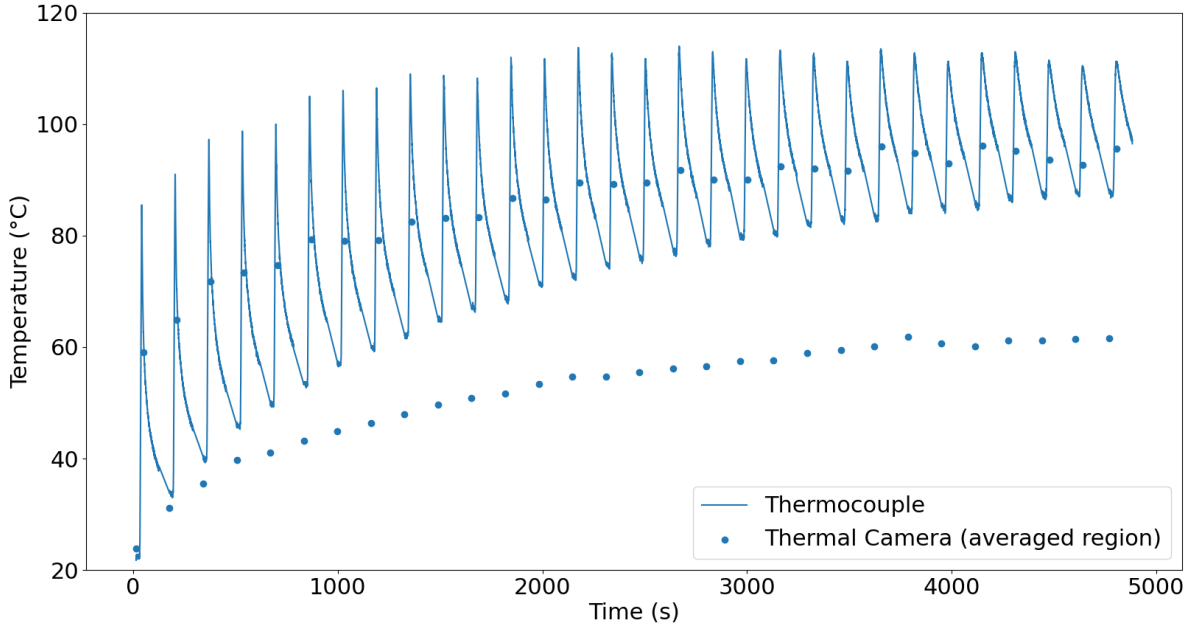


Figure 5.59: Dry Surface-to-Depth Temperature Comparison, 389 W, 5 mm/s, 79.86 J/mm

In Figure 5.59, there is a large deviation between the measured temperatures of the two sensors, with the deviation reaching a maximum of approximately 30°C. While there are some differences expected as the depth increases, the differences are large, which indicates the possibility that at least one of the sensor measurements is incorrect.

Available FLIR camera documentation indicates that low emissivities (below 0.5) can cause measurement problems [16]. The software library being used outputs a converted temperature from its radiometric data using its own model for converting raw spectral radiance counts to temperature [31]. Some consideration on this conversion is noted in Appendix D.

Figure 5.60 shows the same heater parameters for the wetted experiment, with similar outcomes.

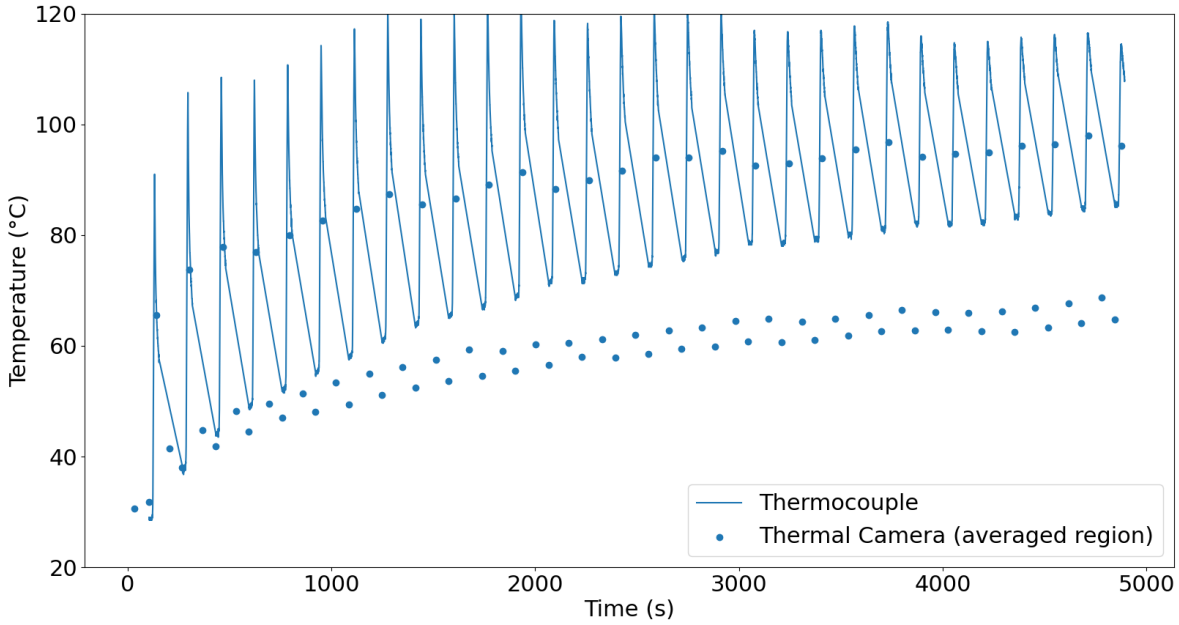


Figure 5.60: Printed Surface-to-Depth Temperature Comparison, 389 W, 5 mm/s, 79.86 J/mm

In Figure 5.60, the measured temperatures between the two sensors are closer together, with the difference increasing as the layers increase and more powder is added between the surface and thermocouple. It is hypothesized that the insulating layer of powder results in less radiant heat loss, resulting in the temperature at depth being higher than the temperature at the surface, at least at the points measured. The smaller difference in temperatures between the two sensors compared to Figure 5.59 may be due to the emissivity of the wetted powder substrate being higher that the dry powder.

Regarding the measurement of temperatures in powder beds in general, non-contact methods such as thermal cameras are subject to non-constant emissivity and dependence on surface conditions, leading to potentially large discrepancies in measured temperature. A suggested guideline is that these tools be used only as qualitative measurements to compare "hotter" and "colder" regions in an image [30, 33]. Contact methods, like thermocouples, can potentially introduce temperature measurement errors in powder bed measurements due to differences in conductivity and emissivity compared to the bulk powder, hypothesised as being more significant near the surface of powder beds due to incident radiation from heaters directly on their junctions [12].

On the specific hardware, software, and materials used in this work, the thermal camera

(Lepton 3.5, FLIR), is a long-wave infrared camera with its high-gain mode operating between -10 °C to 140 °C, and a low-gain mode operating between -10 °C to +400 °C [15]. The documentation of flirpy indicates two corrections made to the raw data - a linear correction to account for sensor temperature and a fit to the Planck equation for spectral radiance to convert to temperature, with a note that the primary cause of uncertainty is likely the object emissivity [32], a property with a complex dependence on temperature and wavelength [12]. FLIR notes that for emissivities less than 0.5, it is expected that accurate temperature measurements are unlikely [16], with the measured emissivity of stainless steel powders in the long-wave infrared region (wavelengths greater than 8 µm) reported as being around 0.5 or less [12, 24].

Lastly, the measured temperatures of the thermal camera, as seen in Figure 5.59, appear to be deviating from the thermocouple measurement more as the powder depth increases. An alternate hypothesis, or potential contributing factor, is that under these conditions, the net effect of the insulating powder layer is keeping heat in, whereas the exposed surface is losing heat more rapidly by comparison. The low conductivity of of metal powders can result in the development of large surface-to-depth deltas [12].

5.6 Dimensional Dependencies

In binder jetting, due to migration of the binder through the powder, where the binder spreads outward from its initial location (like water through sand), the green part geometry tends to be larger than its printed design. This results in parts being slightly larger than the designed part would suggest, and results in internal holes being smaller than designed.

In principle, the action of the heater would serve to modify the migration behaviour due to evaporating the water, which increases the binder viscosity and decreases its volume. From this, we might intuit that increasing heater power would decrease the amount of binder migration and thus increase the accuracy of the printed part, assuming that no heating-related defects like warping occur.

We can check for any clear trends in geometric accuracy vs. heater parameters by selecting the circular artifacts printed in previous sections, and plotting their diameter against the heater powers used to produce them. In this case, a Keyence VHX7000 microscope was used to image the samples, and the Keyence software analysis suite was used to estimate their diameter (i.e. three points on their circumference were manually selected on the captured image, and the calculated diameter was recorded).

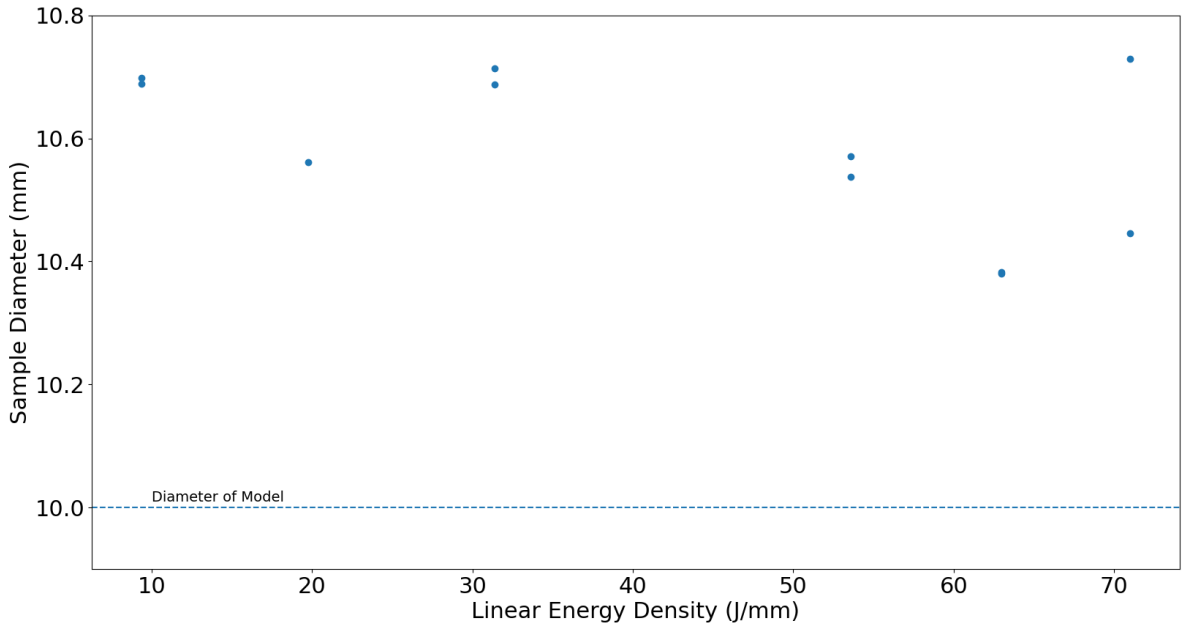


Figure 5.61: Sample Diameters vs. Linear Energy Density

From Figure 5.61, we see that the measured geometries are greater than the designed model geometry, as expected, and that there does not appear to be a strong trend. If the data point in the upper right is rejected (as a potential outlier), then there does appear to be a slight decrease in diameter as heater power increases, which corresponds to an increase in accuracy. Another point of note is that the samples exposed to the same heater power are clustered closely together, which indicates the possibility of other factors other than heater power affecting the final result. Lastly, due to the differences in heater exposure across the powder bed, it is possible that samples under the same set of heater parameters were exposed to significantly higher or lower amounts of energy. Accurately determining a trend in sample diameter would require more data, ideally with the parts held closer together to avoid spatial variations in powder temperature. The inclusion of weight data to assess mass in addition to geometric profile would also assist in assessing geometric fidelity.

Chapter 6

Conclusions and Future Work

6.1 Conclusions

In this work, the development of an open-architecture binder jetting machine is described, as well as experimentation gathering temperature data in 316L powder. The open-architecture nature of the system gives it a degree of procedural and experimental flexibility that exceeds other binder jetting machines, and the temperature measurements performed demonstrate practicality as well as providing insight into powder-binder phenomena that have implications for outcomes in binder jetting. The technical description details the modules and peripherals required for carrying out the printing steps of binder jetting as well as its current capabilities and some technical considerations for its use and future development.

The temperature experimentation of the powder bed provides some predictive results for assessing the temperature as a function of heater parameters, and contrasts differences between dry and printed 316L powder. Some notable results are that the powder provides strong insulation regarding heating rate (dropping to less than half its initial heating rate under 1.5 mm of powder), the peak temperatures achieved have a linear relationship with the heater power (within the ranges tested), and that the evaporative cooling of the binder appears to have varying levels of significance on the temperature depending on the heater power, causing the heating rate to remain below 2°C/s, up to the point where all the binder is evaporated. Lastly, the thermal camera is capable of resolving many details at the surface of the powder bed, and indicates temperature differences across the bed in excess of 10°C, but is not able to be easily synthesized with the thermocouple data in this work.

6.2 Future Work

The topics mentioned in this chapter are of interest in creating more robust thermal models in powder beds and binder jetting, or are directly related to green part quality and sintering outcomes. The focus in these sections will be on how these research areas may be advanced in the future, either with a similar experimental setup or through other research and development methods.

Some of these research packages are extensions to the heater work and testing performed in the previous chapter, and may be performed through additional programming and hardware enhancement of the bespoke binder jetting system described in this paper, while others may need additional equipment support.

6.2.1 Latency of Heater Impact

The latency of heater impact is the time between application of heat and the response at the temperature sensor, and is an expansion of the observations and analysis performed on the heating rate and peak temperatures as a function of depth. The significance of this is quantifying the "reach" of the heater through thicker layers of powders for use in process optimization (applying heat every few layers as opposed to every layer) as well as developing a transient heat conduction model for fine grained control of the bulk powder.

Effectively developing a model from experimental data requires testing multiple depths simultaneously - at minimum, collecting temperature data at both the surface and some distance under the surface would be needed. This type of data collection is not possible with the current sensor setup, as the thermocouples are located at the same height and the thermal camera cannot record the build bed when the heater is over it.

6.2.2 Defect Detection and Geometric Fidelity

Defect detection and geometric fidelity covers deviations from the designed part that occur during the binder jetting process. Examining the image data on a per-layer basis may allow identification of issues that occur during powder spreading and printing, both of which are error-prone and can cause a build-up of issues that significantly reduce the engineering properties of the green part and thus the sintered, final part.

Edge detection testing with the thermal camera was conducted in a prior chapter - here, we would consider the capabilities of currently available and future vision systems

and their ability to resolve features and detect defects in-situ to provide useful feedback and status updates during the printing process.

6.2.3 Green Part Strength

The green parts produced immediately after binder jetting are typically not very strong, and must undergo a "depowdering" step that removes loose powder from the green part. Generally, loose powder does not entirely fall away from parts, particularly if they have complex geometry that powder can get stuck in, and current depowdering techniques are highly manual and involve careful brushing and shifting of the part to dislodge powder. This physical manipulation can damage or break off fine features and sharp angles. Heating modifies the binder composition and chemistry, and quantifying the compressive and shear strength as changed by heating is a way to improve green part yields and allow more feature sizes and types to be binder jetted.

Designing a standard part for load testing and printing it under different heating conditions will produce the test samples required. Due to the temperature differences on the bed, printing them within a fixed region (or altering the heater traversal to more evenly heat the feed bed) will ensure that the parts actually receive comparable amounts of heat.

6.2.4 Multi-Material Printing and Localization

For various engineering purposes, it may be valuable to use multiple materials within the same part, in order to perform localized modification of its properties. Precise application of material is difficult and requires specialized manufacturing hardware, increasing production time and cost. We would like to assess the technical feasibility of using the bespoke binder jetting machine and available hardware to apply metallic reinforcement to particular regions using solutionized or suspension-based metallic inks, in which metal particles are combined with a solvent.

Specifically, MSAM is performing research with a copper nano-ink suspension, where nanoparticles are suspended in an aqueous solvent. The addition of this ink at specific locations within parts is believed to have an effect on the strength and sintering behaviour during heat treatment.

References

[1] Usman Ali, Yahya Mahmoodkhani, Shahriar Imani Shahabad, Reza Esmaeilizadeh, Farzad Liravi, Esmat Sheydaeian, Ke Yin Huang, Ehsan Marzbanrad, Mihaela Vlasea, and Ehsan Toyserkani. On the measurement of relative powder-bed compaction density in powder-bed additive manufacturing processes. *Materials & Design*, 155:495–501, October 2018.

[2] Oraib Alketan and Rashid Abu Al-Rub. MSLattice: A free software for generating uniform and graded lattices based on triply periodic minimal surfaces. *Material Design & Processing Communications*, 3, October 2020.

[3] Shing-Yun Chang, Jun Jin, Jun Yan, Xin Dong, Bodhisattwa Chaudhuri, Karthik Nagapudi, and Anson W. K. Ma. Development of a pilot-scale HuskyJet binder jet 3D printer for additive manufacturing of pharmaceutical tablets. *International Journal of Pharmaceutics*, 605:120791, August 2021.

[4] Han Chen and Yaoyao Fiona Zhao. Process parameters optimization for improving surface quality and manufacturing accuracy of binder jetting additive manufacturing process. *Rapid Prototyping Journal*, 22(3):527–538, January 2016. Publisher: Emerald Group Publishing Limited.

[5] Xuejun Chen, Shanshan Wang, Jie Wu, Shuwei Duan, Xiaolong Wang, Xiaoxuan Hong, Xiaolu Han, Conghui Li, Dongzhou Kang, Zengming Wang, and Aiping Zheng. The Application and Challenge of Binder Jet 3D Printing Technology in Pharmaceutical Manufacturing. *Pharmaceutics*, 14(12):2589, November 2022.

[6] Thomas Cheny, Christophe Colin, and Benoit Verquin. Experimental evaluation of binder infiltration depth and axial overlap to control properties of green parts produced by Binder Jetting. *Additive Manufacturing*, 87:104231, May 2024.

[7] Sohini Chowdhury, N. Yadaiah, Chander Prakash, Seeram Ramakrishna, Saurav Dixit, Lovi Raj Gupta, and Dharam Buddhi. Laser powder bed fusion: a state-of-the-art review of the technology, materials, properties & defects, and numerical modelling. *Journal of Materials Research and Technology*, 20:2109–2172, September 2022.

[8] Nathan B. Crane. Impact of part thickness and drying conditions on saturation limits in binder jet additive manufacturing. *Additive Manufacturing*, 33:101127, May 2020.

[9] Yvo de Haas. Oasis 3DP – Ytec 3D.

[10] Yvo de Haas. Plan B – Ytec 3D.

[11] Truong Do, Patrick Kwon, and Chang Seop Shin. Process development toward full-density stainless steel parts with binder jetting printing. *International Journal of Machine Tools and Manufacture*, 121:50–60, October 2017.

[12] Martin Dressler, M. Röllig, M. Schmidt, Alessandro Maturilli, and J. Helbert. Temperature distribution in powder beds during 3D printing. *Rapid Prototyping Journal*, 16:328–336, August 2010.

[13] Wenchao Du, Xiaorui Ren, Zhijian Pei, and Chao Ma. Ceramic Binder Jetting Additive Manufacturing: A Literature Review on Density. *Journal of Manufacturing Science and Engineering*, 142(040801), February 2020.

[14] Amy Elliott and Tomonori Saito. Advances in Binder Jet Additive Manufacturing. Technical Report ORNL/TM–2023/2829, 1989567, NFE-17-06670, Oak Ridge National Lab. (ORNL), Oak Ridge, TN (United States), July 2023.

[15] FLIR. Lepton LWIR Micro Thermal Camera Module | Teledyne FLIR.

[16] FLIR. How Does Emissivity Affect Thermal Imaging?, 2021.

[17] Fujifilm. StarFire® SG1024/MA | Fujifilm [United States].

[18] Stephanie Hendrixson. How Do Binder Jetting and Multi-Laser Powder Bed Fusion Match Up?, July 2024.

[19] Nancy Huang, Olivia J. Cook, Andrea P. Argüelles, and Allison M. Beese. Review of Process–Structure–Property Relationships in Metals Fabricated Using Binder Jet Additive Manufacturing. *Metallography, Microstructure, and Analysis*, 12(6):883–905, December 2023.

[20] Jacob Lawrence, Hector Andres Peña Vega, Bryant Stegman, Caleb Roberts, Joseph Spencer, Clinton James, McKay Christensen, and Nathan Crane. Construction of Open-Source Laboratory-Scale Binder Jetting System for High-Speed Synchrotron X-Ray Imaging. *2022 International Solid Freeform Fabrication Symposium*, October 2022.

[21] Maja Lehmann, Cara G. Kolb, Flavia Klinger, and Michael F. Zaeh. Preparation, characterization, and monitoring of an aqueous graphite ink for use in binder jetting. *Materials & Design*, 207:109871, September 2021.

[22] Saereh Mirzababaei and Somayeh Pasebani. A Review on Binder Jet Additive Manufacturing of 316L Stainless Steel. *Journal of Manufacturing and Materials Processing*, 3(3):82, September 2019. Number: 3 Publisher: Multidisciplinary Digital Publishing Institute.

[23] Hadi Miyanaji, Shanshan Zhang, Austin Lassell, Amirali Zandinejad, and Li Yang. Process Development of Porcelain Ceramic Material with Binder Jetting Process for Dental Applications. *JOM*, 68(3):831–841, March 2016.

[24] Gunther Mohr, Susanna Nowakowski, Simon J. Altenburg, Christiane Maierhofer, and Kai Hilgenberg. Experimental Determination of the Emissivity of Powder Layers and Bulk Material in Laser Powder Bed Fusion Using Infrared Thermography and Thermocouples. *Metals*, 10(11):1546, November 2020. Number: 11 Publisher: Multidisciplinary Digital Publishing Institute.

[25] Amir Mostafaei, Pierangeli Rodriguez De Vecchis, Katerina A. Kimes, Drew Elhassid, and Markus Chmielus. Effect of binder saturation and drying time on microstructure and resulting properties of sinter-HIP binder-jet 3D-printed WC-Co composites. *Additive Manufacturing*, 46:102128, October 2021.

[26] Amir Mostafaei, Amy M. Elliott, John E. Barnes, Fangzhou Li, Wenda Tan, Corson L. Cramer, Peeyush Nandwana, and Markus Chmielus. Binder jet 3D printing—Process parameters, materials, properties, modeling, and challenges. *Progress in Materials Science*, 119:100707, June 2021.

[27] Daniel Oropeza and A. John Hart. A laboratory-scale binder jet additive manufacturing testbed for process exploration and material development. *The International journal, advanced manufacturing technology*, 114:3459–3473, June 2021.

[28] E. Persembe, C. Parra-Cabrera, C. Clasen, and R. Ameloot. Binder-jetting 3D printer capable of voxel-based control over deposited ink volume, adaptive layer thickness,

and selective multi-pass printing. *Review of Scientific Instruments*, 92(12):125106, December 2021.

[29] Prusa Research. PrusaSlicer | Original Prusa 3D printers directly from Josef Prusa.

[30] Emmanuel Rodriguez, Jorge Mireles, Cesar A. Terrazas, David Espalin, Mireya A. Perez, and Ryan B. Wicker. Approximation of absolute surface temperature measurements of powder bed fusion additive manufacturing technology using *in situ* infrared thermography. *Additive Manufacturing*, 5:31–39, January 2015.

[31] Josh Veitch-Michaelis. Thermal cameras — flirpy documentation.

[32] Josh Veitch-Michaelis, Aglinn, and Alyetama. LJMUAstroecology/flirpy: Version 0.3.0, November 2021.

[33] Alexandra M. Vest, David R. St-Pierre, Stephen Rock, Antoinette M. Maniatty, Daniel J. Lewis, and Samuel J. A. Hocker. Thermocouple Temperature Measurements in Selective Laser Melting Additive Manufacturing. Technical report, NASA, March 2022. NTRS Author Affiliations: Rensselaer Polytechnic Institute, Langley Research Center NTRS Document ID: 20220002988 NTRS Research Center: Langley Research Center (LaRC).

[34] Lien Chin Wei, Lili E. Ehrlich, Matthew J. Powell-Palm, Colt Montgomery, Jack Beuth, and Jonathan A. Malen. Thermal conductivity of metal powders for powder bed additive manufacturing. *Additive Manufacturing*, 21:201–208, May 2018.

[35] Emily M. Wilts, Da Ma, Yun Bai, Christopher B. Williams, and Timothy E. Long. Comparison of Linear and 4-Arm Star Poly(vinyl pyrrolidone) for Aqueous Binder Jetting Additive Manufacturing of Personalized Dosage Tablets. *ACS Applied Materials & Interfaces*, 11(27):23938–23947, July 2019. Publisher: American Chemical Society.

[36] Mohsen Ziaee and Nathan B. Crane. Binder jetting: A review of process, materials, and methods. *Additive Manufacturing*, 28:781–801, August 2019.

APPENDICES

Appendix A

LinuxCNC Configuration

A.1 LinuxCNC INI File

```
# This is the INI file for the bespoke binder jetting machine in the
↪  Multi-
# Scale Additive Manufacturing (MSAM) Laboratory at the University of
↪  Waterloo.
# CONTRIBUTION HISTORY
# Matthew Chai: Sept 2019 to April 2020
## Initial configuration
# Matthew Chai: July 2020 to Ongoing
## Minimum features required for basic functionality
## Removed Z1/A axis to make space for Fuji printhead module
## Added Z1 back in to account for new mount.

# Configuration, mandatory
# Version must be 1.1 or else LinuxCNC assumes it is from previous
↪  version
# with no joint/axis separation.
[EMC]
VERSION = 1.1
MACHINE = BIG_MACHINE
DEBUG = 0
```

```
# Low-level driver for motion controller board, custom variables
# Mesa Electronics 7I96 and 7I77
# IP address can be set on EEPROM of board, factory set to 10.10.10.10
[HOSTMOT]
HOSTMOT = hostmot2
PORT = hm2_eth
IP_ADDRESS = 10.10.10.10

# GUI, mandatory
[DISPLAY]
DISPLAY = axis
CYCLE_TIME = 0.100
POSITION_OFFSET = MACHINE
POSITION_FEEDBACK = COMMANDED
MAX_FEED_OVERRIDE = 1.2
PROGRAM_PREFIX = ./M_files
INTRO_GRAPHIC = emc2.gif
INTRO_TIME = 1.0
MAX_LINEAR_VELOCITY = 70.0
INCREMENTS = 250 mm, 200 mm, 150 mm, 100 mm, 50 mm, 20 mm, 10 mm, 5 mm, 1
↪  mm, 100 um, 10 um, 1 um
OPEN_FILE = ""
PYVCP = pyvcp.xml
PYVCP_POSITION = RIGHT

[FILTER]
PROGRAM_EXTENSION = .png,.gif,.jpg Greyscale Depth Image
PROGRAM_EXTENSION = .py Python Script
png = image-to-gcode
gif = image-to-gcode
jpg = image-to-gcode
py = python

# Software Motion Controller, mandatory
# Periods are in nanoseconds
[EMCMOT]
EMCMOT = motmod
COMM_TIMEOUT = 1.0
```

```
BASE_PERIOD = 50000
SERVO_PERIOD = 2000000
TRAJ_PERIOD = 100000

# Configuration IO, mandatory
[EMCIO]
EMCIO = io
CYCLE_TIME = 0.100
TOOL_TABLE = tool.tbl

# G-Code, mandatory
[RS274NGC]
PARAMETER_FILE = big_machine.var
REMAP=M200 modalgroup=10 argspec=D python=m200
REMAP=M201 modalgroup=10 argspec=D python=m201
REMAP=M202 modalgroup=10 argspec=S python=m202
REMAP=M203 modalgroup=10 argspec=D python=m203
REMAP=M204 modalgroup=10 argspec=D python=m204
REMAP=M89  modalgroup=10  python=m89
REMAP=M93  modalgroup=10  argspec=Pkmdjiqfhser python=m93
REMAP=M94  modalgroup=10  argspec=I python=m94
REMAP=M95  modalgroup=10  argspec=PF python=m95
REMAP=M96  modalgroup=10  argspec=P python=m96
REMAP=M97  modalgroup=10  python=m97

REMAP=M88  modalgroup=10  argspec=PF python=m88

REMAP=M150 modalgroup=10 python=m150
REMAP=M800 modalgroup=10 python=m800
REMAP=M900 modalgroup=10 python=m900

REMAP=M248 modalgroup=10 python=m248
REMAP=M249 modalgroup=10 python=m249
REMAP=M250 modalgroup=10 python=m250
REMAP=M251 modalgroup=10 python=m251
REMAP=M252 modalgroup=10 python=m252
REMAP=M253 modalgroup=10 python=m253
REMAP=M254 modalgroup=10 python=m254
```

```
REMAP=M255 modalgroup=10 python=m255

REMAP=M300 modalgroup=10 python=m300
REMAP=M301 modalgroup=10 argspec=PQRSd python=m301
REMAP=M302 modalgroup=10 argspec=DEPRS python=m302
REMAP=M303 modalgroup=10 argspec=D python=m303
REMAP=M304 modalgroup=10 python=m304
REMAP=M305 modalgroup=10 argspec=ID python=m305
REMAP=M306 modalgroup=10 python=m306
REMAP=M307 modalgroup=10 argspec=dPQR python=m307
REMAP=M308 modalgroup=10 python=m308
REMAP=M309 modalgroup=10 python=m309
REMAP=M310 modalgroup=10 argspec=d python=m310
REMAP=M311 modalgroup=10 argspec=DEPRS python=m311

REMAP=M350 modalgroup=10 argspec=PDR python=m350
REMAP=M351 modalgroup=10 argspec=DEPQR python=m351

REMAP=M400 modalgroup=10 python=m400 argspec=IDp
REMAP=M401 modalgroup=10 python=m401 argspec=IDpr
REMAP=M402 modalgroup=10 python=m402 argspec=IDprq
REMAP=M403 modalgroup=10 python=m403
REMAP=M404 modalgroup=10 python=m404
REMAP=M405 modalgroup=10 python=m405 argspec=IDEprq
REMAP=M406 modalgroup=10 python=m406
REMAP=M407 modalgroup=10 python=m407
REMAP=M408 modalgroup=10 argspec=dPQRE python=m408
REMAP=M409 modalgroup=10 argspec=ID python=m409

# Task Scheduler, mandatory
[TASK]
TASK = milltask
CYCLE_TIME = 0.010

# HAL files, mandatory
[HAL]
HALUI = halui
HALFILE = big_machine.hal
```

```
HALFILE = custom.hal
POSTGUI_HALFILE = postgui.hal

[PYTHON]
PATH_PREPEND = python
TOPLEVEL= python/toplevel.py
LOG_LEVEL = 8

# Trajectory Planning, mandatory
# Each joint is one motor, X axis shares two motors
[TRAJ]
COORDINATES = X X Y Z A B C U V
AXES = 8
JOINTS = 9
LINEAR_UNITS = mm
ANGULAR_UNITS = degree
MAX_LINEAR_VELOCITY = 400.0

# Kinematics (joint-coordinate relation), mandatory
# trivkins => Joint offsets == end-effector position, as in a Cartesian
↪  machine
[KINS]
KINEMATICS = trivkins coordinates=xxyzabcuv kinstype=BOTH
JOINTS = 9
EXTRA_JOINTS = 0

# Axes and Joint Specifications, mandatory
# X axis is a gantry setup and uses two joints
# Y axis uses single joint
# Z axis is height of build bed
# A and B (labelled Z1 and Z2) control the height of the syringe and
↪  printhead
# C controls the carriage
# U, V controls the feed beds
[AXIS_X]
TYPE = LINEAR
MAX_VELOCITY = 100.0
MAX_ACCELERATION = 1600.0
```

```
MIN_LIMIT = -12.1
MAX_LIMIT = 301.0

[JOINT_0]
MAX_VELOCITY = 100.0
MAX_ACCELERATION = 1600.0
HOME_SEQUENCE = 1
DEADBAND = 0.003
P = 8
I = 1.5
D = 0.00
FF1 = 0.030
FF2 = 0.0
BIAS = 2.0
ENCODER_SCALE = -1000
HOME = 0.0
HOME_OFFSET = 0.0
HOME_SEARCH_VEL = -20.0
HOME_LATCH_VEL = -0.3
HOME_FINAL_VEL = 20.0
VOLATILE_HOME = 1

[JOINT_1]
MAX_VELOCITY = 100.0
MAX_ACCELERATION = 1600.0
HOME_SEQUENCE = 1
DEADBAND = 0.003
P = 8
I = 1.5
D = 0.00
FF1 = 0.030
FF2 = 0.0
BIAS = 2.0
ENCODER_SCALE = 1000
HOME = 0.0
HOME_OFFSET = 0.0
HOME_SEARCH_VEL = -20.0
HOME_LATCH_VEL = -0.3
```

```
HOME_FINAL_VEL = 20.0
VOLATILE_HOME = 1

[AXIS_Y]
TYPE = LINEAR
MAX_VELOCITY = 400.0
MAX_ACCELERATION = 10000.0
MIN_LIMIT = -1.0
MAX_LIMIT = 215.1

[JOINT_2]
MAX_VELOCITY = 400.0
MAX_ACCELERATION = 10000.0
HOME_SEQUENCE = 1
DEADBAND = 0.003
P = 7.0
I = 3.0
D = 0.0004
FF1 = 0.018
FF2 = 0.000015
BIAS = -1.7
ENCODER_SCALE = 1000
HOME = 0.0
HOME_OFFSET = 0.0
HOME_SEARCH_VEL = -20.0
HOME_LATCH_VEL = -0.3
HOME_FINAL_VEL = 20.0
VOLATILE_HOME = 1

[AXIS_Z]
TYPE = LINEAR
MAX_VELOCITY = 0.50
MAX_ACCELERATION = 20.0
MIN_LIMIT = -1.9
MAX_LIMIT = 93.00

[JOINT_3]
MAX_VELOCITY = 0.50
```

```
MAX_ACCELERATION = 20.0
HOME_SEQUENCE = 0
STEP_SCALE = 157.48
HOME = 1.65
HOME_OFFSET = 1.65
HOME_SEARCH_VEL = 0.00
HOME_LATCH_VEL = 0.00

[AXIS_A]
TYPE = LINEAR
MAX_VELOCITY = 2.0
MAX_ACCELERATION = 50.0
MIN_LIMIT = -0.1
MAX_LIMIT = 60.0

[JOINT_4]
MAX_VELOCITY = 2.0
MAX_ACCELERATION = 50.0
HOME_SEQUENCE = 0
DEADBAND = 0.001
P = 300
I = 100
D = 10
FF1 = 0.5
FF2 = 2.0
ENCODER_SCALE = 2000
HOME = 0.0
HOME_OFFSET = -1.0
HOME_SEARCH_VEL = -2.0
HOME_LATCH_VEL = -0.3
HOME_FINAL_VEL = 2.0
VOLATILE_HOME = 1

[AXIS_B]
TYPE = LINEAR
MAX_VELOCITY = 2.0
MAX_ACCELERATION = 50.0
MIN_LIMIT = -0.1
```

```
MAX_LIMIT = 45.1

[JOINT_5]
MAX_VELOCITY = 2.0
MAX_ACCELERATION = 50.0
HOME_SEQUENCE = 0
DEADBAND = 0.001
P = 1300
I = 40
D = 50
FF1 = 0.0
FF2 = 0.0
ENCODER_SCALE = 2000
HOME = 0.0
HOME_OFFSET = -1.0
HOME_SEARCH_VEL = -2.0
HOME_LATCH_VEL = -0.3
HOME_FINAL_VEL = 2.0
VOLATILE_HOME = 1

[AXIS_C]
TYPE = LINEAR
MAX_VELOCITY = 4.5
MAX_ACCELERATION = 100.0
MAX_LIMIT = 125.1
MIN_LIMIT = -0.1
# Custom keys for locating beds
RIGHT_POSITION = 125.00
LEFT_POSITION = 0.00

[JOINT_6]
MAX_VELOCITY = 4.5
MAX_ACCELERATION = 100.0
HOME_SEQUENCE = 0
STEP_SCALE = 78.74
HOME = 0.00

# Rightmost feed bed
```

```
[AXIS_U]
TYPE = LINEAR
MAX_VELOCITY = 0.50
MAX_ACCELERATION = 20.0
MIN_LIMIT = -1.9
MAX_LIMIT = 93.00

[JOINT_7]
MAX_VELOCITY = 0.50
MAX_ACCELERATION = 20.0
HOME_SEQUENCE = 1
STEP_SCALE = 157.48
HOME = 0.0
HOME_OFFSET = 0.0
HOME_SEARCH_VEL = 0.00
HOME_LATCH_VEL = 0.00

[AXIS_V]
TYPE = LINEAR
MAX_VELOCITY = 0.50
MAX_ACCELERATION = 20.0
MIN_LIMIT = -1.9
MAX_LIMIT = 93.00

[JOINT_8]
MAX_VELOCITY = 0.50
MAX_ACCELERATION = 20.0
HOME_SEQUENCE = 1
HOME = 9.14
HOME_OFFSET = 9.14
STEP_SCALE = 157.48
HOME_SEARCH_VEL = 0.00
HOME_LATCH_VEL = 0.00

[ROLLER]
DEADBAND = 0.01
P = 3.00
I = 0.00
```

```
D = 0.00
FF0 = 0.200
FF1 = 0.0
FF2 = 0.0
ENCODER_SCALE = 40960

[HEATER]
DEADBAND = 0.01
P = 1
I = 0
D = 0
FF0 = 0
FF1 = 0
FF2 = 0
```

Appendix B

G-Code

B.1 G-Code for Standard Printing

```
; Total number of layers/layers to print from starting index
#101 = 50
; Printing passes per layer
#102 = 5
; Current layer index/starting layer index
#103 = 0

; Heater current input in mA
#104 = 14.0
; Heater traverse speed in mm/min
#105 = 300

; Layer height in mm
#106 = 0.050
; Excess powder in mm
#107 = 0.070
; Roller rotational speed in rpm
#108 = 350
; Roller traverse speed in mm/min
#109 = 500
```

```
; Program start
; Select image directory
M404

; Repeat for all but last layer
O101 REPEAT [#101 - 1]
; Soft purge to prime nozzles
M406
; Printing
M408 D#102 P2 Q2 R1 E#103
; Heating
M409 I#104 D#105
; Spread new layer
M302 P1 D#106 E#107 R#108 S#109
#103 = [#103 + 1]
O101 ENDREPEAT

; Last layer, no powder spreading
; Soft purge to prime nozzles
M406
; Printing
M408 D#102 P2 Q2 R1 E#103
; Heating
M409 I#104 D#105

M2
```

B.2 G-code for Temperature Measurements

```
; Starting layer index
#101 = 0
; Layers to go through
#102 = 30
; Heater current input in mA
```

```
#103 = 14.0
; Heater traverse speed in mm/min
#104 = 300
; Idle time between trials in seconds (not including operational time)
#105 = 25
; Layer height in mm
#106 = 0.050
; Excess powder in mm
#107 = 0.070


; Start program
; Initialise start time
M403

; Dry Layers
O102 REPEAT [#102]
; Run heating sequence and measurements
M402 I#103 D#104 P#105 Q#101
; Spread new layer
M302 P1 D#106 E#107 R350 S500
#101 = [#101 + 1]
O102 ENDREPEAT

; Wet Layers
; Select image directory
M404
O102 REPEAT [#102]
; Soft purge to prime nozzles
M406
; Print layer index
M405 I#103 D#104 E#101 P#105 Q#101
; Spread new layer
M302 P1 D#106 E#107 R350 S500
#101 = [#101 + 1]
O102 ENDREPEAT

M2
```

Appendix C

Geometric Detection

Detecting the edges at which the dry and printed regions meet is useful for analysis of print accuracy and defects, detecting deviations between the intended image and where the binder is actually deposited. At the surface of the build bed, the dry region and printed region respond differently to heating and cooling, and so can be distinguished via temperature differences. We'll look at the following capabilities:

1. The degree to which the edges of a printed part can be resolved through the radiometric data and standard image processing techniques.
2. The degree to which defect-scale edges (sub-millimeter) can be resolved through radiometric data and standard image processing techniques.
3. The ability of the camera to detect binder regions when beneath a layer of powder (sub-surface detection).

As was noted in the Section 5.5.1, the absolute temperature differences between the dry and printed regions are visible in the heatmap images, with the difference being about 10°C or less. However, the temperature gradients at the edges of the parts do not have a significantly greater slope as the gradients that occur within the bulk dry powder due to heat transfer within the powder bed.

To assess the detectable edge quality, we can apply standard image processing, such as Sobel filters/Canny edge detection to develop an intuition for what can be detected.

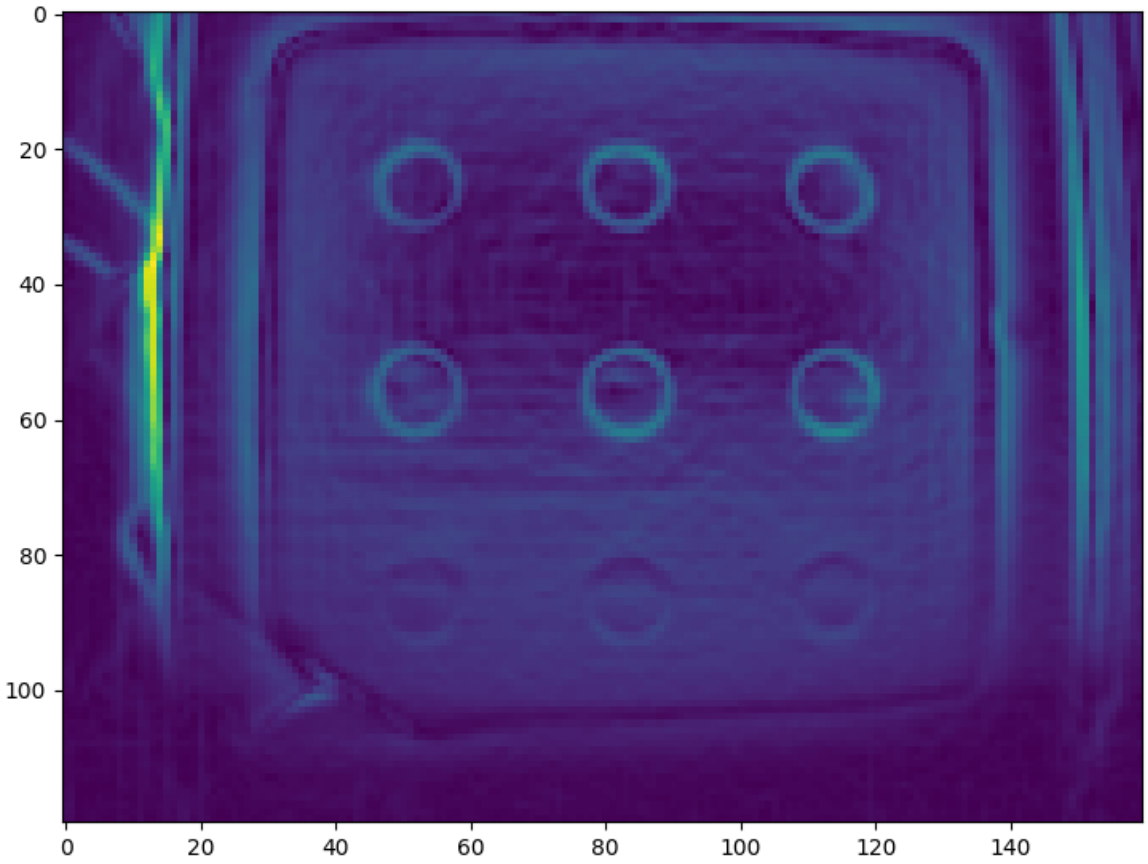


Figure C.1: Sobel 2D Filter, 389 W, 79.86 J/mm

In Figure C.1, after applying the 2D Sobel magnitude filter, we can see that the printed circles are visible with their edges responding visibly in the hotter regions of the build bed.



Figure C.2: Canny Edge Detector, 389 W, 79.86 J/mm

The performance of the thermal camera can also be considered in the context of defect detection, specifically in its ability to distinguish between binder and powder regions and gaps of various widths when held close to the powder bed. This gives some insight into the scale of defects that may be detectable and whether the camera can discriminate between two regions close-up.

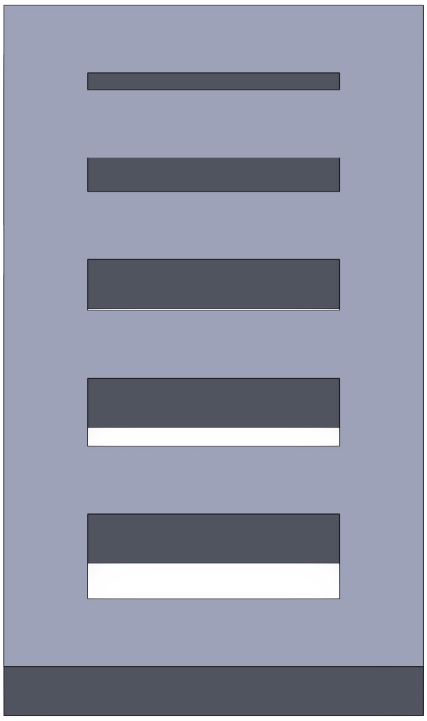


Figure C.3: Example Part with Gaps

The example part used is shown in Figure C.3, which contains a series of gaps of increasing size, starting with a width of 0.5 mm at the top and increasing by 0.5 mm for each gap below that.

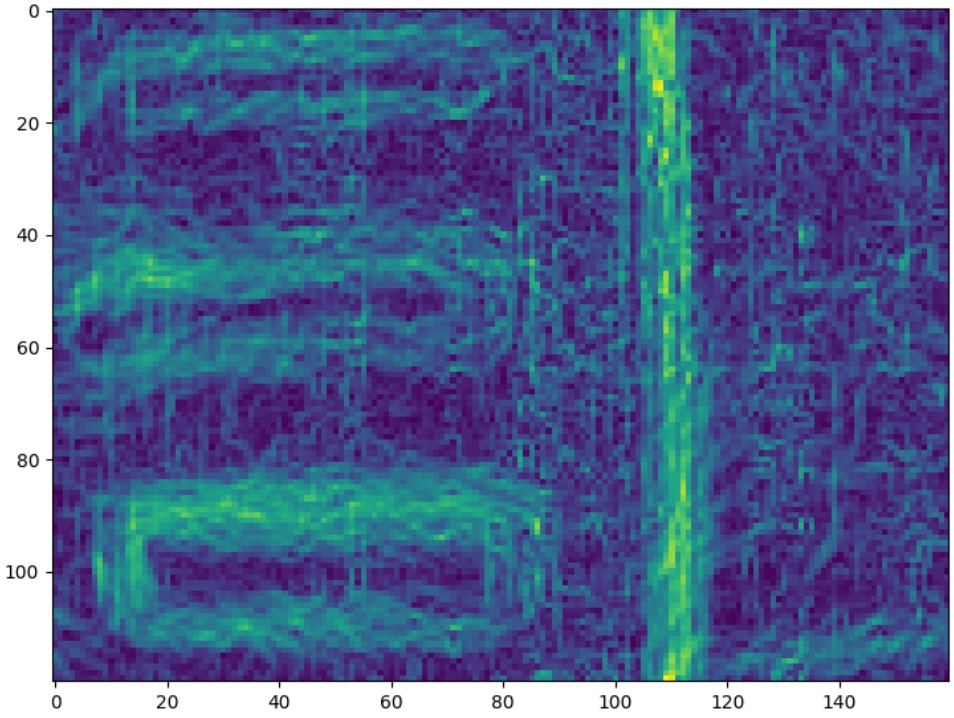


Figure C.4: Gap Test, Sobel 2D Filter

From Figure C.4, we get the impression that there are detectable edge regions when the thermal camera is held close to the printed part. However, the gradients are not distinct enough to sharply define and localise the edges of the part. There is also a significant amount of noise that occurs around the part edges due to minor variations in the non-edge regions. Given this, it is unlikely that images of this quality can be processed to produce high-fidelity edge images.

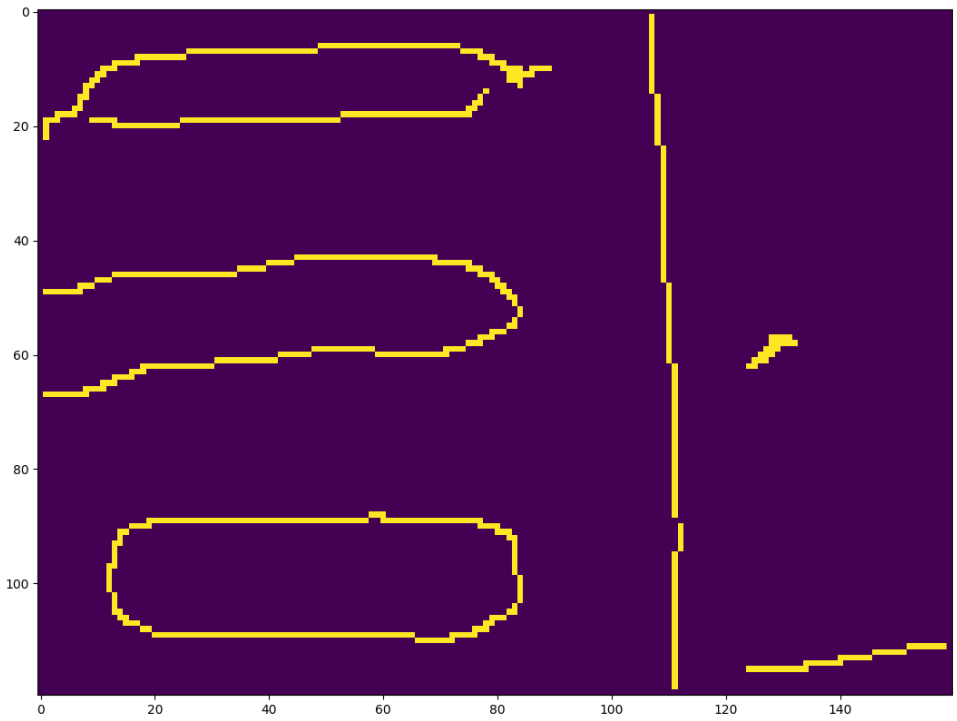


Figure C.5: Gap Test, Canny Edge Detector

Applying the Canny edge detector in Figure C.5, we can see that it is able to identify non-printed regions within the larger part, but does not accurately represent their size or shape.

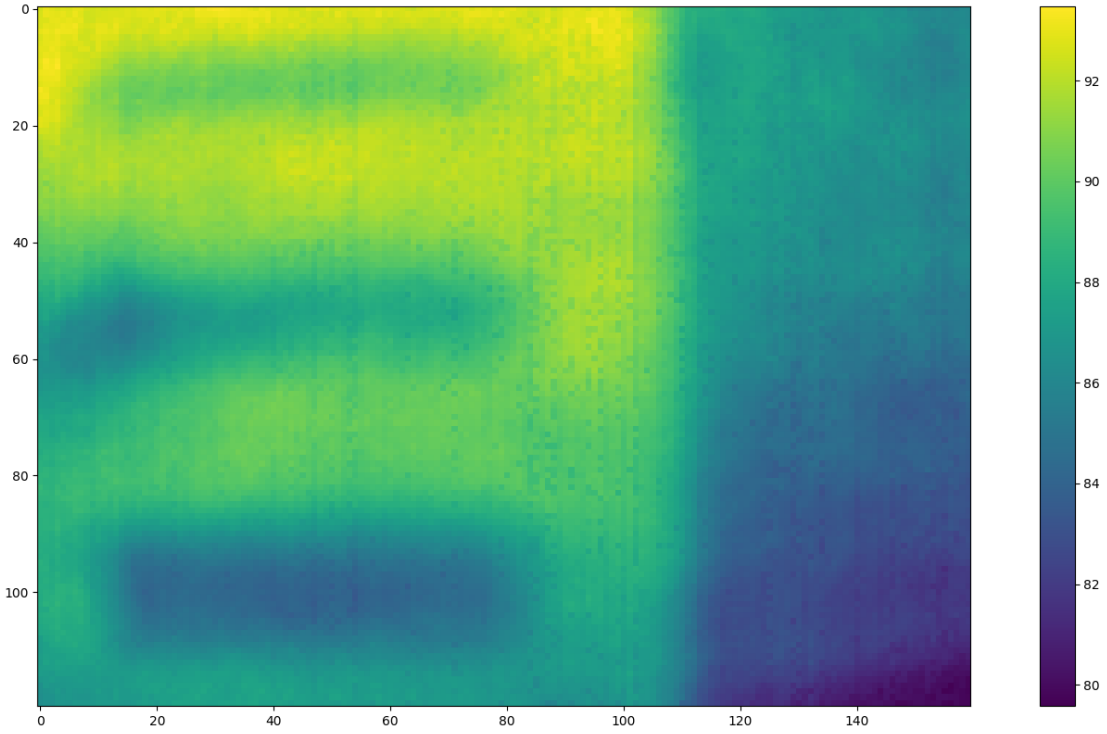


Figure C.6: Gap Test, Raw Data

By examining the raw temperature data, we can see that the absolute values of the difference between printed and non-printed regions are fairly small, and the gradients are fairly shallow. Given this, it is unlikely that the current temperature measurement setup will be able to resolve defects or features of this size.

Unsurprisingly, the thermal camera is almost totally incapable of resolving this fine geometry even under a relatively thin layer of powder. Figures C.7 and C.8 display a printed nine-circle array under a 50 µm thick layer of powder, where they can barely be seen.

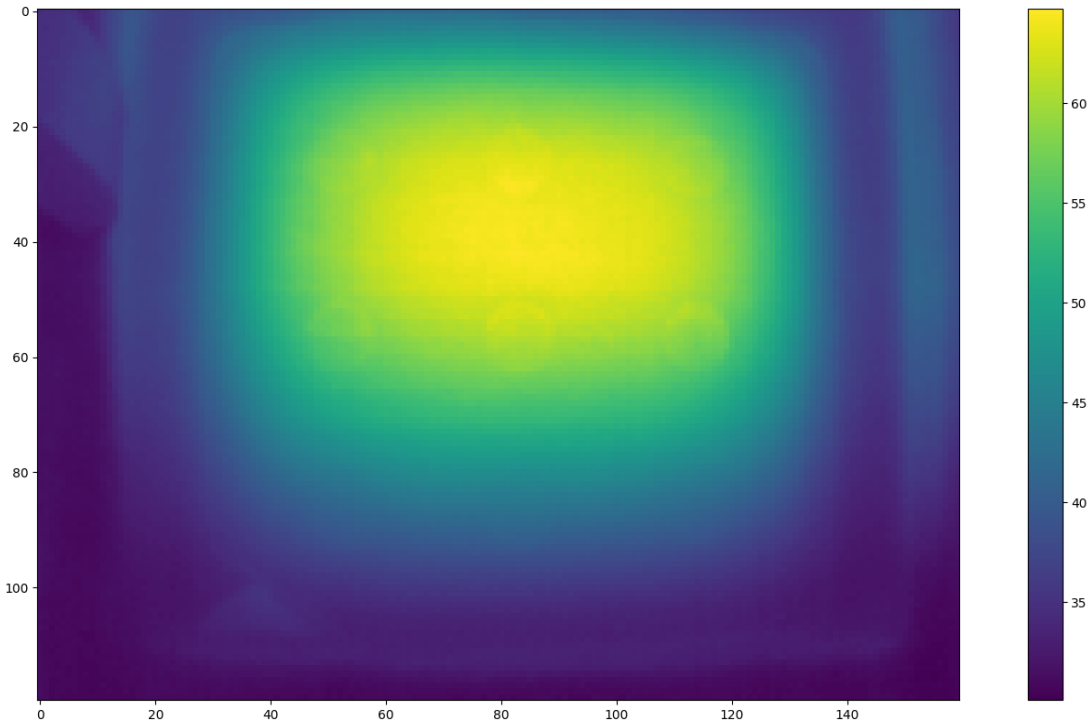


Figure C.7: Subsurface Test, Raw Data

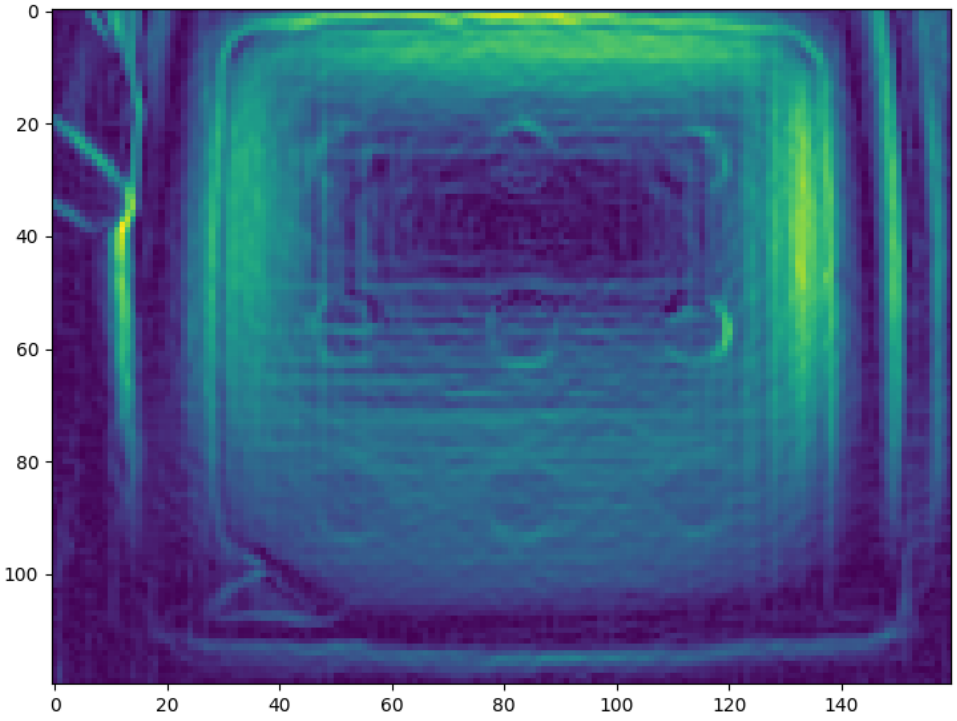


Figure C.8: Subsurface Test, Sobel 2D Filter

Given the results in Figures C.7 and C.8, it seems unlikely that sub-surface detection of geometry other than non-precise location and shape would be possible.

Regarding the noted detection capabilities,

1. The edges of simple parts can be roughly located based on the temperature differences between binder-wetted regions and unwetted regions.

2. For small-scale features, on the order of less than 2 mm, the temperature data collected does not have the information needed to accurately characterise their dimensions.

3. Sub-surface detection of printed geometry is generally going to be very low fidelity and does not seem to be easily made practical.

Appendix D

Emissivity Compensation

On review, the physics equations suggest that the measured temperatures can be converted to a (more accurate) adjusted temperature by converting to Kelvins, multiplying by a constant, and then converting back to Celsius. Unfortunately, there does not seem to be a physical reason behind the range of constants that would result in close fitting between thermocouples and thermal camera - the corresponding emissivity ratio is pretty close to 1, implying an emissivity close to 1. There may some emissivity compensation already occurring, or the camera is correct and the difference is within an expected range due to the temperature difference at the surface versus depth and the typical measurement error. The aforementioned low emissivity problems may also contribute [16].

The derivation on flirpy's library rearranges Planck's equation to define the temperature in terms of spectral counts [31], and what is desired is the relationship between the "measured" temperature and the "actual" temperature.

$$T = \frac{B}{\ln\left(\frac{R}{S-O} + F\right)}$$

$S =$ spectral counts
$O =$ offset (calibration parameter)
$F =$ free parameter (calibration parameter)

$$R = \frac{2h\nu^3}{c^2}$$
$$B = \frac{h\nu}{k_B}$$

$h =$ Planck's constant
$k_B =$ Boltzmann constant
$c =$ speed of light
$\nu =$ frequency

The reasoning is that the "measured" temperature received fewer spectral counts, proportional to its emissivity (so for an emissivity of 0.3, the counts at the detector were 30% of what a blackbody emitter would be. So,

$$T_{actual} = \frac{B}{\ln\left(\frac{R}{S-O} + F\right)}$$
$$T_{measured} = \frac{B}{\ln\left(\frac{R}{\varepsilon S-O} + F\right)}$$
$$\frac{T_{actual}}{T_{measured}} = \frac{\ln\left(\frac{R}{\varepsilon S-O} + F\right)}{\ln\left(\frac{R}{S-O} + F\right)}$$

This gives a ratio for the two temperatures in terms of the equation variables. Using a graphing calculator, we see that $\lim_{S\to\infty} T_{actual}/T_{measured} = \varepsilon^{-1}$ (so it is a function of counts, but for very high values of spectral radiance, it only depends on emissivity).

$R \propto \nu^3$, and by plugging in typical frequency values for infrared (20 to 200 THz), we get that $10^{-15} < R < 10^{-20}$. For "default" calibration parameters, $O = 0, F = 1$, the ratio approaches the limit basically immediately. However, the difference in Kelvins is only about 5%, which implies an emissivity very close to 1 (which doesn't fit the idea that there is no calibration for emissivity).

The results of this reasoning are inconclusive, and it seems probable that measuring this substrate with non-contact methods requires more sophisticated thermography knowledge and compensation.